1997

# A search for high mass photon pairs in $p\bar{p}$ [right facing arrow][small greek letter gamma][small greek letter gamma]jj events at [square root of s] = 1.8 TeV

Bryan Adrian Lauer
*Iowa State University*

# INFORMATION TO USERS

This manuscript has been reproduced from the microfilm master. UMI films the text directly from the original or copy submitted. Thus, some thesis and dissertation copies are in typewriter face, while others may be from any type of computer printer.

**The quality of this reproduction is dependent upon the quality of the copy submitted.** Broken or indistinct print, colored or poor quality illustrations and photographs, print bleedthrough, substandard margins, and improper alignment can adversely affect reproduction.

In the unlikely event that the author did not send UMI a complete manuscript and there are missing pages, these will be noted. Also, if unauthorized copyright material had to be removed, a note will indicate the deletion.

Oversize materials (e.g., maps, drawings, charts) are reproduced by sectioning the original, beginning at the upper left-hand corner and continuing from left to right in equal sections with small overlaps. Each original is also photographed in one exposure and is included in reduced form at the back of the book.

Photographs included in the original manuscript have been reproduced xerographically in this copy. Higher quality 6" x 9" black and white photographic prints are available for any photographs or illustrations appearing in this copy for an additional charge. Contact UMI directly to order.

**UMI**

A Bell & Howell Information Company
300 North Zeeb Road, Ann Arbor MI 48106-1346 USA
313/761-4700 800/521-0600

# A search for high mass photon pairs in $p\bar{p} \rightarrow \gamma\gamma jj$ events at $\sqrt{s} = 1.8$ TeV

by

Bryan Adrian Lauer

A dissertation submitted to the graduate faculty

in partial fulfillment of the requirements for the degree of

DOCTOR OF PHILOSOPHY

Major: High Energy Physics

Major Professor: John M. Hauptman

Iowa State University

Ames, Iowa

1997

Graduate College
Iowa State University

This is to certify that the Doctoral dissertation of

Bryan Adrian Lauer

has met the dissertation requirements of Iowa State University

Signature was redacted for privacy.

Major Professor

Signature was redacted for privacy.

For the Major Program

Signature was redacted for privacy.

For the Graduate College

*To Rebecca, with all my love.*

# TABLE OF CONTENTS

# LIST OF TABLES

# LIST OF FIGURES

# ACKNOWLEDGEMENTS

My long and arduous journey has come to an end and I am thankful to many, many people. First and foremost, I would like to thank my advisor John Hauptman. His enthusiasm and encouragement have made my years of work enjoyable and rewarding. John's great ability to solve tough problems and his global view of the field provided me with a great person to emulate and admire.

My true mentor at DØ is John Womersley, his many talents and seemingly inexhaustible resources have benefited me enormously. His ability to see the true essence of the problem at hand helped to speed up my solutions to several difficult problems. John is more than a mentor, he is a good friend who can always lighten up a grim situation with his wicked sense of humor.

At DØ I would like to thank all the good people for taking the time to answer my numerous questions about physics and life. A special thank you goes to Jay Wightman, Steve Jerger, Arthur Maciel, Elizabeth Gallas, Freedy Nang, Don Lincoln, Kristal Mauritz, and John Zhou. I would not have grown as much intellectually and spiritually without your friendships.

Going back in time a bit, I would like to thank Professor Douglas Brandt and Professor Keith Andrews from Eastern Illinois University. Their honesty and sharp comments about the field of physics still shape my views today. I am very thankful for their influence in continuing my education.

Last but not least, I would like to thank my family and friends for their encouragement and support. My brother Mark, for his questions about "bosons", my Parents' and sisters' confidence and pride in my work, Matt and Kara for the diversions in Ames, Dave and Jason for taking my abuse on the golf course, and Russ and Phyllis

my "adopted parents" for always being there. I can not thank all of you enough. Most importantly, I thank my loving wife, Rebecca, for putting up with my endless hours of work and isolation. I am very lucky to have such a dear friend for a wife.

# ABSTRACT

A search for new physics in the channel $p\overline{p} \rightarrow \gamma\gamma jj$ has been carried out. In some extended Higgs models, a light neutral scalar Higgs boson is produced with suppressed couplings to fermions and standard model(SM) strength couplings to vector bosons(bosonic Higgs), thus enhancing the $H \rightarrow \gamma\gamma$ channel. We required one photon in the event with $E_T^\gamma > 30\,\mathrm{GeV}$, $\mid \eta^\gamma \mid < 1.1$ or $1.5 < \mid \eta^\gamma \mid < 2.0$ and one photon with $E_T^\gamma > 15\,\mathrm{GeV}$, $\mid \eta^\gamma \mid < 1.1$ or $1.5 < \mid \eta^\gamma \mid < 2.25$. Additionally, we required one hadronic jet in the event with $E_T^{jet} > 30\,\mathrm{GeV}$, $\mid \eta^{jet} \mid < 2.0$ and one hadronic jet with $E_T^{jet} > 15\,\mathrm{GeV}$, $\mid \eta^{jet} \mid < 2.25$. The final $M_{\gamma\gamma}$ distribution is consistent with background and no resonance is observed. A 90(95)% confidence level (C.L.) upper limit cross section vs $M_{\gamma\gamma}$ is calculated, which ranges from 0.60(0.73) pb for $M_{\gamma\gamma} = 65\ \mathrm{GeV/c^2}$ to 0.24(0.32) pb for $M_{\gamma\gamma} = 150\ \mathrm{GeV/c^2}$. With standard model coupling strengths between the bosonic Higgs and vector bosons, and coupling strengths of zero between the bosonic Higgs and fermions a 90(95)% C.L. bosonic Higgs lower mass limit is set at 90(85) $\mathrm{GeV/c^2}$.

# 1 INTRODUCTION

Classically, "mass" is defined as a measure of the quantitiy of matter within an object. Physically, inertial "mass" is measured by using Newton's second law. $F = ma$. If we have in hand a standard mass (i.e. a known mass, $M_s$) and an unknown mass ($M_u$), and if we apply the same force and measure the acceleration of each mass ($a_s$ and $a_u$), we can derive the value of the unknown mass, $M_u$:

$$M_u = M_s \cdot \frac{a_s}{a_u} . \tag{1.1}$$

Everyday matter, what you and I are made of, is primarily composed of up quarks, down quarks, and electrons. Fundamentally, what gives the quarks, leptons, and bosons their mass? The Standard Model introduces mass with the Higgs mechanism [1, 2]. Simply put, the Higgs mechanism spontaneously breaks the local electroweak gauge symmetry, and thus introduces a Higgs field (boson). The Higgs field permeates all of space, and interacts with the weak vector bosons and fermions to give them their relative mass. This is similar in idea to an electromagnetic field that permeates space and interacts with the electric charge of particles to give them their relative charge. In the simplest case there is one neutral scalar Higgs that generates all of the weak vector boson and fermion masses. But, Mother Nature might have chosen a more complex scenario! - such as a multiple Higgs sector which has both charged and neutral Higgses.

The focus of this dissertation is an extended Higgs scenario, which predicts multiple Higgs bosons and in particular a light neutral scalar Higgs with suppressed

couplings to fermions, but Standard Model strength couplings to the electroweak vector bosons($W$,$Z$,$\gamma$). Therefore, the one loop $W$ boson mediated $H \rightarrow \gamma\gamma$ decay channel is enhanced greatly, and sensitivity is expected for such a signal within DØ's run1 data sample [3].

# 2 THEORETICAL MOTIVATION

The following will give a brief explanation of the Standard Model theory (SM), not the mathematical formalism, but the resulting physics that is studied. Further with my dissertation focusing on an extended Higgs model, I will explain in some detail local electroweak symmetry breaking, which is the SM's formalism for introducing mass to the fermion and boson particles within the theory.

## Fundamental Forces and Particles

The theoretical framework used to describe particles and their interactions at the length scale of $10^{-15}$ meters is the Standard Model [4] (SM). The SM is built upon two types of particles, half-integer spin fermions and integer-spin bosons. The bosons are the carriers of the fundamental forces and the fermions are the fundamental building blocks of nature.

There are four fundamental forces of nature: strong, weak, electromagnetic (EM), and gravitational. The strong, weak, and EM forces dominate on small distance scales, while gravity is only important on the large distance scales and will be neglected for this discussion. The forces are transmitted by the exchange of integer spin boson particles; the strong interaction is mediated the gluons, the weak interaction is mediated by the massive $W^+$, $W^-$, and $Z^o$ bosons, and the EM interaction is mediated by the photon. Each force has distinctive behavior from one another and Table 2.1 gives some information about them.

Table 2.1 Some properties of the gauge bosons. Here V(r) is the spatial dependance of the potential.

| Force | Boson | Mass (GeV) | EM Charge | V(r) | Effective Range (cm) | Relative Strength |
|---|---|---|---|---|---|---|
| Strong | gluon | 0 | 0 | r | $10^{-13}$ | 1 |
| Weak | $W^{+-}, Z^{o}$ | 80.2, 91.2 | $\pm 1, 0$ | $\frac{e^{-Mr}}{r}$ | $10^{-15}$ | $10^{-6}$ |
| EM | photon | 0 | 0 | $\frac{1}{r}$ | $\infty$ | $10^{-2}$ |

The EM potential has the familiar 1/r behavior, and is detectable at small and large scales. The weak potential has an $e^{-Mr}$ suppression factor, thus the weak potential(force) is only effective on the smallest length scales. The strong potential would have similar EM potential behavior, but the gluon has an additional quantum number called color. The gluon carries color charge, therefore a gluon can interact with other gluons, unlike its photon counterpart that does not interact with other photons. A result of the gluon-gluon interaction is 'color asymptotic freedom' (the gluons and quarks experience little force at small r, but experience a large force at larger r). Thus, gluons and quarks must form 'colorless' states to be isolated, and this is observed experimentally (this is explained more clearly in a later section). All bosons have an antiparticle which is their twin particle with the same mass, but opposite quantum numbers (most noticeably the EM charge). The $Z^{o}$, photon, and gluon are-their-own antiparticle, but the $W^{+}$ antiparticle is the $W^{-}$.

The idea of bosons being the carriers of force is most easily imagined by an electron - electron interaction (Fig.2.1). The like-sign electrons both repel each other due to the emission and absorption of a photon. The system conserves momentum, but does not conserve energy when the interaction is in the intermediate "e + e + $\gamma$" state due to the excess energy from the photon exchange. The violation of energy conservation is allowable for a short period of time as theorized by the Heisenberg uncertainty principle ($\Delta E \cdot \Delta t \leq h$). The photon exchange results in the repulsive Coulumbic force of two like charges. Since the photon exists on borrowed energy it is

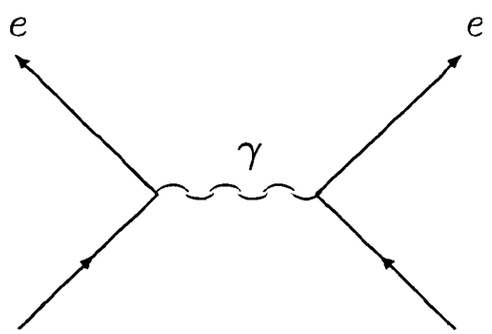


Figure 2.1 Photon exchange between electrons.

called a 'virtual' photon, and this idea of 'virtualness' is allowable for every type of boson.

The fundamental building blocks of nature are spin half fermions which are categorized as two distinct classes of particles called leptons and quarks. The leptons e, $\mu$, and $\tau$ interact (force) weakly and electromagnetically, the lepton-neutrinos only interact weakly, and the quarks can interact weakly, electromagnetically, and strongly. Each type of quark and lepton are referred to as flavors, e-flavor or u-flavor, which will be of importance later. A listing of all the known leptons and quarks is shown in Table 2.2.

The leptons and quarks are grouped in such a manner as to have three generations or families. Each generation has the same symmetric underpinnings, but each generation is progressively more massive, thus harder to discover (the top quark was just discovered three years ago by DØ and CDF). Only three families have been found, but the possibility of a fourth is small. For each fermion there is an anti-particle which has the same mass, but opposite quantum numbers, most noticeably the EM charge. So for an electron there is an anti-electron (positron), for an up quark there is an anti-up quark, and so on.

Table 2.2 Some properties of the leptons and quarks.

| Particle | EM Charge | Mass (GeV) | Type | Generation |
|---|---|---|---|---|
| up - u | +2/3 | $4 \cdot 10^{-3}$ | quark | 1 |
| down - d | -1/3 | $7 \cdot 10^{-3}$ | quark | 1 |
| neutrino - $\nu_e$ | 0 | $< 10^{-8}$ | lepton | 1 |
| electron - e | -1 | $5.11 \cdot 10^{-4}$ | lepton | 1 |
| charm - c | +2/3 | 1.5 | quark | 2 |
| strange - s | -1/3 | 0.2 | quark | 2 |
| neutrino - $\nu_\mu$ | 0 | $< 1.5 \cdot 10^{-4}$ | lepton | 2 |
| muon - $\mu$ | -1 | .106 | lepton | 2 |
| top - t | +2/3 | 175 | quark | 3 |
| bottom - b | -1/3 | 4.7 | quark | 3 |
| neutrino - $\nu_\tau$ | 0 | $< 7 \cdot 10^{-2}$ | lepton | 3 |
| tau - $\tau$ | -1 | 1.78 | lepton | 3 |

The quarks interact strongly and carry a color charge of red - r, green - g or blue - b and the antiquarks carry a color charge or antired - $\bar{r}$, antigreen - $\bar{g}$, and antiblue - $\bar{b}$. The gluons carry one color and one anti-color charge, such as $b\bar{g}$ or $g\bar{b}$. to conserve color at a quark-quark-gluon vertex, there are 8 possible color states for the gluon (Fig.2.2). An important result of the color charge is that, theoretically, any observable particle (proton, pion, etc.) can not have net color, the observable objects color must be conserved or colorless. Therefore, experimentalists should never observe an isolated quark or gluon, just colorless manifestations of them, such as a proton or pion. Experimentally, an isolated quark or gluon has not been observed. In the simplest terms, color combinations that produce a colorless final state are:

- Three separate colors used in combination give a colorless state.
  - ▷ proton(uud) $\rightarrow$ u(r)u(b)d(g).
- A color-anticolor combination gives a colorless state.
  - ▷ pion($u\bar{d}$) $\rightarrow$ u(r) $\bar{d}(\bar{r})$

Experimentally colored objects are not observed, for example no 'uu' hadronic particle to date has been found with an electric charge of +4/3 and spin 1, since the observable

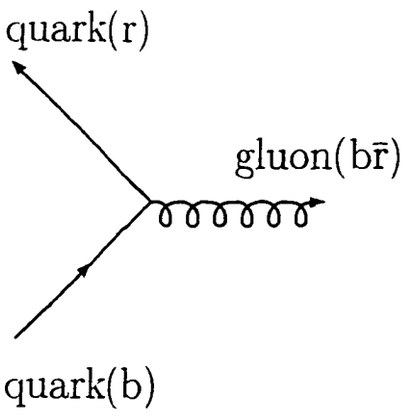


Figure 2.2 Color conservation for a quark-gluon vertex.

state is not colorless.

The lepton neutrinos only interact weakly. The weak interactions allow the conversion of an electron neutrino to an electron (charged current interaction (CC) - flavor changing transition) and the neutral interaction of neutrino to neutrino (neutral current interaction (NC)). This is true of quarks as well. u $\rightarrow$ d (CC) or u $\rightarrow$ u (NC), Fig.(2). Notice how similar the Z boson exchange is to the photon exchange. A clear difference though, is that the Z boson neutral current interaction can occur between electrically neutral neutrinos, which is not allowable for photon exchange.

The quark's weak charged current interaction is slightly more complicated than what was stated. A d quark can change into its doublet partner u quark (the 'doublet' terminology will be explained later), but the d quark can also transform into the higher generation up-type quarks of charm and top. The probability for a d $\rightarrow$ c or d $\rightarrow$ t transition is smaller comparative to the d $\rightarrow$ u transition, and the probabilities are grouped as a Kobayashi - Maskawa (KM) flavor changing mixing matrix. As a rule, the probability for a flavor change from a 1st generation quark to the 3rd generation quark is the lowest, and same generation transitions have the largest probability. The weak flavor changing neutral current interactions are not allowed by the GIM-

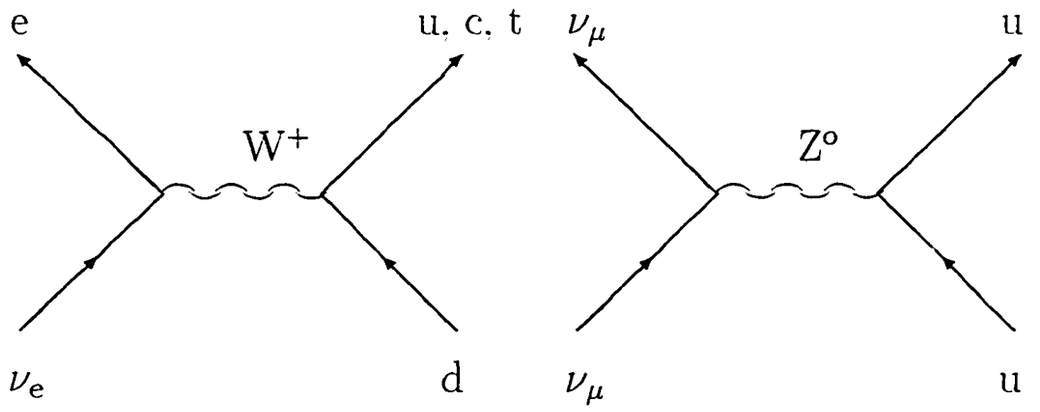


Figure 2.3 Simple examples of the charged and neutral weak interactions.

mechanism, therefore u $\rightarrow$ t or u $\rightarrow$ c are forbidden. Inter-generational charged or neutral mixing is not allowable for the leptons, since the lepton number(flavor) must be conserved. The above excluded weak charged and neutral current channels have been studied experimentally and are found to be valid as of the publication date of this paper.

## Standard Model

The Standard Model is the combination of three quantum field theories:

- the Quantum ElectroDynamic theory (QED) - U(1),
- the Weak theory - SU(2), and
- the Quantum ChromoDynamics theory (QCD) - SU(3)[1].

Recently, the QED and weak theories have been unified to form the $SU(2)_L \times U(1)_Y$ GWS theory. The three theories construct phase (gauge) invariant fields to describe particles and their interactions. By requiring the fields to be gauge invariant, for example QED, the physics is unchanged if any arbitrary phase ($e^{i\Lambda(x)}$) is introduced

[1]The discussion here will focus only on the QED and weak theories. For more information on QCD, I refer the reader to the cited references.

to the fermion-field, if we further properly adjust the photon-field ($\delta\Lambda(x)/\delta x$). The previous application of an arbitrary gauge to the fields is called a 'gauge transformation'. In a nutshell, the previous statements are explaining that the physics remains the same for all space and time, as it must. A result of constructing a gauge invariant spin 1/2 field is that there must exist a massless integer spin boson. Additionally from the theory one can calculate the couplings between the boson and fermions. The previous statements are precisely true of QED, where we have a spin 1/2 electron, with a massless spin 1 photon for a boson, and the the QED coupling constant is calculated (and measured) at $\alpha = 1/137$. For the weak theory, though, the W and Z bosons measured mass is about 100 GeV/$c^2$, which is a far from massless, but this problem is fixed with the introduction of the spontaneous local symmetry breaking (SLSB) mechanism.

The weak theory associates all the fundamental particles into doublet states, $\binom{\nu_e}{e}$, $\binom{\nu_\mu}{\mu}$, $\binom{\nu_\tau}{\tau}$, $\binom{u}{d}$, $\binom{c}{s}$, and $\binom{t}{b}$. Unlike the 1-dimensional U(1) theory, where there is one field for every particle, SU(2) has a 2-component field for every doublet. It is important to require gauge invariance, which is achieved here by applying a gauge transformation on every doublet state with a 2x2 hermitian matrix $\Lambda(x)$ (similar in idea to the QED case), and also to adjust the W boson field. The gauge transformation calculation here is significantly more difficult than the QED case, but the resulting $SU(2)_L$ part of the theory requires three massless $W^+$, $W^-$, and $W^\circ$ gauge bosons. Now, including the QED $U(1)_Y$ $B^\circ$ boson field with the weak $SU(2)_L$ $W^+$, $W^-$, and $W^\circ$ fields, a final $SU(2)_L \times U(1)_Y$ unified theory is achieved. The observable electroweak bosons of $W^+$and $W^-$ , $Z^\circ$, and $\gamma$, are composed of linear combinations of the $W^\circ$, $W^-$, $W^+$, and $B^\circ$ fields. The unified theory predicts fermion left handed helicity doublet states and fermion right handed singlet states. Therefore, $SU(2)_L$ allows either member of the left handed doublet to transform into its doublet partner (CC) or itself (NC), $e \leftrightarrow \nu_e$ or $e \leftrightarrow e$ respectively, while the right handed singlet

states can only transform into themselves (NC). All of the charged fermion states interact electromagnetically ($U(1)_Y$). Notice that there is not a right handed flavor change ($e \leftrightarrow \nu_e$), therefore right handed neutrinos need not exist and this is observed experimentally. The 'Y' subscript refers to the hypercharge, which relates the EM charge quantum number to the weak isospin quantum number, thereby unifying the weak and EM theories. A parameter which comes out of the unified electroweak theory is the electroweak mixing angle - $\theta_W$. For a given $\theta_W$, all gauge couplings are determined by the electric charge e, which is amazing.

A problem still exists, though, since the theory states that the $W^{\pm}$, $Z^{\circ}$ and fermions are massless. It is important that the theory remain gauge invariant (solvable), and yet the bosons must acquire mass. To generate mass via spontaneous local symmetry breaking (SLSB), a scalar Higgs field is introduced and for the simplest model four fields $\phi_i (i = 1 - 4)$ are combined into an isospin doublet.

$$\phi = \begin{pmatrix} \phi^+ \\ \phi^0 \end{pmatrix} = \begin{pmatrix} \frac{1}{\sqrt{2}}(\phi_1 + i\phi_2) \\ \frac{1}{\sqrt{2}}(\phi_3 + i\phi_4) \end{pmatrix} \tag{2.1}$$

To generate the masses, introduce the Higgs potential to the gauge invariant $SU(2)_L \times U(1)_Y$ lagrangian in the form,

$$V(\phi) = \mu^2 \phi^\dagger \phi + \lambda (\phi^\dagger \phi)^2. \tag{2.2}$$

Require $\mu^2 < 0$ and $\lambda > 0$, thus the potential has a minimum at a finite value of $| \phi |$. We want to expand $\phi(x)$ about some chosen minimum, which is chosen as:

$$\phi_1 = \phi_2 = \phi_4 = 0, \ \phi_3^2 = \frac{-\mu^2}{\lambda} = \nu^2. \tag{2.3}$$

Clearly the symmetry is broken since we choose a point in weak isospin and hypercharge space. Expanding $\phi(x)$ about the minima:

$$\phi_0 \equiv \frac{1}{\sqrt{2}} \begin{pmatrix} 0 \\ \nu \end{pmatrix}. \tag{2.4}$$

We can include a term for quantum fluctuations about the minimum,

$$\phi(x) \equiv \frac{1}{\sqrt{2}}\begin{pmatrix} 0 \\ \nu + h(x) \end{pmatrix}. \tag{2.5}$$

Now substituting the new Higgs field, $\phi(x)$, into the potential term within the full lagrangian, and reparameterizing the $\phi$ fields so that the unphysical Goldstone bosons are gauged away, we are left with massive $W^{\pm}$ and Z bosons, massive fermions, a massless photon and gluon since their gauge symmetry is never broken, and a new scalar boson called the Higgs.

The Physical effects are that a Higgs vacuum permeates all space and emits a massive colorless neutral scalar - Higgs boson. The $W^{\pm}$ bosons, Z boson, and fermions couple to the Higgs and acquire mass, while the photon and gluon do not couple thus remain massless. The Higgs-coupling to fermions and bosons is proportional to their mass, for example the electron:

$$\Lambda(\text{Higgs}) \equiv \frac{m_e}{\nu}. \tag{2.6}$$

Here $m_e$ is .511 MeV, and $\nu$(the vacuum expectation value) is 246 GeV, thus the coupling is very weak, but for the top quark the coupling ratio is $10^6$ larger!

The above, greatly abbreviated description of the electroweak SLSB mechanism is the simplest form of the Higgs mechanism mass generation scheme - the "minimal model". To be clear, the Higgs field is a single complex doublet which results in a single neutral scalar Higgs boson. The Higgs fields can be constructed as multiple doublets and even triplets, and this is what my dissertation will focus on. One should not think that any extended Higgs model is valid, though, since many parameters of the electroweak model have been measured. From the minimal model theory, the $\rho$ parameter is theorized to have a value of 1, and experimentally $\rho$ is observed to equal 1 as well. The $\rho$ parameter can be defined as:

$$\rho = \frac{M_W^2}{M_Z^2 \cos^2\theta_W}. \tag{2.7}$$

All of the above parameters have been measured and the experimental value is $\rho = 1.0004 \pm 0.0022 \pm 0.002$ [5]. Therefore, any extended model must preserve $\rho \approx 1$, otherwise the model is invalid.

## Extended Higgs Model

As stated any extended Higgs model must conserve $\rho \approx 1$. Theoretically $\rho$ is defined as:

$$\rho = \frac{\sum_{T,Y}[4T(T+1) - Y^2] \mid V_{T,Y} \mid^2 c_{T,Y}}{\sum_{T,Y} 2Y^2 \mid V_{T,Y} \mid^2}. \tag{2.8}$$

The variables $V_{T,Y}$ are the vacuum expectation value of the neutral Higgs field, with a total weak isospin quantum number T, and hypercharge Y. The parameter $c_{T,Y}$ is 1(1/2) for a complex(real) Higgs field. For $\rho = 1$ and for one complex Higgs field the prior equation can be more simply stated as,

$$(2T+1)^2 - 3Y^2 = 1\ , \tag{2.9}$$

thus the minimal Higgs model, which is a complex doublet with T=1/2 and Y=$\pm$1 has a value of $\rho = 1$. A first attempt at constructing an extended Higgs model could involve a complex triplet with the additional requirement of a neutral Higgs field. This will give a weak isospin, T, value of 1 and a hypercharge, Y, value of 0 or $\pm$2, which will result in $\rho \neq 1$ - unacceptable. Single triplet cases are not allowable. A valid extended model, that preserves $\rho$=1, is the combination of one doublet field, one real triplet field (T=1,Y=0), and one complex triplet field (T=1,Y=2) (HTM model [6, 7, 8, 9, 10, 11]). By using the previous equations it is readily seen that if the vacuum expectation values (VEV) for the triplet fields are nearly equal, $\rho = 1$ is conserved. The power of this extended model is that it does not violate any measured electroweak parameters, and no fine tuning of the theory is required beyond the VEV requirement.

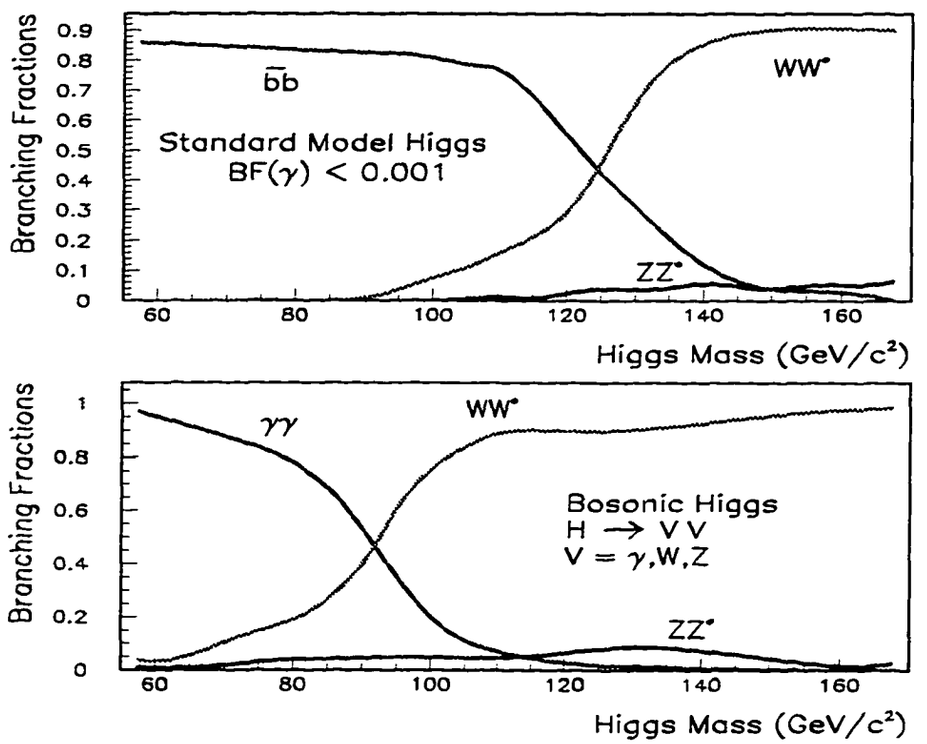


Figure 2.4 The branching fractions are much different for the two models. The $c\bar{c}$ and $\tau\bar{\tau}$ Higgs decay channels are not shown for the SM Higgs case. Notice the large enhancement in the photon channel for the bosonic Higgs model.

The HTM model has some interesting physics results. The theory produces a light neutral scalar Higgs with suppressed couplings to fermions. This type of Higgs boson will be called a "bosonic Higgs". As expected, the decay channels of the bosonic Higgs are much different from the minimal standard model (SM) Higgs and are shown in Figure 2.4. Since the fermion decay channels are suppressed, the decay of the bosonic Higgs with mass less than $2M_W$ is not dominated by $H \rightarrow b\bar{b}$. At tree level the bosonic Higgs decays only to $W^*W^*$ and $Z^*Z^*$ vector bosons (where "*" denotes off-the-mass-shell). At the one loop level the bosonic Higgs decays predominantly

into two photons. The one loop W boson mediated $H \rightarrow \gamma\gamma$ channel is competitive for bosonic Higgs masses less than 90 GeV/$c^2$, with the tree level decays due to the vector bosons being considerably off-the-mass-shell. Three possible Higgs production diagrams in $p\bar{p}$ collisions are shown in Figure 2.5. The most detectable production mode is the radiated Higgs channel, where an off mass shell $W$ or $Z$ vector boson is produced and radiates a Higgs boson [3]. Vector boson fusion has the same event topology, but the production cross section is about five times smaller, and will be included into the theoretical cross section for the limit calculation. The summed $HW$ and $HZ$ cross sections range from a couple of picobarns at $M_H = 60$ GeV/$c^2$ to several hundred femtobarns at $M_H = 100$ GeV/$c^2$ (Fig.2.6). Sensitivity is expected in the $\gamma\gamma jj$ final state, where the bosons decay $H \rightarrow \gamma\gamma$ and $W/Z \rightarrow jj$, up to a mass of about 85 GeV/$c^2$. The present mass limit on a bosonic Higgs is 60 GeV/$c^2$ from LEP1 [3, 12].

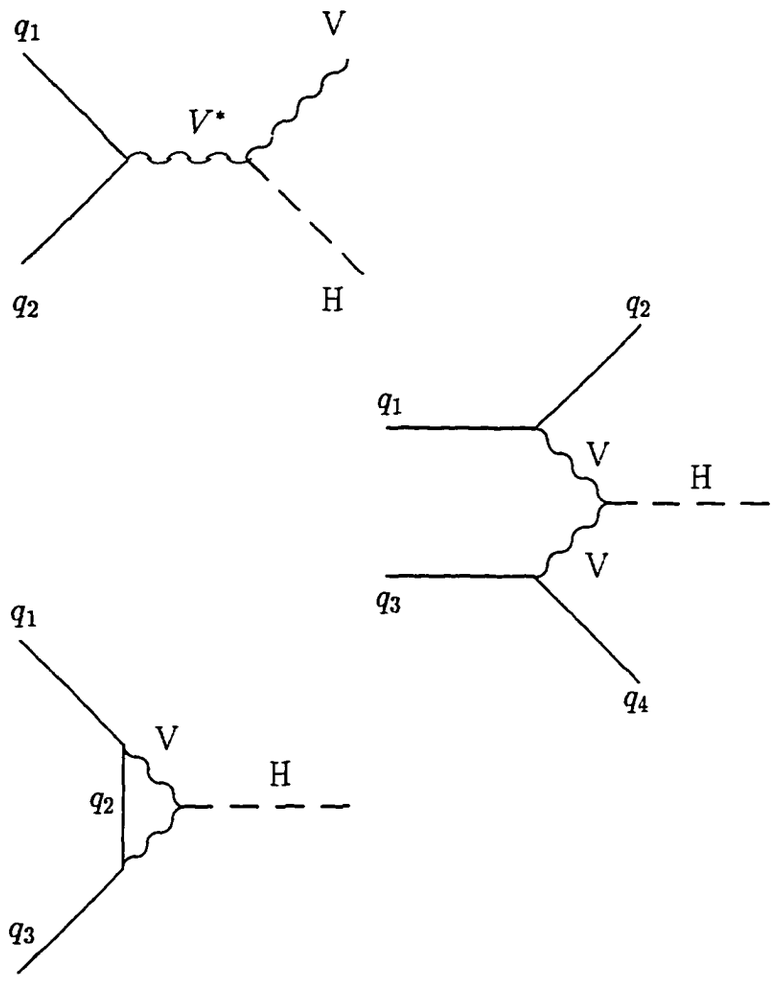


Figure 2.5 Production diagrams for the bosonic Higgs. The first diagram is the radiated Higgs channel, the second diagram is the vector boson fusion channel, and the third diagram is a one loop single Higgs production. The radiated Higgs channel is the most detectable, and will be studied exclusively.

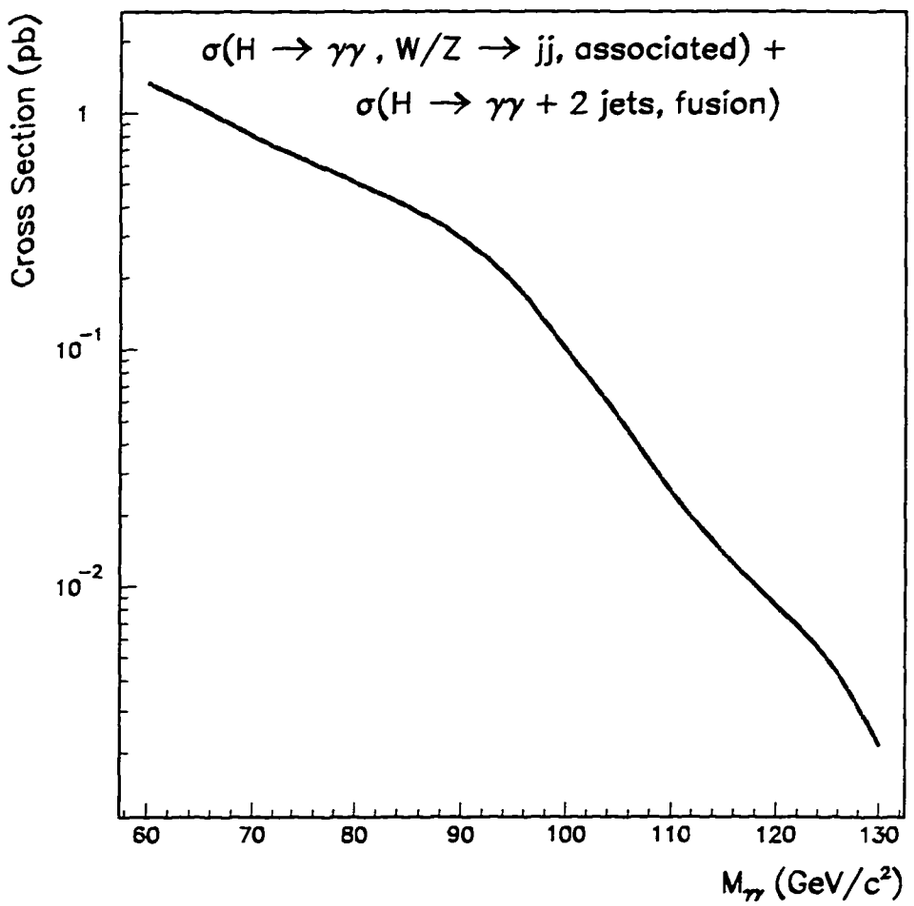


Figure 2.6 The cross section includes both HW/HZ associated production with Hjj fusion process. Folded into the cross section is the Branching fractions for W/Z to jets, and for the bosonic Higgs to decay into photons. The HTM model's final state cross section is over 1000 times larger than the minimal Higgs model.

# 3 EXPERIMENTAL APPARATUS

Commonly, the first inspection of an object is done visually. The visual resolution of the human eye using a microsope is limited to about $10^{-6}$ meters, about 1/10 the width of a human hair. In general, to resolve an object of length "d", the wavelength of the ambient light (probing matter) must be of similar length "d". As previously suggested matter has wave-like properties as well. In 1923 De Broglie postulated this and was experimentally verified by Davisson and Germer. The wavelike behavior of matter is characterized by:

$$\lambda = \frac{h}{p} \equiv \frac{hc^2}{E} , \tag{3.1}$$

where "$\lambda$" is the wavelength of the matter, "h" is Planck's constant, "p" is the momentum of the matter, "E" is the energy of the matter, and "c" is the speed of light. Therefore, to study matter with the resolution of $10^{-18}$ m, as is done at Fermilab, scientists must probe with an energy of 1 TeV( 1,000,000,000,000 electron volts), while visual inspection of an object involves a probing energy of only a few electron volts!

It is a huge undertaking to accelerate protons to such energies and study their interactions. While a microscope can simply fit on a lab table, a modern high energy accelerator is lucky to fit within the city limits. The Fermilab Tevatron is a great example of this; the Tevatron accelerator is $6 \times 10^3$ meters in circumference, and probes the $10^{-18}$ meter length scale. A brief review of the Fermi National Accelerator Laboratory's (FNAL) Tevatron accelerator [13, 14, 15] and DØ detector [16] are discussed here. For a more thorough explanation I refer you to the cited references.

## The Tevatron

The Tevatron accelerator is located at FNAL Batavia, Illinois. The Tevatron collides a 900 GeV beam of protons onto an opposingly directed 900 GeV beam of antiprotons, thus achieving a center of mass energy of 1.8 TeV, presently the largest center of mass energy in the world. The process of accelerating the proton and antiproton beams is a triumph of modern science. The protons and antiprotons are ramped up to their final energy by passing through many stages of acceleration as seen in Figure 3.1. More precisely, the protons are accelerated in five stages, while the antiprotons are accelerated in two stages[1].

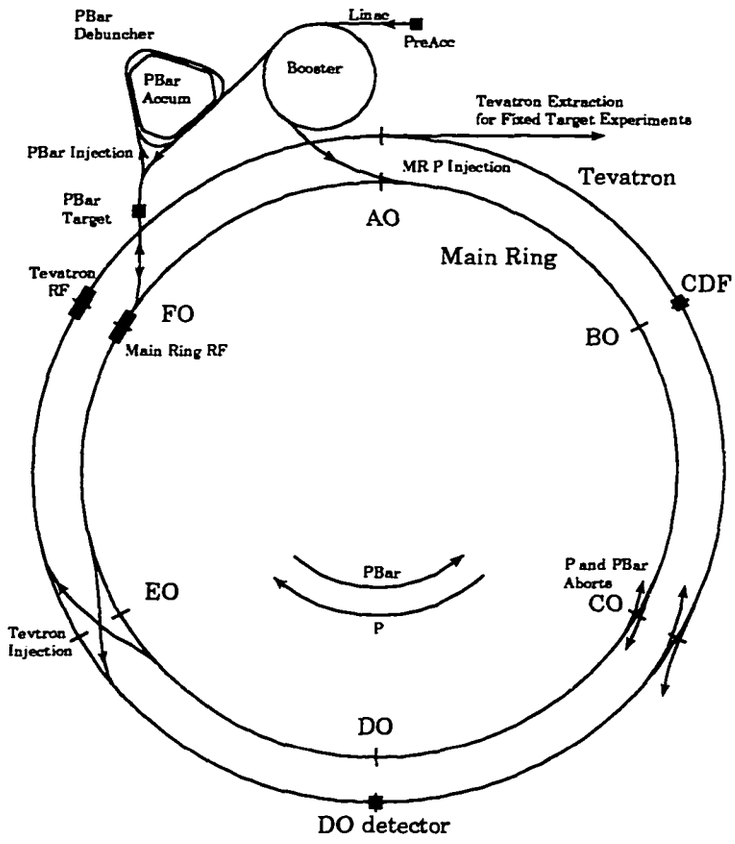


Figure 3.1 Schematic of the Fermi National Accelerator Laboratory

[1]The antiprotons are themselves created on the proton's fourth stage of acceleration.

The first stage of acceleration uses a Cockroft-Walton device which accelerates $H^-$ ions from rest to 750 KeV by several small potential steps. The exiting $H^-$ ion energy is limited by potential arcing. To simplify the injection process into the 3rd stage booster accelerator, $H^-$ ions are accelerated instead of $H^+$ ions(protons). The bending magnets of the synchrotron would repel the protons, but simply bends the $H^-$ ions into the sychnotron's acceleration tube. Just prior to the $H^-$ ions entering the sychnotron's accelerater tube, the electrons are stripped off by passing the $H^-$ ions through a carbon foil.

The second stage accelerates the $H^-$ ions to an energy of 400 MeV, in a linear accelerator called a linac. The linac uses alternating electric fields generated by a radio frequency(RF) cavity to accelerate the $H^-$ ions. The linac both accelerates the $H^-$ ions and also tunes the ions to a tighter beam energy(bunches the beam). Instead of having a continuous beam of ions within the accelerator, there are several collections of ions, called bunches. If a $H^-$ ion is lower in energy it will receive a larger boost of energy, if it is higher in energy it will recieve less of a boost. At the end of the linac the ions' electrons are stripped off by passing through a carbon foil. and the protons are injected into a synchrotron "booster".

The third stage "booster" is a 1/3 mile circumference synchrotron which increases the proton beam energy to 8 GeV. A synchrotron is a ring of magnets that continuously bends the proton beam into a circle, while the beam is accelerated periodically by a RF cavity. The beam is further tuned and bunched in this stage. before it is injected into the main ring synchrotron.

The main ring is the fourth stage of acceleration for the protons. The main ring is a 4 mile long synchrotron, which contains 1000 conventional copper coil magnets and several RF cavities. The main ring has another important purpose: some protons are diverted and strike a nickel target, producing antiprotons which are accumulated and separated from the large number of other secondary particles. The rate at

which antiprotons are collected is low, roughly 1 antiproton per 100000 proton/target collisions. It takes about 15 hours to accumulate enough antiprotons to attempt injection into the main ring. The oppositely moving proton and antiproton bunches are ramped up to an energy of 150 GeV in the main ring, before they are injected into the Tevatron synchrotron.

The Tevatron, the fifth stage, is a more exotic synchrotron, which is housed just a few feet above the main ring synchrotron. The Tevatron uses superconducting magnets, cooled with liquid helium to a temperature of $-450°$ F, to bend the proton and antiproton bunches in a circular path (the Tevatron is the largest producer and consumer of liquid helium in the world!). Likewise, an RF cavity accelerates the proton and antiproton bunches to 900 GeV. With the Tevatron in collider mode, there are 6 counter-cycling bunches of protons and antiprotons. The bunches are cycling in a helical manner so that the proton and antiproton bunches cross through each other at only 6 locations, AØ to FØ. In two of the beam crossing locations, large beam focusing magnets are present to increase the proton/antiproton interaction rate. Just outside the two beam focusing regions, BØ(CDF collider detector) and DØ(DØ collider detector) are located to detect the interactions. The proton/antiproton bunches cross in these regions every $3.5\mu$sec. The proton and antiproton beam luminosities are steadily decreasing as they are collided, so every 15 hours the beam is dumped and a new set of proton and antiproton bunches are injected, accelerated, and collided.

## DØ Detector

The DØ detector was constructed to study high mass states and large $p_T$ phenomena in $p\bar{p}$ collisions at $\sqrt{s} = 1.8$ TeV (Fig. 3.2) and in particular to search for the top quark and the Higgs boson, to study the $W$ and $Z$ bosons as a test of the electroweak model, and to study hadronic showers (jets) as a test of the QCD model

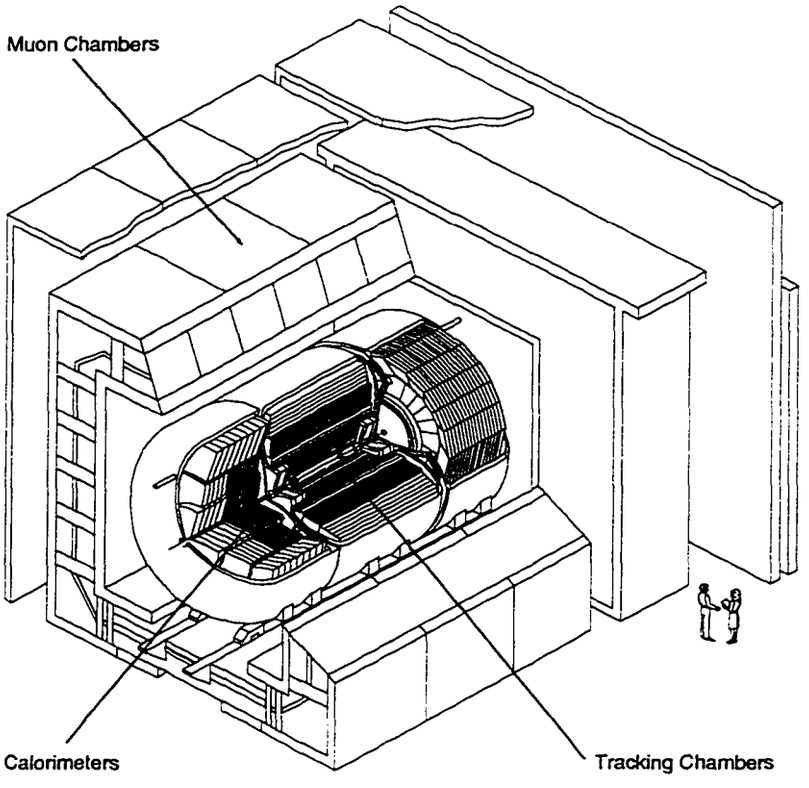


Figure 3.2 The 5500-ton, 40-foot-high DØ detector has three main detector systems: the central detector, the uranium-liquid argon sampling calorimeter, and the muon spectrometer.

were all on the agenda. Three tasks of detection were in mind:

- excellent identification of electrons and muons,
- good measurement of parton jets,
- good measurement of missing transverse energy.

The detection tasks are reasonable, since most interesting physics is associated with leptons($\mu$'s, e's, and $\nu$'s) and tests of QCD are studied through high $p_T$ jets. The DØ detector is composed of three main detection systems:

- Central Tracking, which discriminates between neutral and charged particles, with special emphasis on electron identification.
- Sampling Calorimeter, for energy measurement and particle identification.
- Muon Spectrometer, for measuring muon momentum.

When all the systems are used in conjunction, DØ is a powerful tool to test the standard model.

## Coordinate System

A right handed coordinate system is used at DØ. Here $+\hat{z}$ is down the beam pipe in the proton's direction, $+\hat{y}$ is pointing upwards in the sky, and $+\hat{x}$ is pointing away from the center of the Tevatron ring. The spherical(r,$\theta$,$\phi$) and polar(r,$\phi$,z) coordinate systems are generally used and have their usual definition of $\theta = 0$ at $+\hat{z}$, $\phi = 0$ at $+\hat{x}$, and $+\hat{r}$ is pointing perpendicular and away from the beam line. Since the center of mass energy of an event is not known, $\theta$ is represented as a psuedorapidity($\eta$) variable, defined as:

$$\eta = -\ln(\tan(\theta/2)) \; . \tag{3.2}$$

Pseudorapidity is nearly equal to rapidity, if the mass of the particle is much less than its energy, which is generally true at the Tevatron.

## Central Detector

The primary purpose of the central detector is to measure with good precision the position of a charged particle and locate the interaction point of the $p\bar{p}$ collision. DØ's central detector is not immersed in a magnetic field, thus no charged particle momentum measurement is made. Instead the central detector was designed for charged

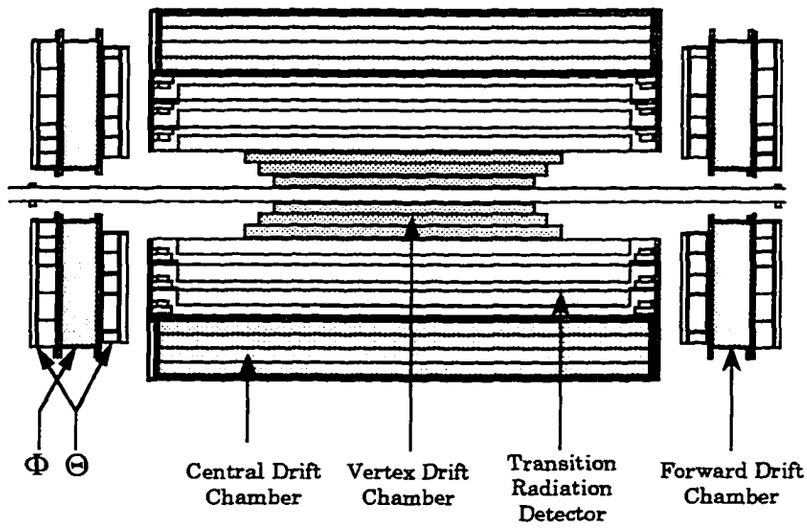


Figure 3.3 The DØ central detector. The innermost detector is the vertex detector, then the transistion radiation detector, and then the central and forward drift chambers.

particle detectection and recognition. This is done primarily with drift chamber detectors. A drift chamber detector is a low mass device which is filled with a specified gas and a uniform electric field. As a charged particle passes through the chamber it will ionize the gas and produce a trail of electrons and ions. The electric field will cause the electrons to drift to the sense wires, where a current pulse is detected. By knowing the properties of the gas and electric field, we know the drift times within the chamber and can reconstruct the position of the passing charge particle with great accuracy($\sim$50$\mu$m). DØ's central detector has four tracking systems as seen in Figure 3.3. The vertex drift chamber(VTX) helps determine the interaction point of the event(vertex). The transition radiation detector(TRD) can distinguish between pions, electrons, and converted photons. The central drift chamber(CDC) and the forward drift chamber(FDC) are used for vertex finding and charged particle track recognition. The first three listed detectors are barrel-like and start with a radius of 3.7cm and extend out to 74.5cm. The FDC are disk-like in shape and act as a lid to

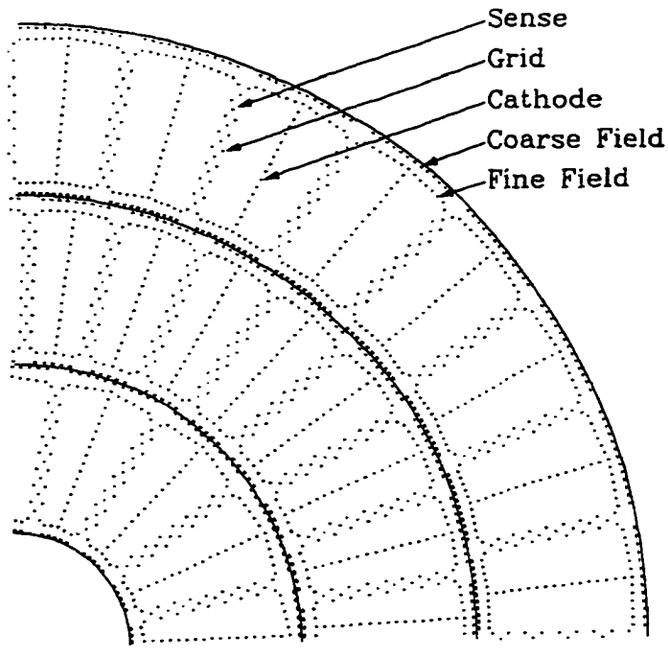


Figure 3.4 A r-$\phi$ slice of the vertex detector.

each end of the barrel-like central detectors. In conjuction they cover 360 degrees in $\phi$ and cover a pseudorapidity range of $|\eta| < 1.1$ and $1.5 < |\eta| < 3.1$.

### Vertex Detector

The vertex drift chamber detector is located closest to the interaction point. It has an inner radius of 3.7cm, an outer radius of 16.2cm, and a length of 116.8cm. The primary purpuse of the VTX is to determine the z-position of the interaction point. Figure 3.4 shows the physical layout of the cathode, anode, and sense wires. Table 3.1 gives most of the relevant information about the VTX. The VTX has three concentric layers with the innermost layer having 16 cells in $\phi$ and the outer two layers with 32 cells each in $\phi$. Each chamber has 16 cathode wires and 18 grid wires. Close to the grounded grid wires are the sense wires, which detect the ionization electrons from the passage of a charged particle. Further, the sense wires

Table 3.1 The vertex drift chamber information.

| Parameter | Specification |
|---|---|
| Radius | 3.7-16.2 cm |
| Overall Length | 116.8 cm |
| Number of Layers | 3 |
| Number of Cells/layer | 16,32,32 |
| Number of Sense Wires | 8 wires/cell |
| Sense Wire Voltage | +2500 Volts |
| Drift Field | 1 kV/cm |
| Gas Type | 95% $CO_2$+5% ethane+0.5% $H_2O$ |
| Gas Pressure | 1 atm |
| Gas Gain | $4\times10^4$ |
| Spatial Resolution | r$\phi \simeq$ 60 $\mu$m, z$\simeq$1.5 cm |

are staggered by 100$\mu$m to resolve left right ambiguities. The sense wires provide excellent r-$\phi$ positioning and are read out at each end to determine the z-coordinate. The VTX can resolve two tracks with a spatial resolution of $\sim$0.6 mm.

### Transition Radiation Detector

The transition radiation detector [17] works on the premise that highly relativistic particles traversing the boundary between materials with different dielectric constants will emit X-rays [18]. Since the particles are highly relativistic the X-rays are emitted in a forward direction ($\theta \sim 1/\gamma$). A nice consequence of this is that electrons and pions have distinctly different X-ray energy distributions. The calorimeter will measure the energy of an electromagnetic shower, but the TRD can distinguish an electron from a pion by the different TRD X-ray depositions. Note that the amount of energy emitted is proportional to $\gamma$;

$$dE/dx = N \cdot \gamma \ , \tag{3.3}$$

where N is some proportionality constant. So for a 10 GeV electron and pion their $\gamma$'s are much different,

$$\gamma \sim \frac{\text{Energy}}{\text{mass}} \tag{3.4}$$

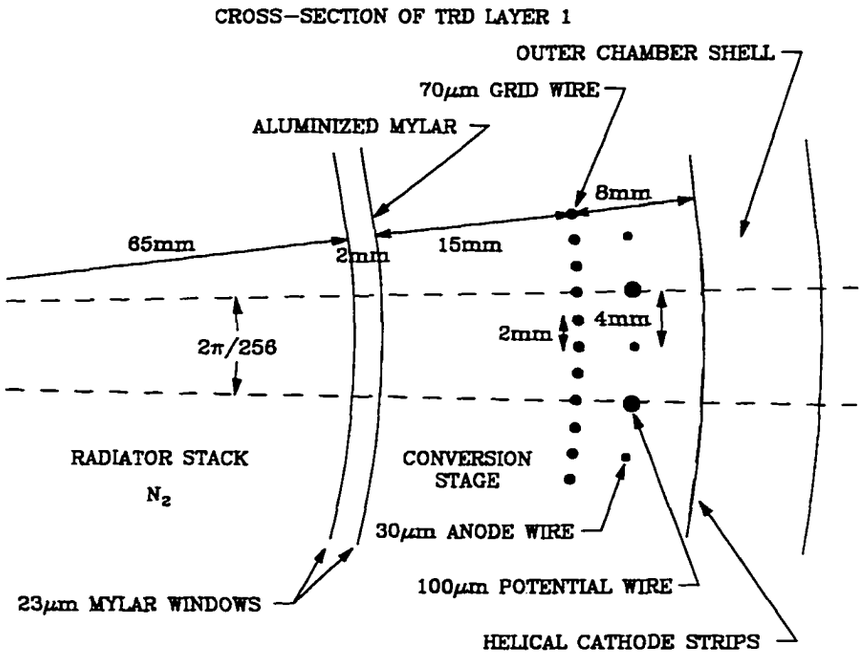


Figure 3.5 A r-$\phi$ slice of the transition radiation detector.

thus,

$$\gamma(\text{electron}) \sim \frac{10000\text{MeV}}{.5\text{MeV}} = 20000$$

and

$$\gamma(\text{pion}) \sim \frac{10000\text{MeV}}{100\text{MeV}} = 100 \ .$$

The average energy deposition in the TRD for the electron is 200 times larger. and this is the discriminant.

The DØ TRD's primary purpose is to distinguish electrons from converted photons and pions. DØ's TRD has 3 concentric layers of a polypropylene radiator foil and drift chambers (Fig. 3.5). The X-rays radiated in the foil convert to $e^+e^-$ pairs in the initial regions of the drift chambers and are detected by the anode sense wires located in the outer most region of the TRD.

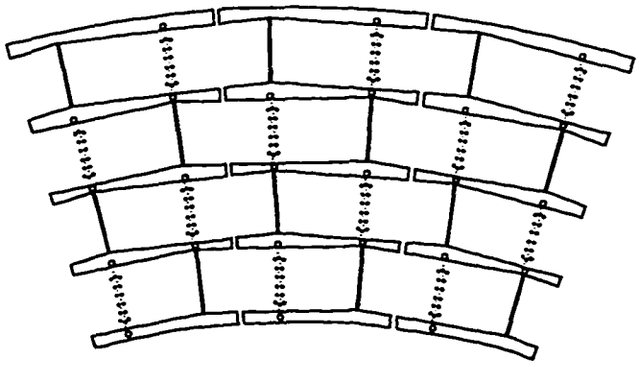

Figure 3.6 A r-$\phi$ slice of the central drift chamber detector.

### Central Drift Chamber

The outer most section to the central detector barrel-like region is the central drift chamber(CDC) [19]. The CDC has an inner radius of 49.5 cm and an outer radius of 74.5 cm, and an pseudorapidity coverage of $\eta \leq 1.1$. The primary purpose of the CDC is for charge particle r . $\phi$, and z positioning and dE/dx information. The CDC has 4 concentric layers with 32 $\phi$ cells per layer as seen in Figure 3.6. The cells are offset by half a cell in $\phi$ on neighboring layers to help distinguish between left-right ambiguities. Each cell has 7 sense wires, which are read out of one end to determine the r and $\phi$ positioning. Further, near the sense wires there are 14 ground wires near the sense wires to stablize the electric field. At each end of the set of sense and ground wire planes, there is a delay line. Delay lines are inductors which detect the current pulse in the closest sense wire. The delay lines are read out at both ends and determine the z position. The CDC can resolve two tracks with a spatial resolution of $\sim$2 mm. Most relevant information is listed in Table 3.2.

### Forward Drift Chamber

The lids to the barrel-like section of the central detector are the forward drift chamber detectors(FDC) [19]. The only far forward (large $\mid \eta \mid$) tracking is done

Table 3.2 The central drift chamber information.

| Parameter | Specification |
|---|---|
| Radius | 51.8-71.9 cm |
| Overall Length | 179.4 cm |
| Number of Layers | 4 |
| Number of Cells/layer | 32 |
| Number of Sense Wires | 7 wires/cell |
| Sense Wire Voltage | $\sim +1500$ Volts |
| Drift Field | 620 V/cm |
| Drift Velocity | 34 $\mu$m/ns |
| Gas Type | 93% Ar + 4% $CH_4$ + 3% $CO_2$ + 0.5% $H_2O$ |
| Gas Pressure | 1 atm |
| Gas Gain | $\sim 4 \times 10^4$ |
| Spatial Resolution | r$\phi \simeq 180$ $\mu$m, z $\simeq$ 2.9 mm |

by the FDC. The FDC's pseudorapidity coverage is $1.5 <| \eta |< 3.1$. The FDC's primary task is to determine the $\theta$ and $\phi$ positioning and dE/dx information of a charged object. The FDC has three modules; one PHI positioning module sandwiched between two THETA modules as seen in Figure 3.7. The PHI module has 36 cells with 16 sense wires running radially in each. No surprise, the PHI module measures the $\phi$ positioning of a charged paricle. Each THETA module has 24 cells each, offset by $\pi/4$ between each THETA module. Each cell has 8 sense wires which measure the $\theta$ positioning, and likewise each cell has a delay line which measures the orthogonal coordinate. The FDC can resolve two tracks with a spatial resolution of $\sim$2 mm. Most relevant information is listed in Table 3.3.

## Calorimeter Physics

DØ's calorimeter is a liquid argon sampling calorimeter, which is designed to periodically sample a shower's devolopment. A sampling calorimeter detector consists of alternating layers of a high "Z" material as a radiator and an active layer to sample the energy loss. Here "Z" is the atomic number. Thus, only a small fraction of

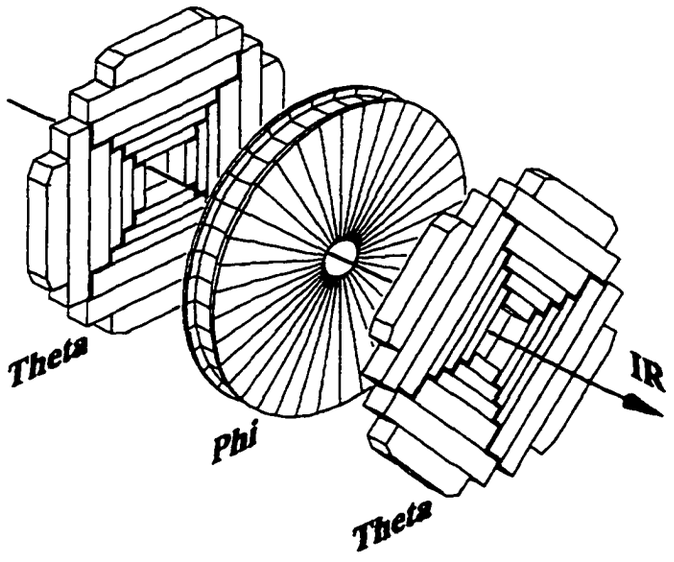


Figure 3.7 The geometry of the forward drift chamber detector.

shower's energy is measured, the sampling fraction. The showers are of two types. an electromagnetic shower caused by a photon or electron and a hadronic shower caused by hadrons. The two shower types are distinct and will be discussed seperately.

Electromagnetic showers [18] are initiated by either an electron or a photon entering a material of high "Z", such as lead (which will be the example here). If the electron has an energy greater than about 7 MeV the electrons lose most of their energy through radiated bremsstrahlung photons. For photons with an energy greater than about 7 MeV in lead the major loss of energy is through $e^+e^-$ pair production. For high energy photons or electrons this process will continue until the secondary particles have reached roughly 7 MeV, where atomic excitation and ionization become more important. Two important characteristics can be drawn from electromagnetic (EM) showers. The energy loss for EM showers is constant;

$$\frac{dE}{dx} = -\frac{E}{X_o}. \tag{3.5}$$

Here E is energy, x is distance, and $X_o$ is the radiation length. So for every $X_o$, 63% of the incident EM object's energy is lossed. The second characteristic is that the EM

Table 3.3 The forward drift chamber information.

| Parameter | Specification |
|---|---|
| Radius | 11-62 cm |
| Overall Length | $\pm$(104.8 - 135.2) cm |
| Number of Layers in each FDC | 2 $\Theta$, 1 $\Phi$ |
| Number of Cells/module | 24 $\Theta$, 36 $\Phi$ |
| Number of Sense Wires/cell | 8 $\Theta$, 16 $\Phi$ |
| Sense Wire Voltage | $\sim$ +1500 Volts $\Theta$ and $\Phi$ |
| Drift Field | 1000 V/cm |
| Drift Velocity | 40 $\mu$m/ns $\Theta$, 37 $\mu$m/ns $\Phi$ |
| Gas Type | 93% Ar + 4% $CH_4$ + 3% $CO_2$ + 0.5% $H_2O$ |
| Gas Pressure | 1 atm |
| Gas Gain | $\sim 4.3 \times 10^4$ |
| Spatial Resolution | r$\Theta \simeq$ 300 $\mu$m, $\Phi \simeq$ 200 $\mu$m |

shower have an electron, positron, and photon number 'maximum'. At this point in the shower development the most electrons, positrons, and photons are present. The maximum point can easily be defined in the number of radiation lengths:

$$t_{max} = 3.9 + \ln(E). \tag{3.6}$$

Thus for an incident electron with energy between 10-1000 GeV the shower maximum point is located at $6.2X_o$-$10.8X_o$ respectively. It is important to sample the shower well at its maximum, so that good energy and shower profile measurements can be made.

The second type of shower is a hadronic shower [18]. Hadronic showers are initiated when a hadron passes through a high "Z" material. The dominant loss of energy for the hadron is through nuclear scattering. The collisions produce many secondary particles and the process is repeated. The showers energy loss is parameterized with a nuclear interaction length parameter, $\lambda$. The hadronic shower are much deeper and wider than their EM counterparts. Typically, the secondary hadrons have a transverse momentum of $p_T \sim 350$ MeV/c, unlike EM secondary photons-electrons which have a transverse momentum of $p_T \sim p/\gamma \sim mass_{electron}$, where p is the momentum. The

difference in shower width is due to the large angles subtended by nuclear scattering (pion exchange). The differences between EM and hadronic shower depth is seen by the difference in uranium thickness needed for $1\lambda$ to $1X_o$, which is 3:1 respectively. Some rough calorimeter characteristics can be drawn from these two shower types:

- initial regions of the calorimeter should be devoted to EM showers;
- at 6-11 radiation lengths the EM shower should be sampled most carefully;
- the hadronic calorimeter is outside of the EM calorimeter;
- the hadronic calorimeter is roughly 3 times thicker than the EM calorimeter.

## The DØ Calorimeter

DØ's central detector is not capable of measuring charged particle momentum, since the central detector is not immersed in a magnetic field. Further, DØ's central detector can not detect neutral particles such as photons, neutrons, and $K_L^o$. Therefore, the DØ calorimeter was designed to have excellent energy measurement of electrons, photons, and jets. The calorimeter was further designed to easily discriminate between electrons/photons, jets, muons, and neutrinos (missing transverse energy). The DØ calorimeter is a liquid argon/uranium sampling calorimeter with a projective tower design (Fig. 3.8) covering 360° in $\phi$ and $|\eta| < 4$. The segmentation of the absorption plates are $\eta \times \phi = 0.1 \times 0.1$, except within the EM calorimeter's 3rd cutward layer, which is the EM shower maximum location. The EM calorimeter 3rd layer has a segmentation of $\eta \times \phi = 0.05 \times 0.05$. To have access to the central detector, the calorimeter is broken into three pieces as seen in Figure 3.9. The central calorimeter(CC) covers $|\eta| < 1.1$, and two identical end cap calorimeters(EC) cover $1.5 < |\eta| < 4.0$. The CC and EC calorimeters are encompassed by stainless steel cryostats which are filled with liquid argon. In each of the CC and EC calorimeters

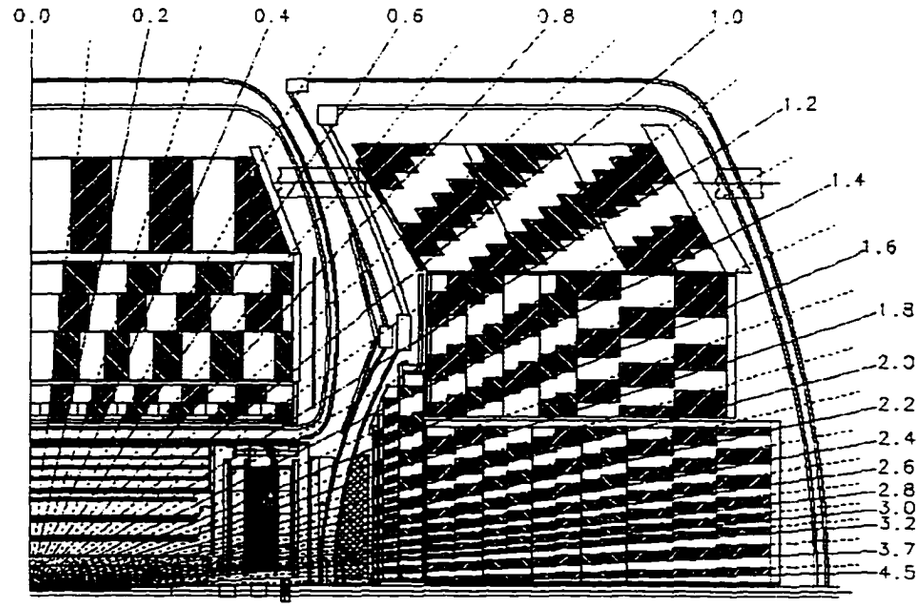


Figure 3.8 The psuedoprojective tower design of the calorimeter.

there are three distinct parts: an EM section with thin uranium plates (t $\sim 0.2\lambda$), a fine hadronic section (FH) with thicker uranium plates (t $\sim 1.0\lambda$), and a course hadronic section (CH) with thick copper or stainless steel plates (t $\sim 4.0\lambda$). The EC hadronic calorimeter is segmented into many ring-like modules. The FH in the EC has two modules: an inner fine hadronic (IFH) and a middle fine hadronic (MFH). The CH in the EC is segmented into three pieces : the inner course hadronic (ICH), the middle course hadronic (MCH), and the outer course hadronic (OCH). The combination of the two calorimeters gives full $\eta$ and $\phi$ coverage, and is nearly 'hermetic'. The radial sum of the plate interaction length thicknesses from EM to CH sections at $|\eta| = 0$ is t $\sim 7.2\lambda$ and at $|\eta| = 4$ is t $\sim 10.3\lambda$. Some information for the central calorimeter is listed in Table 3.4. Some information for the forward calorimeter is listed in Table 3.5.

A comment, the main ring (MR) accelerator passes through the CH part of the calorimeter. When antiprotons are being made, this can cause some excessive noise in

Table 3.4 The central calorimeter information.

| Parameter | EM | FH | CH |
|---|---|---|---|
| $\eta$ Range | $\pm$1.2 | $\pm$1.0 | $\pm$0.6 |
| Absorber Material | U | 98% U + 2% Nb | Cu |
| Absorber Thick. (mm) | 2.3 | 6.0 | 46.5 |
| Number of Layers | 4 | 3 | 1 |
| Depth/Layer | 2, 2, 7, 10 $X_o$ | 1.3, 1.0, 0.9 $\lambda$ | 3.2 $\lambda$ |
| Sampling Fraction | 11.79% | 6.79% | 1.45% |
| Layer Segmentation in | 0.1$\times$0.1 (1, 2, 4) | 0.1$\times$0.1 | 0.1$\times$0.1 |
| ($\Delta\eta \times \Delta\phi$) | 0.05$\times$0.05 (3) | | |
| Total Channels | 10,368 | 3000 | 1224 |

Table 3.5 The forward calorimeter information.

| Parameter | EM | IFH | ICH |
|---|---|---|---|
| $\eta$ Range | $\pm$(1.3-4.1) | $\pm$(1.6-4.5) | $\pm$(2.0-4.5) |
| Absorber Material | U | 98% U + 2% Nb | Stain. Steel |
| Absorber Thick. (mm) | 4.0 | 6.0 | 46.5 |
| Number of Layers | 4 | 4 | 1 |
| Depth/Layer | 0.3, 2.6, 7.9, 9.3 $X_o$ | 1.2 each $\lambda$ | 3.6 $\lambda$ |
| Sampling Fraction | 11.9% | 5.7% | 1.5% |
| Layer Segmentation in | 0.1$\times$0.1 (1, 2, 4) | 0.1$\times$0.1 | 0.1$\times$0.1 |
| ($\Delta\eta \times \Delta\phi$) [1] | 0.05$\times$0.05 (3) | | |
| Total Channels | 7488 | 4288 | 928 |
| **Parameter** | **MFH** | **MCH** | **OCH** |
| $\eta$ Range | $\pm$(1.0-1.7) | $\pm$(1.3-1.9) | $\pm$(0.7-1.4) |
| Absorber Material | 98% U + 2% Nb | Stain. Steel | Stain. Steel |
| Absorber Thick. (mm) | 6.0 | 46.5 | 46.5 |
| Number of Layers | 4 | 1 | 1 |
| Depth/Layer | 0.9 $X_o$ each | 4.4 $\lambda$ | 7.0 $\lambda$ |
| Sampling Fraction | 6.7% | 1.6% | 1.6% |
| Layer Segmentation in | 0.1$\times$0.1 | 0.1$\times$0.1 | 0.1$\times$0.1 |
| ($\Delta\eta \times \Delta\phi$) | | | |
| Total Channels | 1432 | 384 | 960 |

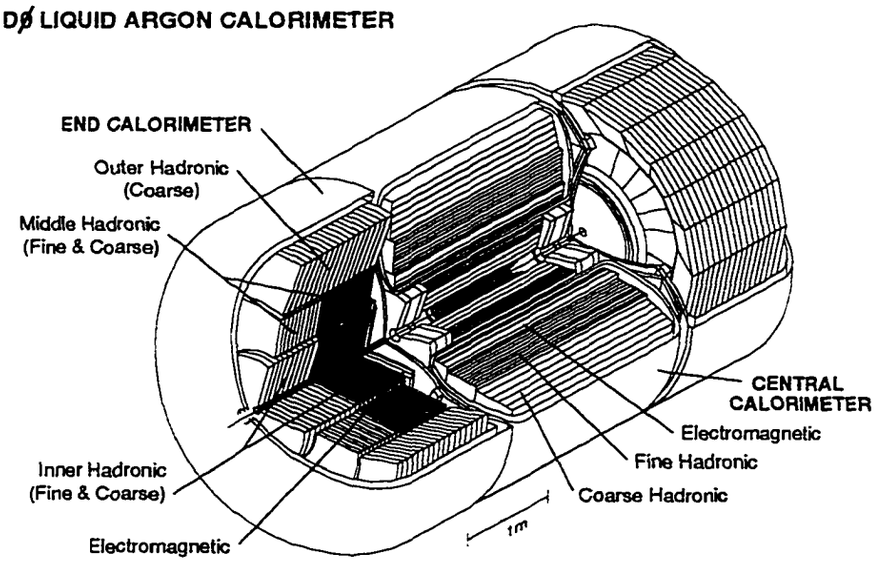


Figure 3.9 The DØ calorimeter.

this region of the calorimeter. The MR's noise is defined in two ways: when the MR is ramping up the proton's energy the proton beam is particularly noisy (MRBS_LOSS), and secondly when protons simply pass through the main ring CH in coincidence with a Tevatron $p\bar{p}$ crossing (MR_BLANKING). To account for this excessive noise, each noise source has an event 'flag' set, so that the triggers will not confuse noise in a CH tower for real hadronic shower energy.

A calorimeter cell is shown in Figure 3.10. The metal absorber is grounded while ~3 mm away a G10 resistive coated copper pad is kept at about +2000 volts. The electron drift time across the 3mm gap is about 450ns. Since the collected charge is small (~ about $10^6$ electrons/GeV) tha analog signal is amplified with a preamplifier. The signal has baseline detector noise which must be subtracted. Therefore the signal is passed through Base Line Subtracter (BLS) electronics. The BLS simply takes a cell signal sample just before and after the beam crossing, and takes the difference between the two. The BLS analog signal is then converted to a digital signal, by Fast Analog-to-Digital Converters (FADC). One digital count corresponds to 3.75 MeV of

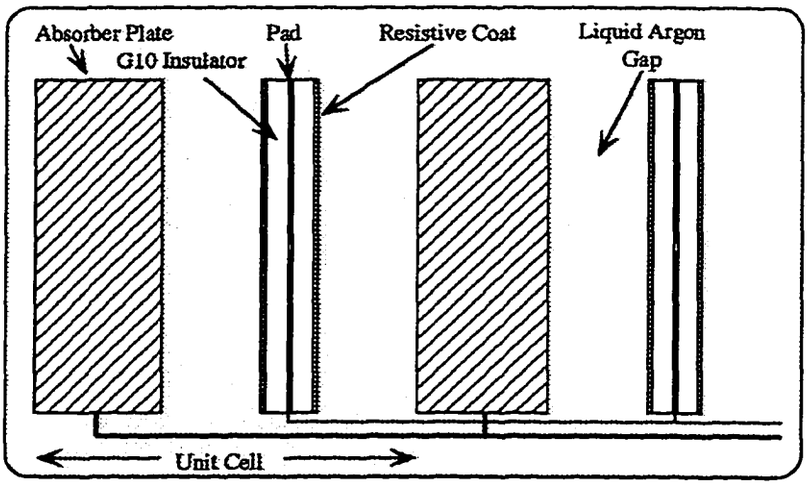


Figure 3.10 A typical calorimeter unit cell.

deposited energy.

### The Intercryostat and Massless Gap Detectors

In the region between the CC and EC calorimeters there is a large amount of dead (unsampled) material. Most of the material is the cryostat walls, calorimeter support, and cabling for detector readout. To better sample this region, scintillation detectors have been mounted to the front end of each of the EC cryostat walls. Each inner cryostat detector (ICD) has 384 scintillator tiles of size $\eta \times \phi = 0.1 \times 0.1$ matching the calorimeter's pseudoprojective tower structure. Within the CC and EC cryostats, 512 additional scintillator tiles are added called the massless gap (MG). The two additional detectors reduce missing transverse energy in multijet events by roughly 40% [20].

## Muon Spectrometer

The outermost detectors for DØ are the muon spectrometer's SAMUS (small-angle muon system) and WAMUS (wide-angle muon system). Muons and neutrinos are the only particles that can pass through the uranium-liquid argon calorimeter. The neutrino transverse energy is measured indirectly by the calorimeter by requiring $E_T$ balance in the event. The calorimeter detects the muon through small minimum ionizing deposits in the calorimeter, but the muon does not shower like an electron. The muon's mass is ~200 times larger than the electron's, thus the muon's bremsstrahlung radiation is about $(1/200)^4$ less energetic since the rate of radiation is porportional to the acceleration of the particle to the fourth power. Therefore the muon momentum measurement can only be made by the muon spectrometer.

The DØ muon spectrometer (Fig. 3.11) consists of 5 iron-yoked toroids of field strength varying from 1 to 2 Tesla. There is one set of proportional drift tubes (PDT) before to the magnetic field (layer A) and two sets of PDT's after the field (layer B and C) [21]. The muon montemum is calculated using the muon hit postions in the three PDT layers. The angular resolution of the PDT's is about 3°. The momentum resolution of the muon is limited by multiple coulomb scattering in the iron toriods to $\geq$ 18%. The central muon system is WAMUS (wide-angle muon system) covers the region of $|\eta|<1.7$. The forward muon system SAMUS (small-angle muon system) covers the region of $1.7<|\eta|<3.6$. Table 3.6 has some relevant information about the muon system.

## Data Aquisition

At DØ $p\bar{p}$ beam crossings occur every 3.5 $\mu$sec, which gives an event rate of 286,000 Hz. Interesting physics though, only occurs a small fraction of the time, so events must be carefully picked from the "haystack". The means by which event

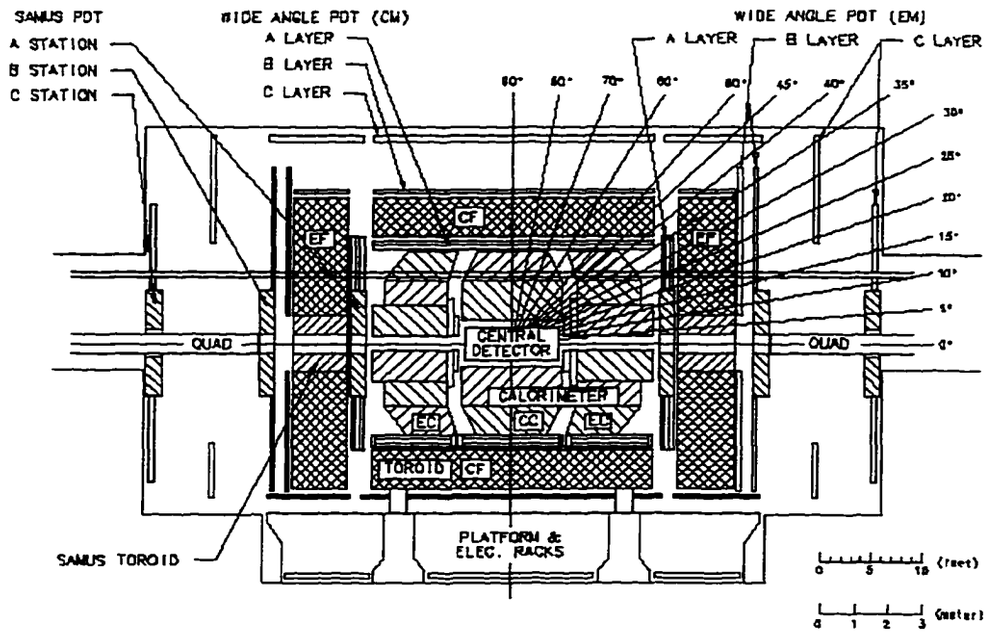


Figure 3.11 The y-z view of the muon system.

rates are reduced intelligently is called "triggering". The DØ trigger system has the daunting task of reducing 286,000 Hz down to a final usable rate 2 Hz. that is a factor of 143,000!

The DØ trigger system has three triggering levels level Ø, level 1, and level 2. The level Ø trigger simply requires a non-diffractive inelastic collision, which reduces the event rate to about 100,000 (this depends upon instantaneous luminosity). The level 1 trigger can make event requirements such as $E_T$ of EM-hadronic calorimeter towers, $p_T$ of muons, number of calorimeter towers above $E_T$ threshold, calorimeter $E_T$ imbalance (missing $E_T$), and so on. The level 1 trigger makes most of the decisions between beam crossings, so reducing the event rate by a factor of about 1000. and the passing rate is about 100 Hz. The level 2 trigger is a parced down version of final event reconstruction programs. This level of triggering is much more specific. Requirements can be made on the $E_T$ of an EM cluster, $E_T$ of a jet, $\eta$ requirements.

Table 3.6 The muon spectrometer parameters.

| Parameter | WAMUS | SAMUS |
|---|---|---|
| $\eta$ Coverage | $\pm 1.7$ | $\pm(1.7-3.6)$ |
| Magnetic Field | 2 T | 2 T |
| Nuclear Interaction Length | $\sim$ 13.4 | $\sim$ 18.7 |
| Number of Modules | 164 | 6 |
| Number of Drift Cells | 11,386 | 5308 |
| Sense Wire Parameters | 50$\mu$m Au-plated W | 50$\mu$m Au-plated W |
| Sense Wire Voltage | +4.6 kV | +4.0 kV |
| Cathode Pad Voltage | +2.3 kV | +2.3 kV |
| Gas | 93%Ar, $\sim$5%$CF_4$, $\sim$5%$CO_2$ | 90% $CF_4$, 10% $CH_4$ |
| Drift Velocity | $\sim$ 6.5 cm/$\mu$sec | $\sim$ 9.7 cm/$\mu$sec |
| Bend View Resolution | $\pm$ 0.53 mm | $\pm$ 0.35 |
| Non-Bend View Resolution | $\pm$ 3.0 mm | $\pm$ 0.35 mm |

and so on. Due to the more complex decisions, the level 2 trigger makes the decisions in about 0.3 seconds, so reducing the event rate by a factor of about 50. and the passing rate is about 2 Hz.

### Level Ø Trigger

The level Ø trigger [22] detects $p\bar{p}$ inelastic collisions. It uses two hodoscope scintillator counters which are mounted on the end calorimeters near the beam line. When both of the scintillators detect some excessive number of hits in a correct time slice, this signifies the breaking up of the $p\bar{p}$ pair, and that a non-diffractive inelastic collision has taken place. The two hodoscopes have timing resolutions of 100 ps. Therefore, the level Ø trigger determines the z-position of the interaction point to an accuracy of 3 cm. This information is passed on to the level 1 and level 2 triggers for $E_T$ calculations.

One final, but very important, job that the level Ø system does is calculate the instantaneous luminosity ($\mathcal{L}(cm^{-2}s^{-1})$) of the $p\bar{p}$ interactions. This is calculated by measuring the rate of inelastic collisions per beam crossing and by knowing the cross

section for inelastic collsions. Further, by integrating the $\mathcal{L}$ over time ($\int \mathcal{L} dt$), we can calculate the cross sections for all physical processes and test the standard model.

### Level 1 Trigger

The level 1 trigger [23] is a programmable hardware trigger, that reduces the event rate by a factor of 1000. Further, most of the level 1 triggering decisions are made within the beam crossing time of 3.5$\mu$sec. At level 1, only calorimeter and muon detector information is used. The triggers are constructed using a 256 bit "term" list. Each "term" can be turned on or off, and in addition and/or qualities can be used with the terms. The terms list types of level Ø, calorimeter, and muon event requirements. For example, one term might be: require 1 EM calorimeter tower with $E_T > 10GeV$, or require 1 muon with $| \eta | < 1.0$, or require an "inelastic collision". The triggers are constructed using the 256 terms, and we can easily have 4 or 5 term requirements. DØ uses 32 triggers for each run of data taking. Each of these triggers is suited to identify some particular high energy phenomenon. Some physical processes, though, are so copiously produced that the process must be pre-scaled, which simply means that only 1 out of N produced events of this process are kept. The trigger list is easily modified, and the prescales are changed throughout a run, reflecting the falling $\mathcal{L}$, and thus the falling event rates.

The level 1 calorimeter trigger defines energy clusters as longitudinal "towers" with transverse dimensions of $\Delta\eta \times \Delta\phi = 0.2 \times 0.2$ and constructs the towers out to $| \eta | = 4$. The calorimeter towers read out to a total of 1280 EM calorimeter and 1280 fine hadronic towers. The analog tower energy is estimated from an analog signal taken from the base-line-subtraction cards (BLS) trigger pickoffs and are "FLASH" analog to digital converted to 8 bit digital signals. A digital 3 bit z-position is passed to level 1 from level Ø. Some physical quantities are calculated:

- EM $E_T$ towers.

- hadronic $E_T$ towers,
- total EM and/or hadronic $E_T$ of calorimeter($H_T$), and
- total $\not\!\!E_T$(missing $E_T$).

The muon level 1 trigger receives 1 bit from each of the 16,700 PDT cells. The bit is a yes/no qualifier for a hit in that particular cell. This gives a hit positional resolution of about 5 cm. The level 1 muon trigger checks the hits to see if they are consistent with a muon coming from the interaction region. The muon level 1.5 trigger makes a rough $p_T$ calculation for all found muons. This process can take about 5-100 $\mu$sec, and can introduce some data selection "dead-time".

At the level 1 triggering, events start to take the shape of our final event ensemble (i.e. we can select photons, electrons, jets, $\not\!\!E_T$, and muons). If the event passes one of the thirty-two allowable triggers, all of the central detector, calorimeter, and muon analog signals are digitized and sent to the level 2 trigger processing farm.

### Level 2 Trigger

The level 2 trigger [24] is a software-driven event filter. It takes 48 vaxstations about 1/3 of a second to reduce the input rate of 100 Hz down to an output rate of 2 Hz. The event filtering is built around a series of filter tools. The tools are streamlined versions of the actual event reconstruction routines. The idea is to save time at the expense of having superb reconstruction accuracy. Each tool has a particular function, such as identification of jets, EM clusters, or muons. Further tools can look for general event topologies such as $E_T$, $\not\!\!E_T$, $H_T$, or a track associated with an EM cluster. The tools are scripted together and work off a particular level 1 trigger bit. The script can create many level 2 filters, thus it is reasonable to have several level 2 filters working off the output of one level 1 trigger. (the level 1 trigger can be thought of as a starting point from which several level two filters can work from) For example, a

level 1 trigger requirement can be made that two EM towers with $E_T > 10$ GeV are detected. Using the output from level 1 could be several level 2 filters: one level 2 filter can require two EM clusters that have an $E_T > 15$ GeV, and both EM clusters have an associated track; a second level 2 filter could require two EM clusters that have an $E_T > 15$ GeV, both EM clusters are energy isolated, and that the event has $\not\!\!E_T$>30 GeV. Several other level 2 filters can work off the same level 1 trigger output. The virsatility of level 2 filters allows the physicists at DØ study many aspects of particle physics. There are 128 level 2 filters avaliable. If the event passes any one of the level 2 filters, and passes the trigger prescale, this "special" event is written out to tape.

## Summary

The road for a unique high energy physical process to be detected and saved to tape is long and arduous. If one part of the detection chain fails (even partially), the physics that can be studied is reduced. So every attempt is made and much work is done to consistently calibrate and test this 70 million dollar microscope.

# 4 EVENT RECONSTRUCTION AND PARTICLE IDENTIFICATION

## DØRECO

The raw information from a $p\bar{p}$ collision consists of thousands of ADC counts from each detector system. Obviously, the counts are meaningless unless they are properly "coordinated" with all detector systems. The process in which all the electronic signals are "coordinated" is called event reconstruction. The event reconstruction software recognizes patterns within all of the raw ADC counts and reconstructs physics-objects (photons, electrons, muons, jets, and missing transverse energy). The reconstruction software used by DØ is called DØRECO, and this pattern recognition software calculates all the relevant information for physics analysis.

### Vertex and Track Reconstruction

An important task that DØRECO must perform is finding the $p\bar{p}$ interaction point (IP), or vertex. The accuracy of the vertex measurement is important, since all calculated quantities depend upon this single measurement.

The collided proton-antiproton bunches are gaussian distributed and have a cylindrical like shape. The bunch's diameter is about d = 50$\mu$m and length is about $\delta$z $\sim$ 30 cm. Therefore, the x-y coordinate is well defined from run to run due to the diameter of the collided proton-antiproton bunches. The x-y IP position is known to about 50$\mu$m. Due to the length of the proton-antiproton bunches, the z coordinate of

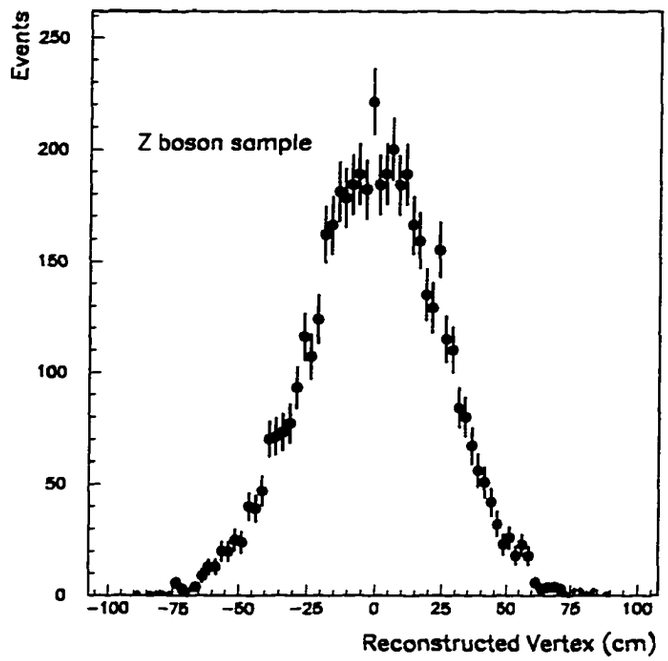


Figure 4.1 The reconstructed z-coordinate vertex position for Z boson events.

the interaction point is not well constrained and must be measured for each event. A single run's z coordinate IP point has a mean of nearly zero and is distributed like a gaussian with a width of about 30 cm as seen in Figure 4.1. The vertex z position is constructed by using the central drift chamber detector. It starts by reconstructing the hit positions from dE/dx and timing information from the CDC chambers. The hits from every CDC layer are used to construct charged particle tracks. The tracks are projected through the interaction region and an impact parameter is calculated. Only reconstructed tracks with an impact parameter less than some cutoff are used for vertex reconstruction. The projected tracks' z-positions are binned in a histogram and form a gaussian distribution where the interaction point is located. If multiple interactions took place the vertex with the most tracks pointing to it is the primary

vertex. Multiple vertices can be distinguished if they are about 8 cm apart. The uncertainty on the z-position of the vertex is less than about 2-3 cm event-to-event. If the interaction point is not found within $\pm 100$ cm from $z = 0$, the vertex z position is set to zero.

### Electromagnetic Object Reconstruction

Electromagnetic (EM) objects are reconstructed as localized energy deposits in the EM calorimeter. The EM objects are reconstructed by ranking the calorimeter EM towers from higher to lower transverse energies ($E_T$), with an minimum tower $E_T$ cutoff of 50 MeV. The $E_T$ ordered towers are called 'seed' towers, since they are the initial "seed" to the EM energy cluster reconstruction algorithm. Starting with the highest $E_T$ seed tower, a "nearest neighbor" algorithm [25] is used to sum the seed tower's neighboring towers' energy above some energy threshold. The centroid of the cluster is calculated using a log-weighted center-of-gravity method on the energy deposition in the EM calorimeter's third layer. The position of the shower is calculated to an accuracy of about 2 mm. A cluster is classified as an EM object if 90% of the EM object's energy is in the EM calorimeter and at least 40% of the cluster's energy is in one tower. The EM cluster is identified as an electron if the central detector has a reconstructed track between the cluster and the IP within a cone of radius $\Delta R = 0.2$, where $\Delta R = \sqrt{\Delta\eta^2 + \Delta\phi^2}$. If no track is found the cluster is identified as a photon.

The EM energy scale is determined using $Z \rightarrow e^+e^-$, $J/\psi \rightarrow e^+e^-$, and $\pi^\circ \rightarrow \gamma\gamma$ events. Since the masses of the Z boson, $J/\psi$, and $\pi^\circ$ are known to great accuracy, the DØ EM energy measurement is simply scaled to the proper value.

### Jet Reconstruction

Jet reconstruction uses both the EM and hadronic parts of the calorimeter. Using the EM calorimeter is reasonable since much of the hadrons final decay products are photons. The remaining hadronic particles will generally pass through the relatively thin EM calorimeter and shower within the hadronic portion of the calorimeter. As mentioned, hadronic showers are much larger longitudinally and transversely. Further hadronic showers have larger fluctuations than than EM showers and therefore a cone algorithm is used for jet clustering [26]. The randomness of the hadronic shower makes the choice of a cone algorithm much more reasonable, since all the energy within a region will be summed with no dependance upon cell-to-cell energy differences.

Initially, calorimeter towers are $E_T$-ordered from higher to lower $E_T$. Starting with the highest seeded tower, a precluster is formed by summing the energy of adjacent towers in $\eta$ and $\phi$ that have an $E_T > 1$ GeV. This process is continued out to a radius $\Delta R = 0.4$ from the seed tower. The precluster centroid is found using an $E_T$-weighted method. Preclustering continues until all seed towers are exhausted.

The preclusters are $E_T$-ordered and a final cone algorithm is used. Three cone sizes are used at DØ: $\Delta R = 0.3$, 0.5, and 0.7. The preclusters are reconstructed from highest to lowest $E_T$, and all the energy is summed within the cone. If a following precluster is within $\Delta R = 0.5$ of a reconstructed jet, that precluster is skipped. Similarly, the jet's centroid is found using an $E_T$ weighted method. The $E_T$-weighted process is cyclic, and will continue to iterate until the reconstructed jet axis stabilizes. If the jet has an $E_T$ less than 8 GeV, the jet is not recorded. After all of the jets have been reconstructed, some cells are assigned to two separate jets. It is common that jets share similar towers, therefore jet splitting and merging must be completed. If the shared towers have greater than 50% of the smaller jet's $E_T$, then the jets are merged, and otherwise they are split.

Due to jet energy measurement inefficiencies, the jet energy scale must be corrected. An uncorrected jet's $E_T$ is typically measured 10-15% less than the true value. There are three main sources of mismeasurement: the underlying event energy from the remnant proton-antiproton pair can falsely increase the reconstructed jets energy, and this is removed; secondly, since a cone algorithm is used for jet reconstruction, some energy can fall outside of the cone and this is added; further, many low energy particles are produced during hadronization, and these particles are poorly measured, and their energy is added.

The corrections are calculated using direct photon events. The leading order production diagram for these events consist of 1 photon and 1 jet produced in the event. Therefore, no $\not\!\!E_T$ is expected and the calculated $\not\!\!E_T$ for these events are from jet $E_T$ mis-measurement [27]. The jet energy corrections are $E_T$ and $\eta$ dependant.

### Missing Transverse Energy Reconstruction

The weakly interacting neutrino will simply pass through the calorimeter, and is measured indirectly as missing transverse energy ($\not\!\!E_T$). The conservation of the z-component of an event's momentum can not be calculated, since the proton/antiproton remnants are unmeasured within the event. The transverse momentum of the colliding proton and antiproton is negligibley small though, and is constrained to equal zero. Therefore, a $\not\!\!E_T$ measurement is made using momentum conservation, and all $\not\!\!E_T$ is associated with neutrinos or energy mis-measurement.

The $\not\!\!E_T$ is calculated first by determing the $\vec{E}_T$ of every calorimeter cell (this includes the the CC, EC, ICD, and the massless gaps). The $\vec{E}_T$ for each calorimeter cell is calculated using the energy measurement of the cell, plus the $\eta$ and $\phi$ direction of the cell from the vertex. The sum of every calorimeter cell's $\vec{E}_T$ is completed, and the negative value of this quantity is the $\not\!\!E_T$. If a muon is present in the event, the muon's $\vec{p}_T$ is summed along with the calorimeter cells and the negative value of this

quantity is the $\not\!\!E_T$. For an analyses particular interest, several types of $\not\!\!E_T$ are stored in the reconstructed event's $\not\!\!E_T$ bank.

### Muon Reconstruction

A muon is detected by recording both ionizing tracks in the central detector's drift chambers and by the muon systems's proportional drift tubes (PDT). Further, the calorimeter can be used as a 'tracker' since the muon will deposit 2-5 GeV of energy as it passes through the calorimeter.

The muon reconstruction starts by using the timing information from the hits in the muon PDT's. The hits from every layer are used to reconstruct the muon's track. A global fit is performed using the muon's reconstructed track, the reconstructed vertex, the energy deposition in the calorimeter, and the charged reconstructed track from the central detector. This is performed for every 'found' muon, and several quantities are kept in the muon bank so that an assessment can be made on the quality of the muon (such as a global fit $\chi^2$, number of PDT layers hit, and reconstructed track quality (IFW4)).

### Event Data Format

The output from each event is stored in a ZEBRA format as STA's, DST's, and $\mu$DST's, with each data format type being of smaller size, STA$\sim$ 500 Kbytes, DST$\sim$20 Kbytes, and $\mu$DST$\sim$2 Kbytes. Generally, the STA's are on tape and the DST's and $\mu$DST's are on disk. To further reduce the event file size, CERN software's PAW program is utilized to construct data ntuples. In short, the ntuples behave like a spreadsheet and were streamlined for my analysis. Therefore, I only keep physics information that is of use to me, and discard the rest. Thus, it only takes me a few minutes to run over a million events, instead of the 1 week it would take with the $\mu$DST's!

## Particle Identification

The output from DØRECO is a nice starting point from which physics objects can be selected. Further requirements are made that are effective at rejecting mimicking background objects, but are very efficient on real physics objects. This analysis selects photons, which have a significant QCD background source of $\pi^o$ and $\eta$ mesons. Therefore, this section is devoted to EM (photon) selection quality variables. The primary tools used to select photons from background are:

- electromagnetic fraction (EMF),
- transverse energy isolation (ISOL),
- EM shower shape ($\chi^2$),
- reconstructed track cut,
- excessive hits in road cut.

The first three listed quantities are used to describe the quality of the EM shower, thus their title 'EM quality variables'. The last two listed quantities are tracking variables and are used, for the most part, to distinguish photons from electrons. Each will be discussed in the following sections.

### EM Quality Variables

The EM quality variables used in this analysis are EMF, ISOL, and $\chi^2$. The use of all of these variables gives excellent discrimination of photons from jets.

The EMF of the photon is the intial tool for the selection of EM objects. DORECO's output photon bank requires an EMF' > 0.90, which is defined as:

$$\mathrm{EMF}' = \frac{E_{EM}}{E_{EM} + E_{FH1}}. \qquad (4.1)$$

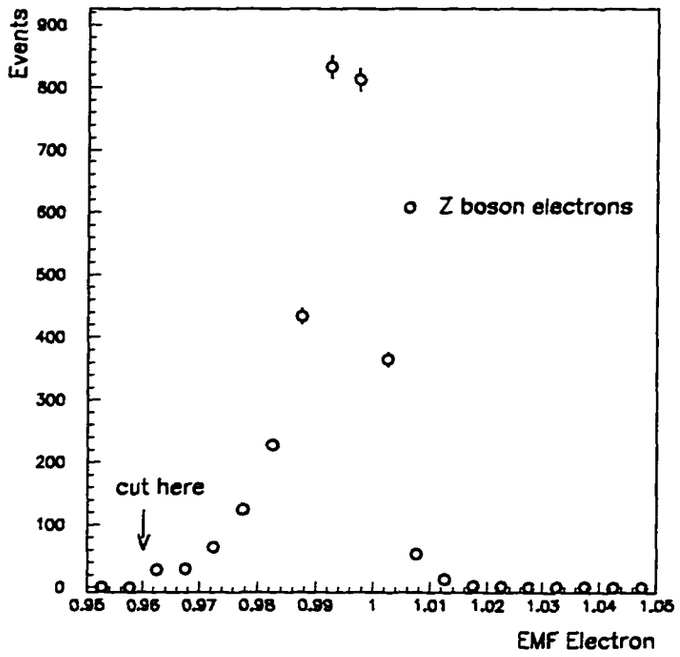


Figure 4.2 The EMF distribution for Z boson electrons form the run 1 data sample.

Here $E_{EM}$ is the energy measurement in the EM calorimeter and $E_{FH1}$ is the energy measurement in the fine hadronic calorimeter's first layer. Generally though, photons have a much higher EMF value. This analysis uses a slightly different definition of EMF.

$$EMF = \frac{E_{EM}(\Delta R = 0.2)}{E_{EM}(\Delta R = 0.2) + E_{Hadronic}(\Delta R = 0.2)}, \tag{4.2}$$

where all the energy in the hadronic calorimeter is used within a cone of radius $\Delta R = 0.2$. This analysis requires an EMF $> 0.96$, which is reasonable as seen in Figure 4.2. The Z boson decay electrons are used throughout this analysis as a consistency check for EM variables, since electron and photon showers are nearly identical within the EM calorimeter and are distinguished from each other by tracking.

Energy isolation is another way to discriminate a "real" photon from $\pi^0$ and $\eta$

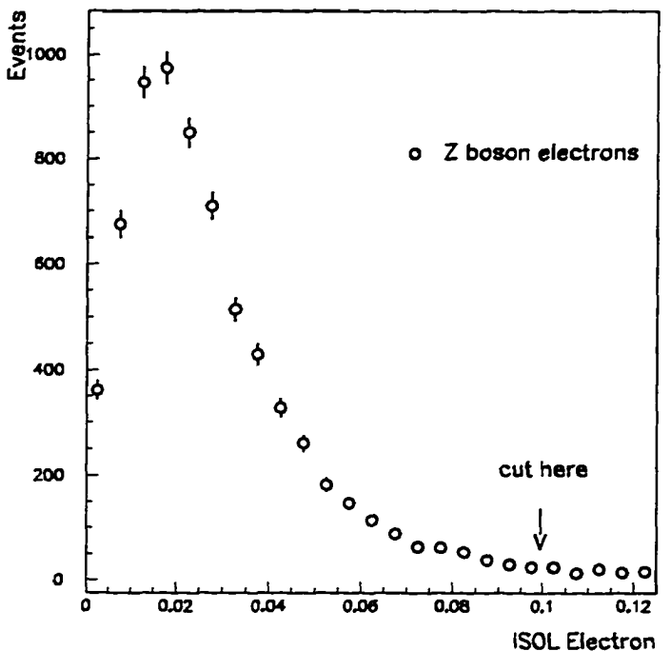


Figure 4.3 The ISOL distribution for Z boson electrons form the run 1 data sample.

meson decays. The mesons are from a hadronic shower, therefore they will have more hadronic energy activity or noise, associated with them, while photons from a direct Higgs decay or even direct photon production would have significantly less hadronic noise.

The ISOL parameter is defined as:

$$\mathrm{ISOL} = \frac{E_T^{photon}(\Delta R = 0.4) - E_T^{photon}(\Delta R = 0.2)}{E_T^{photon}(\Delta R = 0.2)} \tag{4.3}$$

and measures the fraction of energy deposited within an annulus of outer radius R = 0.4 and inner radius of R = 0.2. The photon candidate is accepted if ISOL $< 0.10$, which is reasonable as seen in Figure 4.3.

The final EM quality variable used is the $\chi^2$ likelihood parameter. The $\chi^2$ parameter has $\chi^2$ like behavior and describes the likelihood that the EM shower's longitudinal

and transverse shape is consistent with test beam electron's shower shape.

The $\chi^2$ parameter is derived from the building of a 41x41 covariance matrix. Each entry in the matrix is built from EM shower observable quantities, such as the fraction of energy in the EM calorimeter layers 1, 2, 3, and 4, and the distribution of energy in the third layer of the EM calorimeter. Further DØ has a known set of electrons and pions from test beam data and Monte Carlo simulations, so that the matrix can be tuned to discriminate electrons from pions. The matrix is defined as:

$$M_{ij} = \frac{1}{N}\sum_{n=1}^{N}(x_i^n - \bar{x}_i)(x_j^n - \bar{x}_j). \tag{4.4}$$

Here $x_i^n$ is the value of the observable i for electron n, and $\bar{x}_i$ is the mean value of the observable i from the electron sample. Several $M_{ij}$ matrices were calculated at different pseudorapidities to account for the $M_{ij}$ $\eta$ dependance. The calculation of the $\chi^2$ parameter for every EM candidate is done by inverting the $M_{ij}$ matrix and summing over the product of the observable deviations from the mean.

$$\chi^2 = \sum_{i,j}(x_i^k - \bar{x}_i)(M_{ij})^{-1}(x_j^k - \bar{x}_j). \tag{4.5}$$

The $\chi^2$ parameter is a nice rejection tool for pions. The $\chi^2$ distribution for a sample of Z boson electrons is shown in Figure 4.4.

### Tracking Variables

As mentioned previously, the only discernable difference between photon and electron showers is the tracking. Therefore, this section will explain the steps taken to reject electrons from the signal sample.

The first step for selecting photons from the EM sample is requiring no reconstructed track in the EM cluster's tracking road. The tracking road is defined as a cone of radius $\Delta R = 0.2$ with the axis projecting from the reconstructed vertex to the EM cluster's centroid. The efficiency for track reconstruction has been calculated

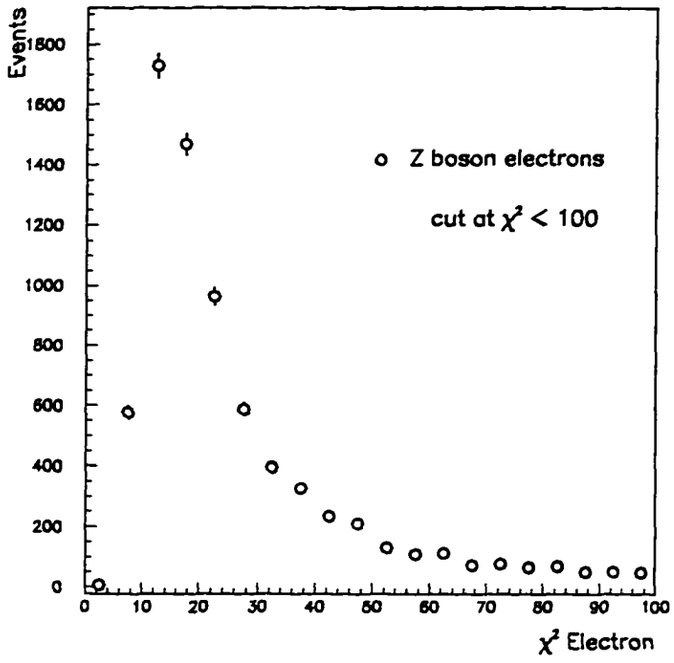


Figure 4.4 The $\chi^2$ distribution for Z boson electrons from the Run 1 data sample.

in Appendix C and is stated as:

$$\epsilon_t = 0.80 \pm 0.02,$$

for both the central and forward drift chambers [28]. Since this analysis is interested in photons, not electrons, the efficiency can be thought of as a rejection factor for electrons. The rejection factor is defined as,

$$R_t = \frac{1}{1 - \epsilon_t}, \tag{4.6}$$

thus

$$R_t = 5 \ .$$

The inefficiency of track reconstruction will let 1 out of every 5 electrons pass into the photon sample. By using the HITSINFO utility [29] a much larger electron rejection

Table 4.1 The HITSINFO tracking volume parameters.

| Detector | $\Delta\theta$(rad) | $\Delta\phi$(rad) |
|---|---|---|
| VTX | 0.005 | 0.012 |
| CDC | 0.05 | 0.0075 |
| FDC | 0.005 | 0.015 |

Table 4.2 The HITSINFO requirements for every EM candidate.

| Vertex Chamber | |
|---|---|
| RHVTXW $< 0.3$ | |
| NHVTX3D $\leq 8$ | |
| Central Drift Chamber | Forward Drift Chamber |
| RHCDCW $< 0.3$ | RHFDCW $< 0.7$ |
| NHCDCXY $\leq 20$ | NHFDCXY $\leq 30$ |
| NHCDC3D $\leq 1$ | none |
| NHCDCZS $= 0$ | none |

factor can be obtained.

The HITSINFO utility constructs a smaller tracking road than that used in tracking, sums all the hits found in the road, repeats this for every reconstructed vertex, and keeps the largest number of found hits. A 'hit' is defined as a drift chamber wire current pulse caused by the passage of a charged particle and the cycling over every vertex is completed so that misvertexed events will be accounted for. The HITSINFO road size is defined in Table 4.1 and the HITSINFO requirements are listed in Table 4.2. Here RHVTXW is the percentage of vertex wires hit, NHVTX3D is the number of 3d hits in road, RHCDCW/RHFDCW is the percentage of CDC/FDC wire hits in road, NHCDCXY/NHFDCXY is the number of CDC/FDC XY hits in road, NHCDC3D is the number of CDC 3d hits in road, and NHCDCZS is the number of CDC z-segment hits in road. The HITSINFO requirements used are standard at DØ and were used in other studies [30, 31]. The HITSINFO requirements reject electrons by a factor

of $R_h = 30 \pm 10$ [29]. The total electron rejection factor is just the product of the tracking rejection ($R_t$) and the hits rejection ($R_h$), which is $R_{h+t} = 150 \pm 50$ per electron. The electron pollution of the final signal sample is very small and will be calculated later.

### Summary

In summary, an EM object is only called a photon candidate after it has passed the following criteria,

- EMF $> 0.96$,
- ISOL $< 0.10$,
- $\chi^2 < 100$,
- no reconstructed track,
- no excessive number of hits in tracker,

and even with these tight requirements, a significant number of $\pi^\circ$ and $\eta$ mesons pass into the photon sample. The $\pi^\circ$ and $\eta$ meson background is discussed thoroughly in later sections and will be referred to as QCD multijet background.

# 5 THE ANALYSIS

The discussion will focus on the complete analysis of the search. The motivation for the search was discussed at the end of Chapter 2.

## Data Selection

The final state of interest consists of two photons and two jets having large transverse energy and centrally located. Additionally, the dijet mass is consistent with the W or Z boson, the two photons are well isolated from the jets, and the diphoton invariant mass is large. The events will be collected using a diphoton filter, which will reduce the sample sizes considerably since diphoton events are in general rare.

### Event Triggering

The level Ø requirement for the selected events is that the level Ø hodoscope must detect a $p\bar{p}$ inelastic collision. The level Ø requirement is very efficient and has a calculated efficiency of 99%. The level 1 trigger used is EM_2_MED, which requires two EM towers with an $E_T$ greater than 7 GeV. The level 2 trigger used for Run Ia was GAM_2_MED, for Run Ib was EM2_GIS_GAM, and for Run Ic was EM2_GIS_GAMA. The level 2 filters require:

- 2 EM showers with $E_T > 12$ GeV,
- 1 EM shower (GAM requirement), and
- 1 EM shower with Energy Isolation (GIS requirement).

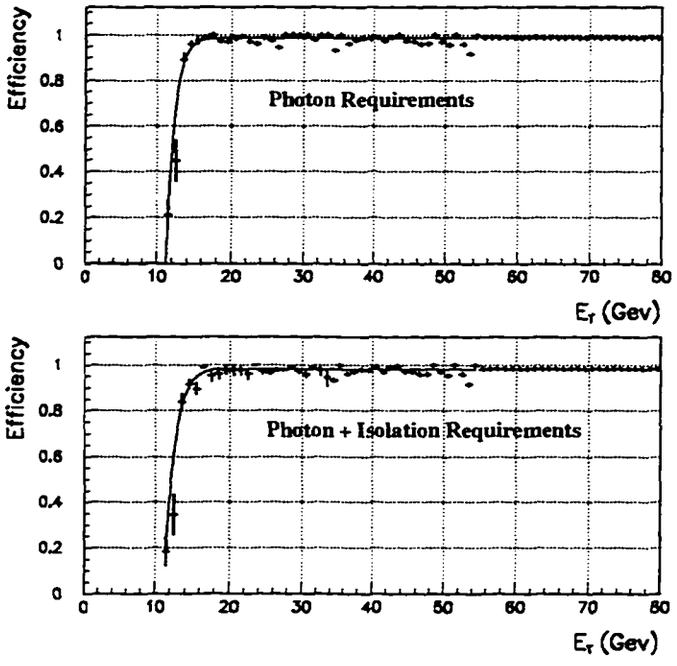


Figure 5.1 The trigger "turn-on" curves for the GAM (top plot) and GIS (bottom plot) parts of the EM2_GIS_GAM level 2 filter.

The level 2 GAM part of the filter requires that the EM shower is consistent with a photon and the level 2 GIS part of the filter requires a GAM requirement plus energy isolation on the shower. The Run Ia trigger had only a double GAM requirement, no isolation requirement. The run Ic level 2 trigger is identical to the run Ib trigger, it just had an 'a' added to its title. The trigger efficiencies have been calculated elsewhere [32], and both parts of the level 2 filter are fully efficient ($\epsilon > 95\%$) when both photons have an $E_T$ greater than 15 $GeV$ as shown in Figure 5.1.

Using the DØ luminosity utilities, the integrated luminosity has been calculated. The Run I level 2 filters have a total integrated luminosity of $101.2 \pm 5.5\ pb^{-1}$. The sources of the 5.5% error on the integrated luminosity are the following errors added in quadrature: the uncertainty in the $p\bar{p}$ minimum bias cross section of 4.6%, the

Table 5.1 The general event selection criteria.

| General Event Requirements |
|---|
| $\mid Z_{vertex} \mid < 75cm$ |
| $N_{em} \geq 2$ |
| $E_T^{em} \geq 15$ GeV |
| $\mid \eta_{em} \mid \leq 1.1$ or $1.5 \leq \mid \eta_{em} \mid \leq 2.5$ |
| $\chi^2_{em} \leq 100$ |
| EMF $\geq 0.96$ |
| ISOL $\leq 0.10$ |
| $N_{track} = 0$ |
| $N_{jet} \geq 2$ |
| $0.05 \leq EMF_{jet} \leq 0.95$ |
| $\mid \eta_{jet} \mid \leq 2.5$ |
| $E_T^{jet} \geq 15$ GeV |
| $dR_{em\ jet} \geq 0.7$ |
| Reconstruct events with DØreco 12.22 |
| EM objects pass HITSINFO cuts |

Monte Carlo uncertainty of 2%, and the small amount of uncertainty from the level Ø detector.

### General Event Selection

A complete listing of the general event requirements are shown in Table 5.1. The Run I event samples have been reconstructed with several versions of DØRECO. The latest event reconstruction version, DØRECO version 12.22, has the full HITSINFO bank information needed for event selection. Therefore, before the HITSINFO requirements are applied all of the remaining events are reconstructed with DØRECO version 12.22. DØRECO version 12.22 also has a DØFIX routine that improves event reconstruction. DØFIX made modifications to several reconstructed objects, such as EM objects, jets, and vertex finding. Two changes of importance to this analysis are: a noticeable change in vertex reconstruction, and only a slight difference in EM shower centroid calculations. The improvement in vertex reconstruction will improve

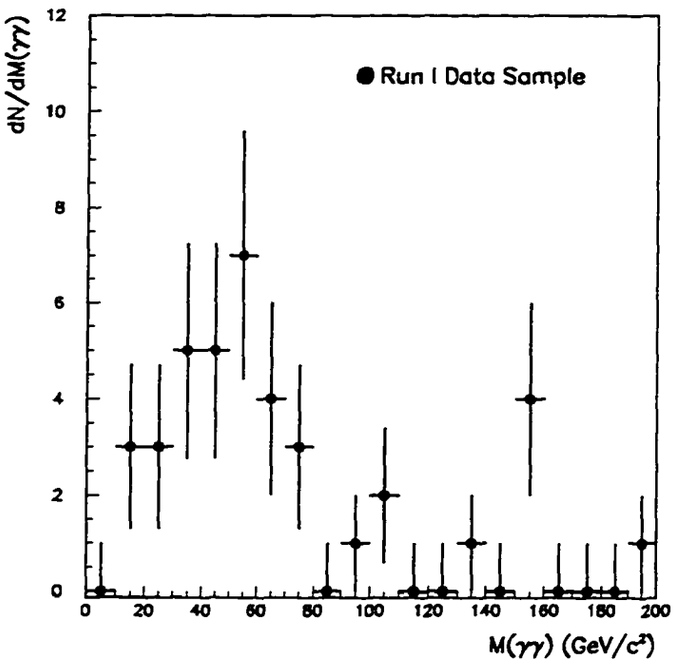


Figure 5.2 The Run I data sample with the general event requirements.

the analysis as a whole, since every selection criterion is dependent on this single measurement.

A diphoton invariant mass distribution with the general event requirements is shown in Figure 5.2. The distribution is reasonable, but there is an upward fluctuation in the number of events around 155 GeV/$c^2$. The expected number of events is about one per 10 GeV/$c^2$ bin width and four are seen. The four interesting events are discussed in Appendix A.

## Background

The dominant background in the $\gamma\gamma jj$ channel is QCD multijet events, where two jets mimic two photons. During the jet fragmentation process, $\pi^0$ and $\eta$ mesons

are produced and will promptly decay into multiple photons. If the mesons have an $E_T$ greater than about 10 GeV the photons will coalesce and mimic a single photon. The handle on these events comes from the longitudinal shower profile. The meson's multi-photons generally shower sooner in the electromagnetic calorimeter than a single photon would. A thorough study of EM candidates' longitudinal shower shape has been completed to estimate the jet misidentification rate, and is discussed in Appendix B. The probability for a jet to fragment into an isolated photon($P(j \rightarrow "\gamma")$) is of the order of a few times $10^{-4}$. $P(j \rightarrow "\gamma")$ is small, but the multijet cross section is so very large that this background is still significant. A rough calculation of the number of expected QCD multijet events for the general selection criteria is.

$$N(\gamma\gamma jj) = \{\sigma(\text{prod}) \times A\} L_{\text{int}} \{P(\text{jet} \rightarrow \gamma)\}^2$$

$$N(\gamma\gamma jj) = (2.0 \times 10^6 \text{ pb})(100 \text{ pb}^{-1})(1.9 \times 10^{-7})$$

$$N(\gamma\gamma jj) = 38 \pm 19 \text{ events.}$$

Here $\sigma$ is the production cross section, $L_{int}$ is the integrated luminosity, $\epsilon$ is the efficiency and A is the acceptance of a $\gamma\gamma jj$ event, and $P(jet \rightarrow "\gamma")$ is the probability for a jet to fragment into an isolated photon. The second, and smaller, source of background is single and double direct photon production. Direct photons are produced during the initial or final state partonic processes. The photons are not 'direct' if they are produced during the fragmentation process. The expected number of double direct photon events expected for the general event requirements is,

$$N(\gamma\gamma jj) = \sigma(\text{prod}) L_{\text{int}} A\epsilon$$

$$N(\gamma\gamma jj) = (100 \text{ pb})(100 \text{ pb}^{-1})(0.0018)(0.275)$$

$$N(\gamma\gamma jj) = 5 \pm 1 \text{ events}$$

and for single direct $\gamma$ production is,

$$N(\gamma\gamma jj) = \sigma(\text{prod}) L_{\text{int}} AP(\text{jet} \rightarrow \gamma)\epsilon$$

$$N(\gamma\gamma jj) = (88610 \text{ pb})(100 \text{ pb}^{-1})(.0015)(.00043)(.52)$$

$$N(\gamma\gamma jj) = 3 \pm 1 \text{ events.}$$

This analysis uses a floating 10% isolation requirement on the EM objects, unlike the analysis shown in Appendix B which uses a flat 2 GeV isolation requirement. For either method the $P(jet \rightarrow \text{“}\gamma\text{”})$ values should be equal for 20 GeV $E_T$ jet, since an isolation requirement of 10% on a 20 GeV EM object is 2 GeV. By using the floating 10% isolation requirement, much of the $E_T$ dependence is lost [33], thus it is reasonable to use a constant $P(jet \rightarrow \text{“}\gamma\text{”})$ value. The $P(jet \rightarrow \text{“}\gamma\text{”})$ used is the convoluted value for a CC and EC 20 GeV jet. The $P(jet \rightarrow \text{“}\gamma\text{”})$ is calculated as $(4.3 \pm 1.0) \times 10^{-4}$.

Other sources of background would be the $Z \rightarrow e^+e^- + 2$ jets, $W\gamma \rightarrow e^{\pm}\nu\gamma + 2$ jets where a track is lost on the electron, and $t\bar{t} \rightarrow e^+e^-\nu\nu + 2$ jets where both the tracks are lost. Without the HITSINFO this background is about 1.5 events. With the additional HITSINFO requirements, only one out of thirty charged objects will pass into the sample. The HITSINFO will give a rejection factor of about $30^2$ for the above events, therefore the electron channels are minimal and disregarded.

Quick review, the expected number of background events calculated using Monte Carlo methods is $46 \pm 21$ events, and 39 events are observed in the signal sample. The large error on the expected number of events is largely due to the $P(jet \rightarrow \text{“}\gamma\text{”})$ uncertainty in the QCD multijet background calculation. The QCD multijet background is calculated using data-based and MC methods, while the double direct photon (DDP) and single direct photon (SDP) backgrounds are only calculated using

MC methods. All mass distributions that are shown include QCD multijet, DDP, and SDP backgrounds and they are called, generically, 'background'.

### Double Direct Photon Background

The double direct photon (DDP) channel is 11% of the total background and will be included in the expected number of background events. The expected number of DDP background events is calculated using PYTHIA5.7's single direct photon channels. The detector acceptance is simulated using PYTHIA5.7's LUCELL energy clustering software. LUCELL is parameterized so that it had similar jet and electromagnetic energy resolutions to DØ's calorimeter and, to reflect the real detector environment, includes initial state radiation, final state radiation, pile up events, and multiple interactions. The efficiency for two photons to pass the EM quality and tracking criteria is calculated using the Higgs MC sample and the clean tracking road efficiency value, respectively. The DDP background is normalized to the final sample using the following formula;

$$\frac{dN}{dM_{\gamma\gamma}} = \left\{\frac{n'}{N_T}\right\}\left\{\frac{\sigma(pythia \rightarrow \gamma\gamma)\cdot \mathrm{L}}{\triangle M_{\gamma\gamma}}\right\}\cdot\epsilon\ . \tag{5.1}$$

Here $\triangle M_{\gamma\gamma}$ is the mass bin width of the histogram, $n'$ is the number of events in one bin of width $\triangle M_{\gamma\gamma}$, L is the integrated luminosity ($\int \mathcal{L}dt$) of the EM2-filters, $\sigma(pythia \rightarrow \gamma\gamma)$ is the PYTHIA's production cross section for DDP event, and $\epsilon$ is the efficiency for both photons from the DDP event to pass the EM quality and tracking requirements. The uncertainty in the number of DDP events is 5% from the $\int \mathcal{L}dt$ uncertainty and 15% uncertainty in modeling the detector acceptance. The errors are added in quadrature and give a 16% total uncertainty in the number of DDP events.

### Single Direct Photon Background

The single direct photon (SDP) channel is about 7% of the total background and will be included in the expected number of background events. The $\gamma\gamma jj$ signature is produced by having one photon and three or more jets produced, and where one of the jets are misidentified as a photon. The probability $P(jet \rightarrow \text{“}\gamma\text{”})$ is known and is applied to every jet-photon mass combination and the net probability is summed. The expected number of SDP background events is calculated using PYTHIA5.7's single direct photon channels. The event selection efficiency and acceptance are calculated using LUCELL with the same methods as mentioned beforehand. The SDP background is normalized to the final sample using the following formula;

$$\frac{dN}{dM_{\gamma\gamma}} = \left\{\frac{n'}{N_T}\right\}\left\{\frac{\sigma(pythia \rightarrow \gamma)\cdot \mathrm{L}}{\triangle M_{\gamma\gamma}}\right\}\cdot P(jet \rightarrow \gamma)\cdot \epsilon\ . \qquad (5.2)$$

Here $\sigma(pythia \rightarrow \gamma)$ is the PYTHIA's production cross section for a SDP event and $\epsilon$ is the efficiency for one photon from the SDP event to pass the EM quality and tracking requirements. The error on the SDP events is 25% from the P(jet $\rightarrow$ "$\gamma$") uncertainty, 15% from the uncertainty in modeling the detector acceptance, and 5% integrated luminosity uncertainty. The errors are added in quadrature and give a 30% total uncertainty in the number of SDP events.

### QCD Multijet Background

The QCD multijet background is estimated using both data and Monte Carlo methods. The data-based method uses the same general event requirements for event selection, but requires that either EM candidate must fail an EMF, ISOL, or $\chi^2$ EM quality requirement. This will give a QCD enriched sample, since the photon candidate is likely a $\pi^0$ or $\eta$ meson.

The data-based QCD multijet background is normalized to the Higgs excluded region of my data sample, minus the DDP and SDP backgrounds which are $11.3 \pm$

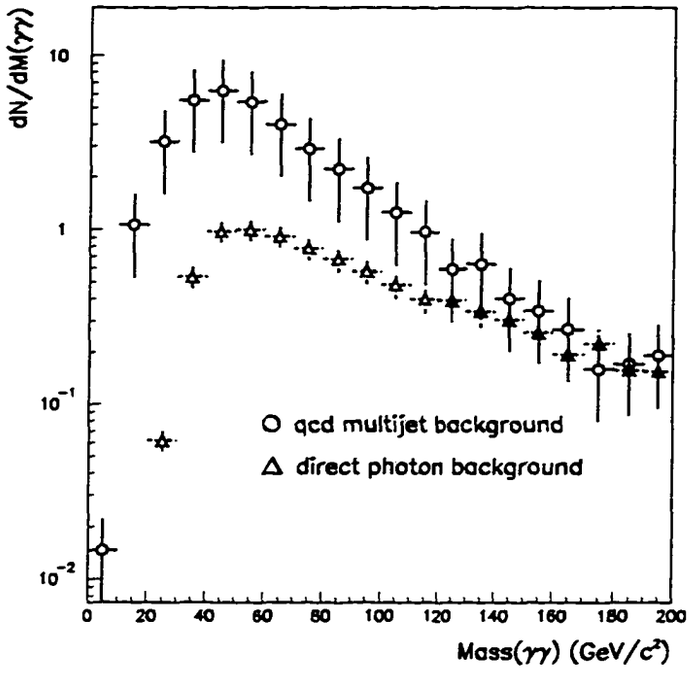


Figure 5.3 A comparison of the MC calculated QCD multijet and direct photon backgrounds.

2.0% of the total background in this region. A $M_{\gamma\gamma}$ comparison between the MC calculated QCD multijet backgrounds and the direct photon backgrounds are shown in Figure 5.3. To be clear, the data-based QCD background is normalized to:

$$N(\text{normalization}) = N_{\text{events}}^{\text{observed}}(M_{\gamma\gamma} < 60) - N_{\text{events}}^{\text{direct}\gamma}(M_{\gamma\gamma} < 60)$$

$$N(\text{normalization}) = (23 - (.113 * 23)) = 20.4 \pm 0.6 \text{ events.}$$

Therefore the signal and background samples have the same number of events for $M_{\gamma\gamma} \leq 60\ GeV/c^2$. For the general selection criteria, the data sample and background are plotted in Figure 5.4.

In a later section the signal sample's event selection criteria are optimized for a Higgs search. The data-based background is normalized similarly, but using the normalization number from the general event ensemble's normalization procedure.

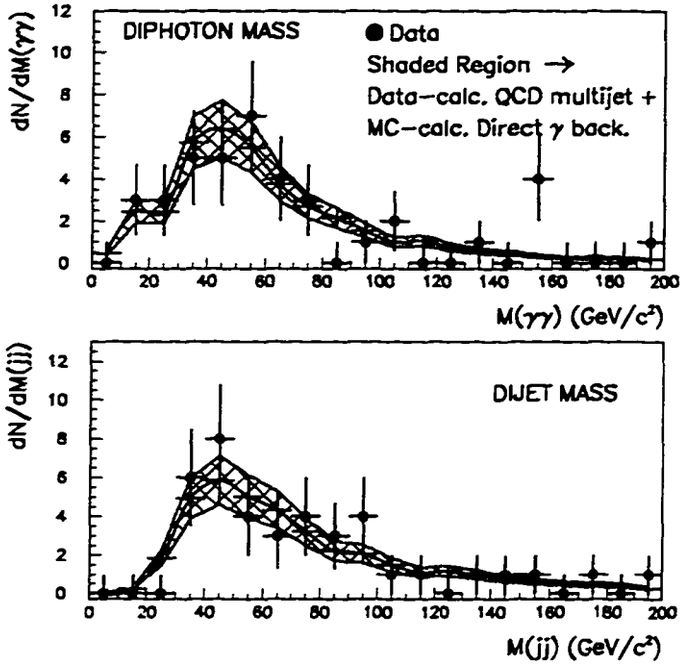


Figure 5.4 The Run I data with the general event requirements. The combined data-based QCD, MC DDP, and MC SDP backgrounds are shown as the shaded region. The central line is the nominal expected number of background events and the systematic error is the shaded region. The dominant error on the background is associated with the normalization procedure, and is 22%.

If the background sample truly represents what the signal sample is composed of, both samples should scale similarly with tighter event requirements. This is in fact seen in the optimization section of this paper. By using the general event ensemble's normalization number a reduction in the error on the expected number of background events in the final signal sample is acquired. The error is reduced since the background is normalize to 20 events instead of 4 events, thus the error is 22% instead of 50% ($\sqrt{N}/N$).

A second method of estimating the QCD multijet background was done using the PYTHIA event generator. Since the P($j \rightarrow \gamma$) is so small it is not reasonable to

GEANT, noise overlay, reconstruct, and ntuple all the generated events(on the order of 10 million events would need to be generated). Instead, PYTHIA's LUCELL energy clustering routine is used to cluster the jets. LUCELL was parameterized so that it had similar jet and electromagnetic energy resolution to DØ's calorimeter. The events were simulated from all of the leading order QCD multijet channels within PYTHIA. To reflect the real detector environment, initial state radiation, final state radiation, pile up events, and multiple interaction switches were turned on. Each PYTHIA event requires four LUCELL clusters to pass the 'kinematic' component of the event requirements. The four jets are treated as if two of the jets have fragmented into two isolated photons by weighting each jet of the $jet_i - jet_k$ event combination. $j_1j_2$, $j_1j_3$, $j_1j_4$, $j_2j_3$, $j_2j_4$, and $j_3j_4$, with $P(j \rightarrow \text{“}\gamma\text{”})$. In this case the $P(j \rightarrow \text{“}\gamma\text{”})$ is applied twice for each event combination. If either LUCELL-jet did not pass the photon kinematic requirements, $\eta_\gamma$, $E_T^\gamma$, etc., the probability for that combination was zero. All the event requirements are applied and each $jet_i - jet_k$ mass combination is binned for the background distribution.

The PYTHIA calculated QCD multijet background is normalized to the general event sample by using the following cross section formula.

$$\frac{dN}{dM_{\gamma\gamma}} = \left\{\frac{n'}{N_T}\right\}\left\{\frac{\sigma(pythia\text{QCD})\cdot \text{L}}{\triangle M_{\gamma\gamma}}\right\}\cdot\{P(jet \rightarrow \gamma)\}^2 \,. \qquad (5.3)$$

The Monte Carlo QCD multijet, DDP, and SDP backgrounds agree well with the event distribution as shown in Figure 5.5.

The two QCD multijet background calculated methods are compared with each other in Figure 5.6 and Figure 5.7. The photon and jet $\eta$ and $E_T$ distributions are normalized and agree fairly well. The error on the MC background is $\sim$50%, due to the uncertainty in $P(jet \rightarrow \text{“}\gamma\text{”})$. The larger $E_T$ regions in both $\gamma$ and jet distributions disagree slightly. The most likely cause of the difference my be due to incorrect calorimeter energy resolution functions on the MC photons and jets.

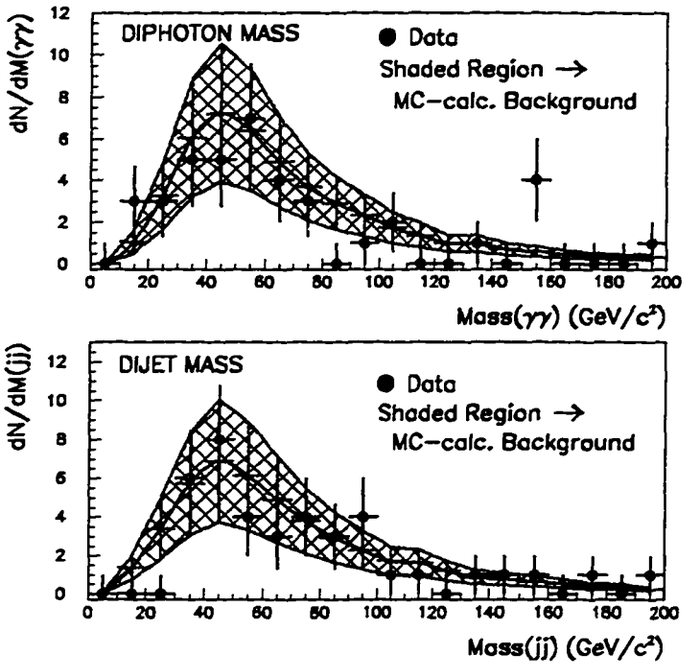


Figure 5.5 The Run I data sample with the general event requirements. The MC calculated number of QCD multijet, DDP, and SDP background events are the shaded region. The central line to the expected number of background nominally and the shaded region is the systematic uncertainty. The QCD multijet MC systematic error is 50% and is dominated by the P(jet→ "$\gamma$") uncertainty.

## Monte Carlo Signal Sample

Monte Carlo (MC) is essential for calculating the signal efficiences for $\gamma\gamma jj$ events. Initially $p\bar{p} \rightarrow HW$ and $p\bar{p} \rightarrow HZ$ events are generated using PYTHIA5.7, in which internal decay channel switches force the decays $H \rightarrow \gamma\gamma$ and $W/Z \rightarrow qq'$ exclusively. PYTHIA is a leading order event generator that correctly models all spin effects of the decaying $W$, $Z$, and $H$ particles. The proton and antiproton structure function used is CTEQ3M , but using several other structure functions little change is seen. Seven ensembles of 5000 events each are generated, with Higgs masses of 60, 70, 80, 90, 100,

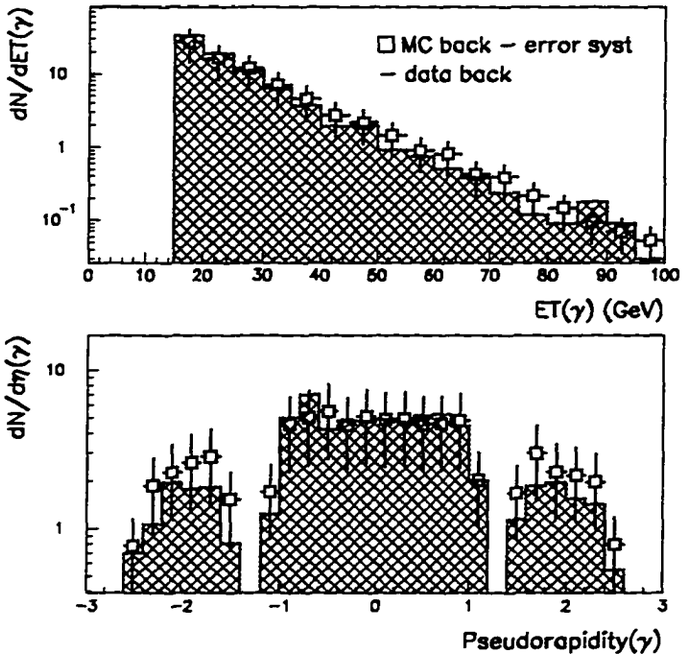


Figure 5.6 Comparing the photon kinematic variables of the calculated data-based and MC QCD-multijet backgrounds.

110, and 150 $GeV/c^2$. The events are then detector simulated with DOGEANT's shower library package. The shower library method vastly increases the processing speed with which these events can be detector modeled. Prior to event reconstruction, noise is added into the event. Noise is random energy fluctuations in the calorimeter at a level of a few hundred MeV per module. Noise can be caused by an underlying event (proton/antiproton remnants), pile up events (preceeding event energy), multiple interactions per beam crossing, and calorimeter hardware noise. Noise is added to the events by overlaying one non-zero suppressed minimum bias event, where non-zero suppressed is defined as having all cells of the calorimeter read out, i.e. none of the cells have been zeroed before read-out. The minimum bias event requires a level zero trigger, and should properly model the calorimeter noise. The energy

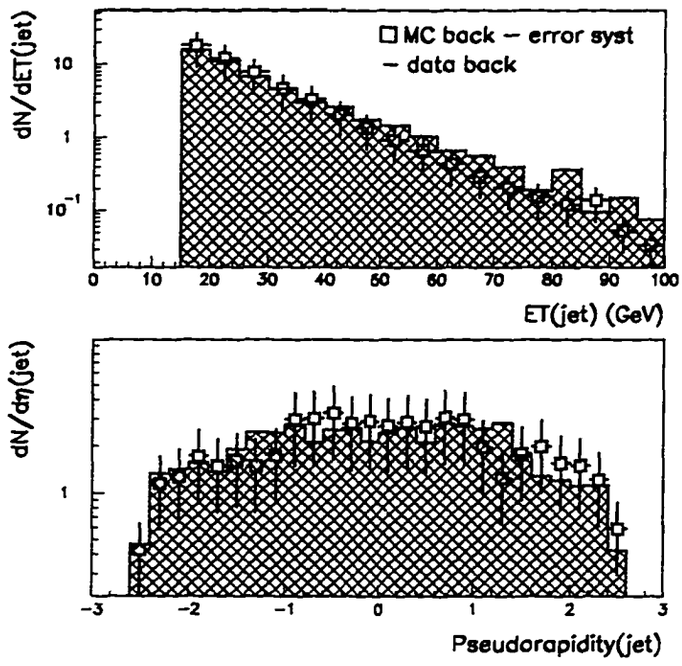


Figure 5.7 Comparing the jet kinematic variables of the calculated data-based and MC QCD-multijet backgrounds.

isolation variable(ISOL) is predominantly the sum of the detector transverse energy noise. Thus ISOL might be expected to be sensitive to additional calorimeter noise associated with higher instantaneous luminosities ($L_{inst}$). Clearly though, Figure 5.8 shows that the isolation energy fraction on electrons is only weakly dependant on $L_{inst}$ in $Z \rightarrow e^+e^-$ events, and will not be parameterized. The mean $L_{inst}$ of my data sample is about $6 \times 10^{30}$ $cm^{-2}s^{-1}$, the closest special minimum bias runs are $5.35 \times 10^{30}$ $cm^{-2}s^{-1}$which is sufficient. The ensembles are event reconstructed with DORECO version 12.15 and calorimeter energy corrected with CAFIX5.0.

To verify that the MC is modeling the Higgs events properly, $Z \rightarrow e^+e^-$ MC and data electromagnetic(EM) and hadronic quantities are compared. The EM quantities compared are EMF, ISOL, $\chi^2$, $E_T^e$, $\eta^e$, and $M_{ee}$. The hadronic variables compared

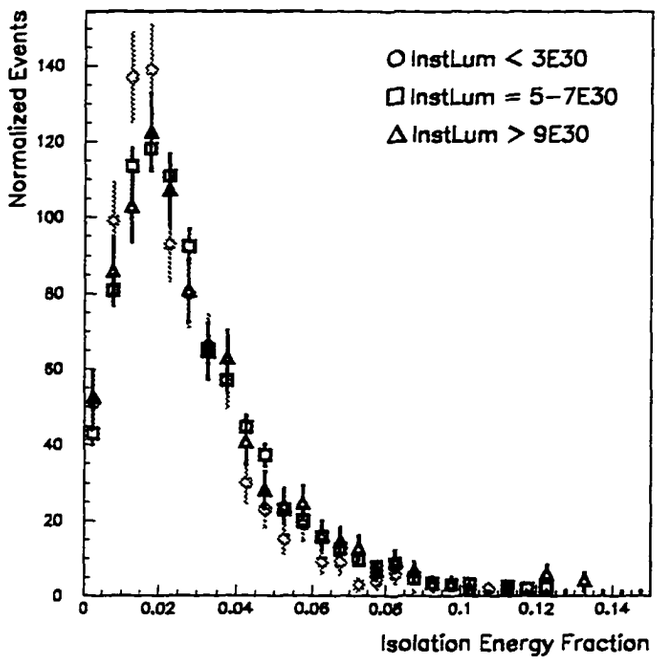


Figure 5.8 A $Z \rightarrow e^+e^-$ sample distribution of isolation energy fraction shows little dependence of Instantaneous Luminosity ($L_{inst}$).

are $E_T$, $\eta$, and the number of recoil jets.

A 5000 event ensemble of MC $Z \rightarrow e^+e^- + X$ events are generated as specified above. Here 'X' represents additional jets in the event.

The $Z \rightarrow e^+e^-$ data events are selected using the same trigger and EM quality selections as the signal sample. Further, no jet requirements are made, but the following requirements are made to Z-enrich the data's di-electron sample:

- $E_T^{em} \geq 20$ GeV,
- Reconstructed track for both EM objects.
- $86 GeV/c^2 \leq M_{ee} \leq 96 GeV/c^2$.

The data and MC Z boson events have the same EM kinematic and quality requirements and are shown in Figures [5.9, 5.10,5.11].

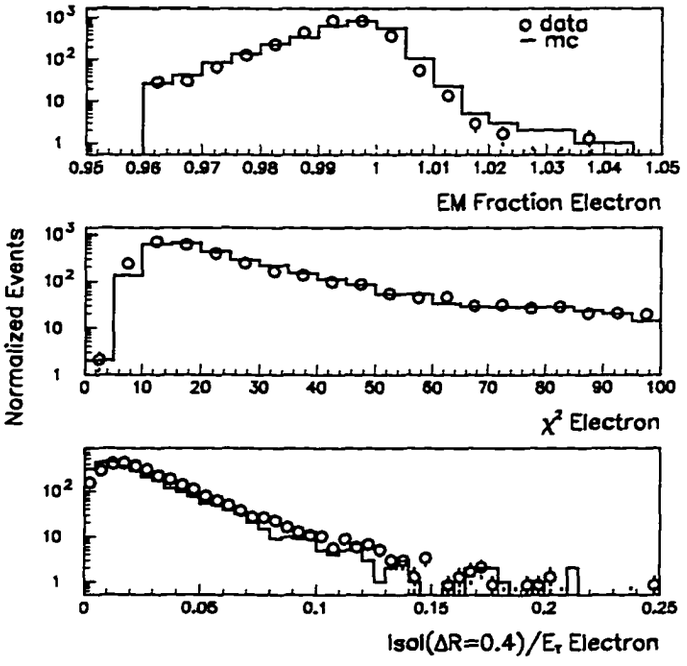


Figure 5.9 The EM quality variables agree very well between data and MC. The comparison is over all $\eta$.

The EM qualities agree nicely. The $M_{ee}$ distribution agree well on the condition that the MC Z boson mass is shifted up by 1.9 $GeV/c^2$. The MC EM energy scale is corrected for this by shifting the photon $E_T$ selection cuts downward by 2%. The data agree well with the experimental value for the $Z$ mass, therefore no $M_{\gamma\gamma}$ mass scaling is made on the final data sample. Also the true mass of my generated MC Higgs are known, therefore no correction is needed here either.

The Monte Carlo EM variable uncertainty is calculated using the same MC/data samples compared above. The uncertainty in the number of passing events is highly dependent on the agreement between MC/data near the event selection regions (i.e. $\chi^2 = 100$, EMF = 0.96, and ISOL = 0.10). The uncertainty is estimated by applying varying EM quality cuts to the Z samples, and comparing their differences. The

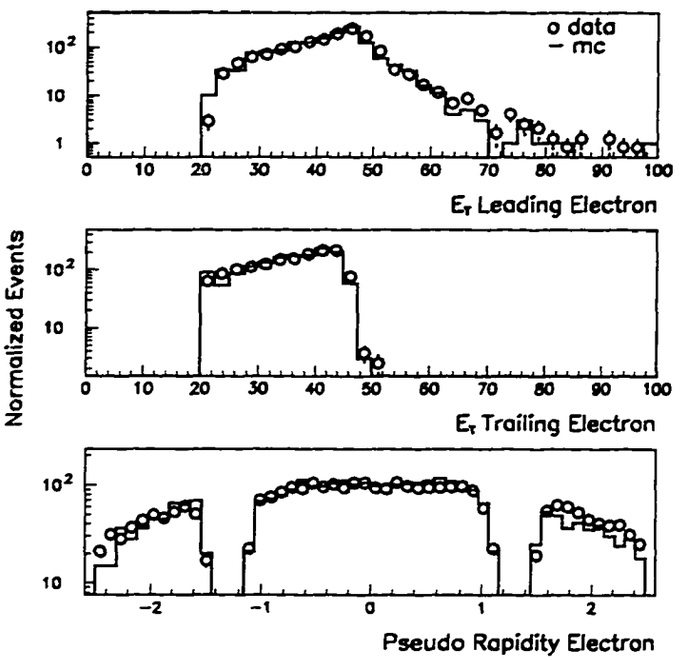


Figure 5.10 The EM kinematic variables agree very well between data and MC. The comparison is over all $\eta$.

difference between the data and MC is the uncertainty in the modeling of the EM variables. A "base" MC and data Z sample have the same kinematic requirements as before, but the electrons must pass the EM quality variables set at: EMF > 0.92; $\chi^2$ < 150; and ISOL < 0.15. The $Z \rightarrow e^+e^-$ data events are background subtracted using a side-band method. Five ensembles are constructed with varying EM quality requirements. Table 5.2 lists the EM requirements made for each ensemble and an efficiency variable $\zeta$ ($\zeta$=(ensemble A) /(base ensemble)) is calculated for each ensemble. Figure 5.12 shows the same information, and the $\zeta$ efficiency variable turn-on is seen for both MC and data. The MC $\zeta$ variable agrees with the data within statistical uncertainties. A 2% uncertainty is assigned to the MC EM quality variables. The MC modeling uncertainty for EM variables including kinematic

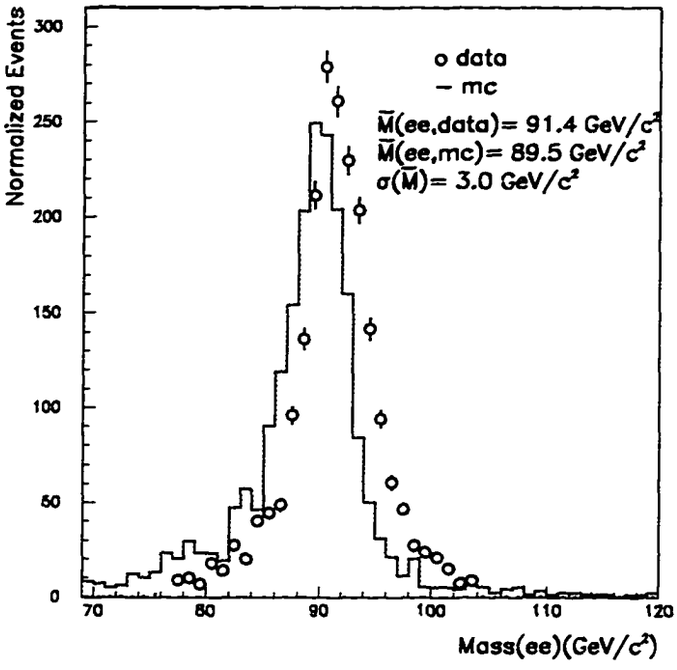


Figure 5.11 The two mass distributions are noticeably different. A gaussian fit to each of the samples gives a difference in the fitted masses of 1.9 $GeV/c^2$, a 2% effect (the MC EM energy scale is corrected for this). The resolutions of the two distributions differ by only 10%. The mean of the two ensembles widths are $\sigma(M_{ee}) = 3.0 \pm 0.3\ GeV/c^2$.

quantities is about 3% for the isolated photon cross section calculations [34], which is in nice agreement with what is calculated for this study.

The Z + jets events are used to study the hadronic quantities as well. Some data and MC hadronic quantities are compared in Figure 5.13, and are a reasonable match. The difference between the recoil jet $E_T$'s in the range of 50-70 GeV is a known data effect and is observed by the W/Z physics group as well [35]. The dominant source of uncertainty for the hadronic quantities is the jet energy scaling differences between data and MC. Using the same Z + jets events, an additional requirement is made that the Z boson's calculated $E_T$ be greater than 12 GeV. Due to the data

Table 5.2 The variable $\zeta$ is the efficiency for a Z event to pass the different EM quality variables. The MC and data $\zeta$ values agree within the statistical uncertainty. The MC EM variable uncertainty is estimated at 2%.

| (EMF,$\chi^2$,ISOL) | $\zeta$(data) | $\zeta$(MC) |
|---|---|---|
| (0.98,80,0.08) | 0.682±0.021 | 0.703±0.030 |
| (0.97,90,0.09) | 0.828±0.019 | 0.829±0.027 |
| (0.96,100,0.10) | 0.898±0.018 | 0.888±0.026 |
| (0.95,110,0.11) | 0.936±0.018 | 0.927±0.026 |
| (0.94,120,0.12) | 0.962±0.017 | 0.953±0.025 |

sample's construction, only jets with an $E_T$ greater than 12 GeV are kept: to avoid biasing the hadronic energy scale calculation, lower Z boson transverse energies are not included. The transverse momentum of the Z boson is calculated using the momentum vectors of the electrons. The recoil jet $E_T$ is calculated using every reconstructed jet in the event. The sum of all of the jets' vector $E_T$ are calculated using the jets' momentum vectors. This method is similar to the top physics group's jet energy scale uncertainty calculation [36]. Figure 5.14 and Figure 5.15 show the $E_T$(jets) vs $E_T$(Z boson) scatter and profile plots for the data and MC respectively. A linear regression fit (y=mx+b) on the profile plot is performed in the region of statistical significance only. By this I mean, that only a bin with 4 or more events is used for the linear fit. If the data and MC were energy corrected perfectly the linear regression fit would have a slope of 1 and an intercept of 0. The important factor here, though, is that the data and MC agree well with each other. Table 5.3 calculates the ratio of the slopes (PYTHIA/ data) and the difference in the intercepts (PYTHIA - data). The data and MC are fairly consistent within errors. The linear regression fit above 20 GeV will be used to avoid edge effects of the scatter plot (events can fluctuate above the 12 GeV Z boson $E_T$ cutoff, but not below). The edge effects would incorrectly decrease the slope and shift the intercept to larger values. The jet energy scale uncertainty is

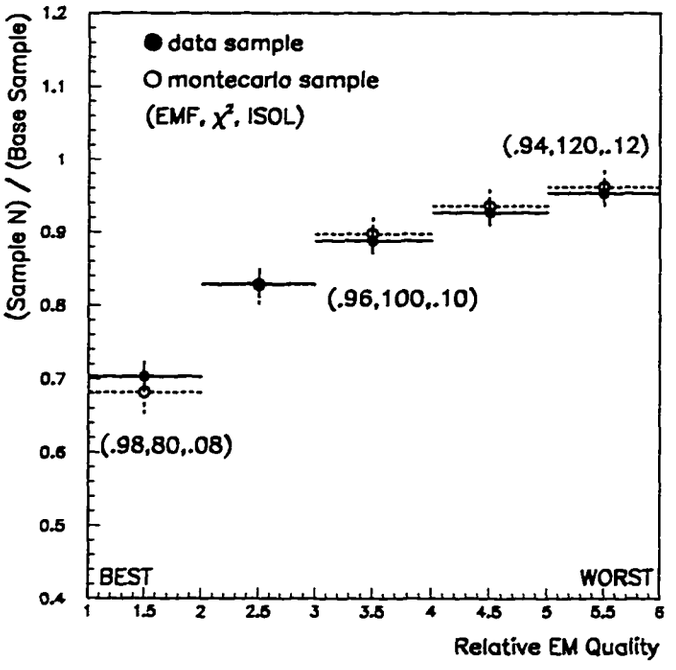


Figure 5.12 The vertical axis is the $\zeta$ efficiency variable. The horizontal axis scales from the tightest to loosest EM variable quality. The data and MC $\zeta$ values agree within the statistical uncertainty. The MC EM variable uncertainty is estimated at 2%.

set at $\pm(7\% + 1$ GeV). The top group has an uncertainty of $\pm(4\% + 1$ GeV) for a jet cone size of 0.5. The Monte Carlo Z boson variables model the Z boson data within the quoted errors. Therefore it is reasonable to conclude that the MC is modeling the Higgs signal sample properly in both the EM and hadronic variables as well.

Finally, I should note that DOGEANT does not model the central or forward drift chamber tracking efficiencies properly. The MC tracking efficiency is high by more than 20%, because DOGEANT and PYTHIA do not properly account for underlying event noise, aging effects, etc.. All the tracking efficiences must therefore be calculated using data. Much work has been done to calculate these efficiences [37, 38].

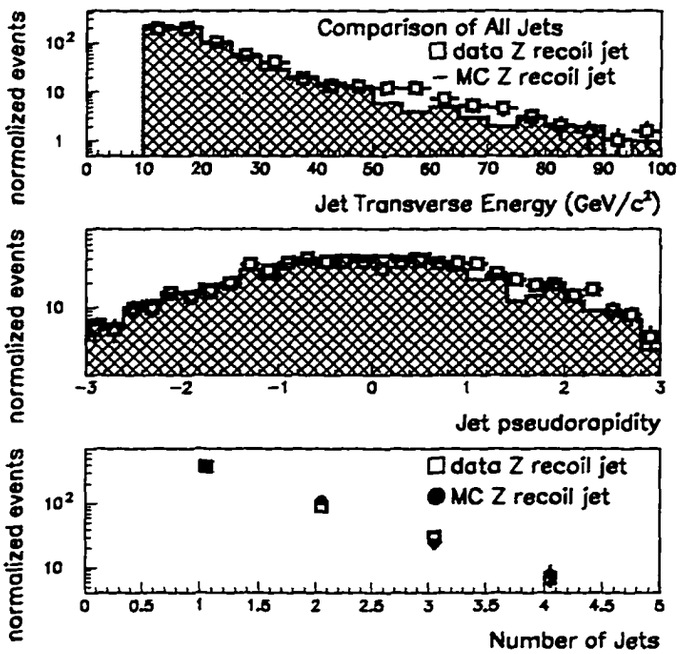


Figure 5.13 The hadronic quantities agree reasonably well. The error on the data is statistical. The statistical uncertainty of the MC sample is similar to the data sample.

The clean tracking road requirement efficiency is defined as,

$$\epsilon(ctr) = \epsilon_{oh}(1 - P_c(1 - (1/R_{h+t}))), \tag{5.4}$$

and since $R_{h+t} = (150 \pm 50)$,

$$(1 - (1/R_{h+t})) \rightarrow 1\ . \tag{5.5}$$

Table 5.3 The uncertainty in the jet energy scale is set at ±(7% + 1 GeV).

| $E_T$ Range | Slope (PYTHIA / data) | Offset(PYTHIA - data) |
|---|---|---|
| > 10 | 1.11±0.05 | -0.75±1.85 |
| > 20 | 1.06±0.07 | 0.73±3.62 |

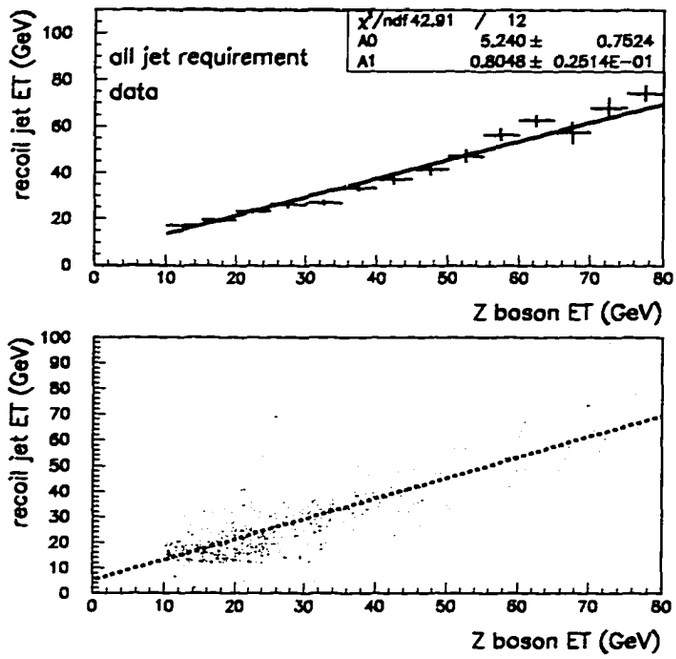


Figure 5.14 The first data distribution is the profile plot of the bottom scatter plot. A linear regression fit to the data is shown, and the function with uncertainties are stated in the upper right corner. The fit here is above 10 GeV.

So to a good approximation,

$$\epsilon(ctr) = \epsilon_{oh}(1 - P_c) \ . \tag{5.6}$$

Here $\epsilon_{oh}$ is the efficiency for requiring no reconstructed overlapping charged track and passing the HITSINFO cuts, $P_c$ is the photon conversion probability, and $R_{h+t}$ is the charged object rejection factor from applying HITSINFO and no track requirement as explained at the end of Chapter 4. The $\gamma \rightarrow e^+e^-$ conversion probabilities have been calculated using DOGEANT for the central(cc) and forward(ec) calorimeter regions. The conversion probability for the cc is $P_c(cc) = 0.10 \pm 0.01$ and for the ec is $P_c(\epsilon c) = 0.33 \pm 0.03$ [30, 39]. The systematic error is an assigned 10%; statistical error is negligible.

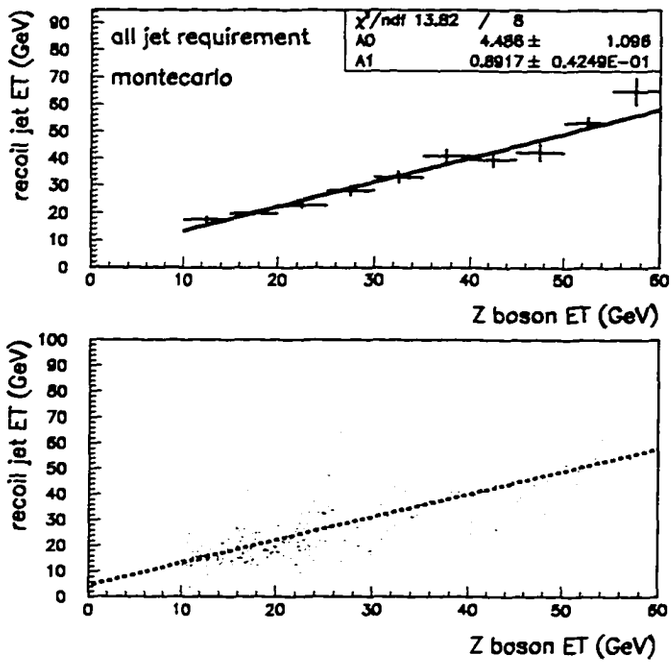


Figure 5.15 The first MC distribution is the profile plot of the bottom scatter plot. A linear regression fit to the data is shown, and the function with uncertainties are stated in the upper right corner. The fit here is above 10 GeV.

The charged track overlap plus HITSINFO failure probability are calculated using an "emulated photon" sample. An "emulated" photon is a purposely constructed imaginary photon in the calorimeter. The purpose of this is to correctly model the underlying event noise in the tracking volume of the photon. This method has been used extensively by other studies [30, 31, 40]. A sample of one thousand $Z \rightarrow e^+e^-$ events are DORECOed with version 12.22. The $Z$ electrons are selected from the Run I b data sample and must pass a loose set of criteria as stated below:

- vertex position within 75cm of $Z_{det} = 0$,
- $E_T^e \geq 15$ GeV,
- $\chi^2 \leq 150$.

- Energy Isolation Fraction $\leq 0.15$,
- $\mid \eta_e \mid \leq 1.1$ or $1.5 \leq \mid \eta_e \mid \leq 2.5$,
- EMF $\geq 0.95$,
- $75\text{GeV/c}^2 < M_{ee} < 105\ \text{GeV/c}^2$,
- $E_T^{jet} < 8$ GeV.

The selected electron and positron positions are $EM^1(\eta_1, \phi_1)$ and $EM^2(\eta_2, \phi_2)$. their bisector is calculated as:

$$\eta(\gamma_{emul}) = \frac{\eta_1 + \eta_2}{2} \tag{5.7}$$

and

$$\phi(\gamma_{emul}) = \frac{\phi_1 + \phi_2}{2}, \tag{5.8}$$

further requiring that the emulated photon is constructed in the smaller $\phi$ opening angle of the two parent electrons. The final requirement is made to avoid constructing an emulated photon on a recoil jet from the Z boson as shown in Figure 5.16. It is important not to bias the sample by constucting an emulated photon on top of underlying hadronic activity, since these photons would most likely fail EM quality requirements regardless. Therefore to avoid double counting this inefficiency the emulated photon is constructed away from the recoil jet region and the emulated photon must pass energy isolation requirements similar to my final photon sample. The efficiency of the hits requirements and no track overlap requirement for the central calorimeter is:

$$\epsilon(cc)_{oh} = 0.81 \pm 0.03 \pm 0.03(stat/syst)$$

and for the forward calorimeter,

$$\epsilon(ec)_{oh} = 0.72 \pm 0.06 \pm 0.02\ .$$

The statistical error is calculated using the binomial theorem. The systematic error is calculated by removing the emulated photon isolation requirements(i.e. recoil jet

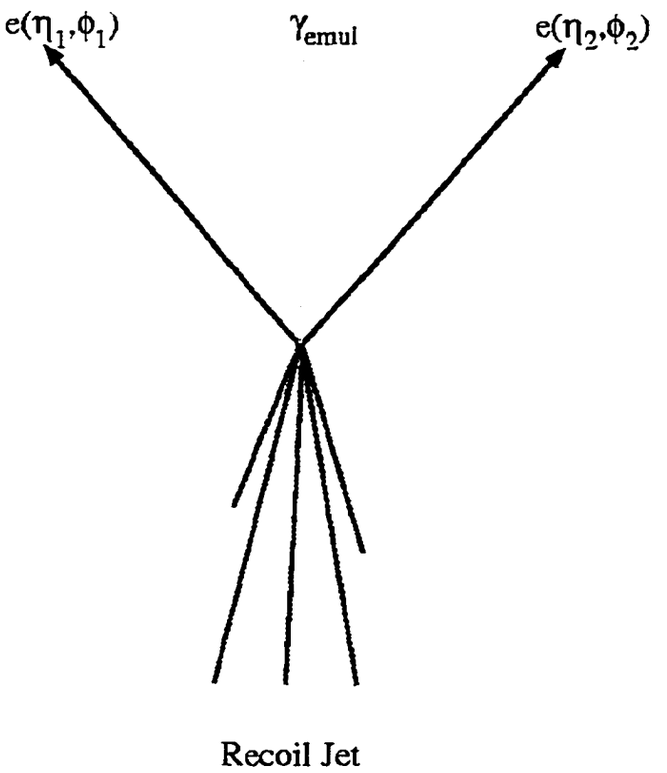


Figure 5.16 The emulated photon is constructed at the bisector of the two electrons. This method differs from other studies, but the results are consistent within errors.

$E_T$ req., energy isolation of $\gamma_{emul}$, etc.). The difference is minimal, and the systematic error is quoted as one half the difference between the two requirements. Other similar studies have been carried out [30], and the efficiencies are consistent within the quoted errors.

All of the quantities are in hand, therefore the efficiency for requiring a clean tracking road in the central calorimeter is:

$$\epsilon(ctr) = \epsilon_{oh}(1 - P_c).$$

$$\epsilon(ctr, cc) = 0.73 \pm 0.03 \pm 0.03$$

and for the forward calorimeter,

$$\epsilon(ctr, cc) = 0.48 \pm 0.04 \pm 0.01 \ .$$

The $\epsilon$(ctr) errors are simply the $\epsilon_{oh}$ and $P_c$ errors added in quadrature. The numbers are reasonable, the forward regions are less efficient as expected, mainly due to the higher $\gamma \rightarrow e^+e^-$ conversion probability and charged track overlap probability.

## Signal Optimization

Bosonic Higgs mass sensitivity is expected around 80-90 GeV/$c^2$, therefore the event selection criteria will be optimized using the 80 GeV/$c^2$ Higgs MC sample and the data-based QCD multijet background sample. Noticeable differences in photon(jet) transverse energy and pseudorapidity distributions are seen. Normalized transverse energy and pseudorapidity distributions are shown in Figure 5.17, 5.18, 5.19.

The optimized event requirements are chosen using the following significance parameter:

$$Significance = \frac{N_{signal}}{\sqrt{N_{background} + N_{signal}}} \ .$$

Here $N_{signal}$ is the number of Higgs events and $N_{background}$ is the number of QCD background events in the ensemble. A significance plot of the additional transverse energy cut is shown in Figure 5.20 and we cut at $E_T > 30$ GeV. An event requirement that the leading photon and the leading jet have an $|\eta| \leq 2$ (Fig. 5.21) is applied. Here "leading" refers to the higher transverse energy photon(jet) in the event. Finally, a looser cut of $\eta < 2.25$ on the trailing jet and photon in the event is applied. The $E_T$ and $\eta$ event requirements are reasonable since the Higgs events are more centrally located due to the decay of two massive objects, the W/Z and H bosons.

The additional event requirements are:

- $\not{E}_{T1} \geq 30$ GeV,

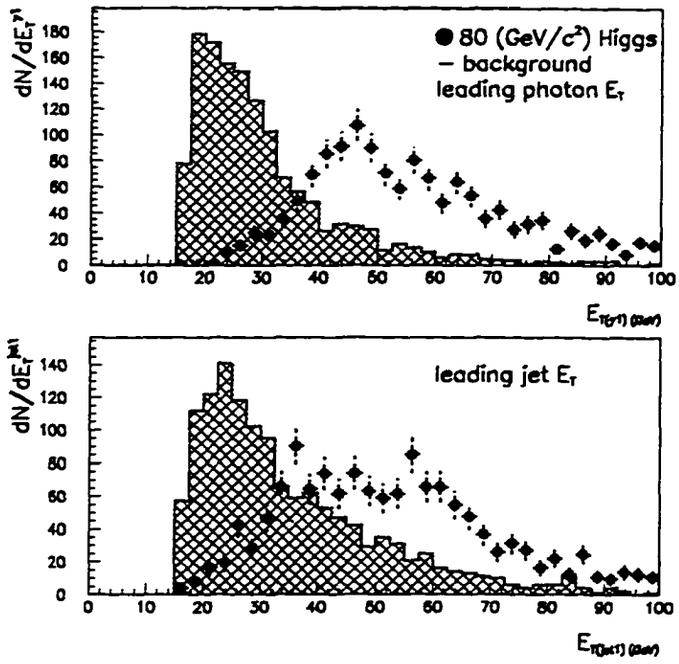


Figure 5.17 Leading photon and jet transverse energies. Significant differences between the background and Higgs signal.

- $E_{T1}^{jet} \geq 30$ GeV.
- $\eta_1^{\gamma} \leq 2.0$.
- $\eta_1^{jet} \leq 2.0$.
- $\eta_2^{\gamma} \leq 2.25$.
- $\eta_2^{jet} \leq 2.25$.
- 40 GeV/c$^2$ < $M_{\gamma\gamma}$ < 150GeV/c$^2$ .

The final event requirements reduces the QCD background by 85% while only eroding the signal efficiency by 15%. The 95% confidence level upper limit cross section is decreased by a factor of 3. due to the reduced QCD background. The final event sample consists of four events with no events above the present mass limit of 60 GeV/c$^2$ as seen in Figure 5.22 and Figure 5.23 with an expected $7.8 \pm 3.4$ events of

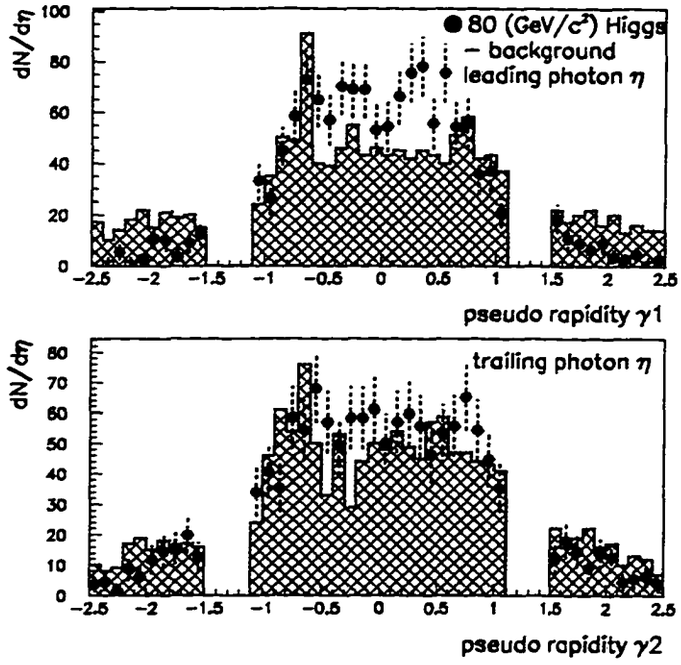


Figure 5.18 Leading and trailing photon pseudo rapidities. Significant differences between the background and Higgs signal at larger absolute $\eta$'s.

background using MC methods and $6.0 \pm 1.8$ events of background using data-based methods.

## Signal Efficiency and Limit Calculation

The final event requirements are applied to the seven MC Higgs samples, except the tracking requirements. Since DOGEANT incorrectly models the central tracking of the DØ detector. Instead of making the same clean tracking road requirements as on the data, we calculated the efficiency for making such a cut. Therefore each photon in each event is weighted with $\epsilon_{ctr}$ to account for the tracking cuts. A diphoton invariant mass is calculated, each photon is weighted by $\epsilon_{ctr}$, and mass binned for every

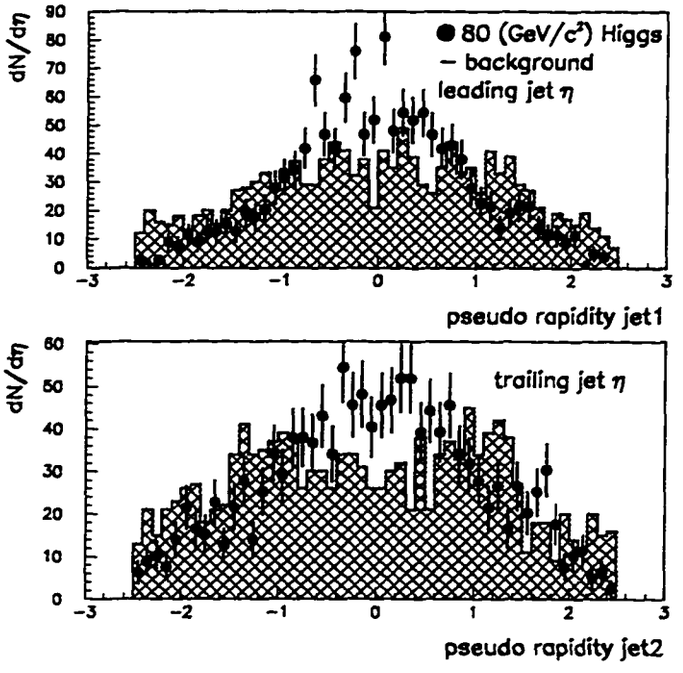


Figure 5.19 Leading and trailing jet pseudo rapidities. Significant differences between the background and Higgs signal at larger absolute eta's.

event that passes. The signal acceptance for each Higgs-mass sample is calculated by making a gaussian fit to the final diphoton invariant mass distribution. All of the fitted samples are shown in Appendix D. The fit gets progressively worse for larger Higgs masses, due to the increasingly longer tail on the lower $M_{\gamma\gamma}$ side of the resonance. but for all the Higgs samples the gaussian fit has a $\chi^2 < 1.5$ per degree of freedom. The lower mass-tail is due to the energy loss in the calorimeter cracks. To avoid loosing some signal efficiency, the number of events are integrated over a $[-4\sigma \rightarrow +2\sigma]$ ($M_{\gamma\gamma}$) window centered at the generated mass. The number of events that pass are then simply divided by the number of events generated for each ensemble (5000 events for each ensemble) to yield the signal efficiency and acceptance (Table 5.4).

The signal efficiency has four dominant sources of error: tracking requirement

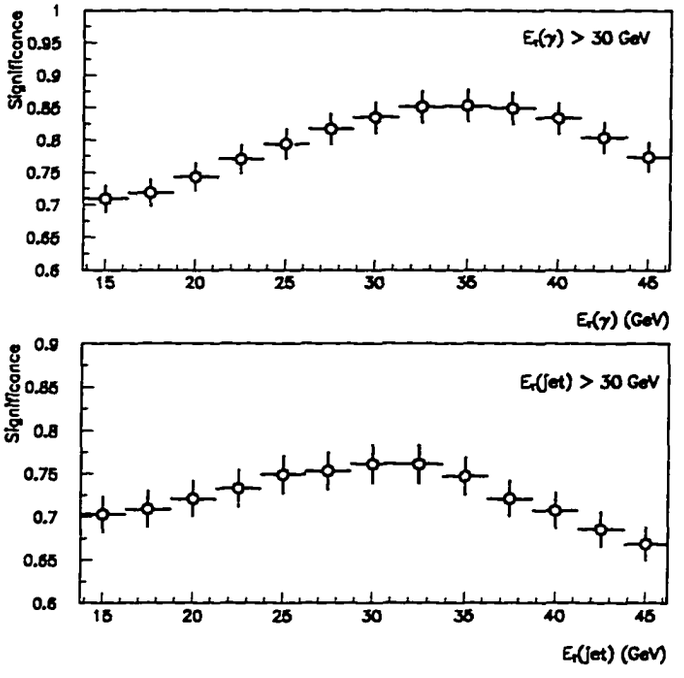


Figure 5.20 The transverse energy significance distributions. A modest transverse energy cut of 30 GeV is applied. The error is statistical only.

uncertainty of 6.1%, the uncertainty in the MC modeling of the hadronic variables which varies from 7-11%, the uncertainty in the MC modeling of the electromagnetic variables of 2%, and the statistical error on the MC sample which is of the order of 5%. The errors are largely uncorrelated, so they are added in quadrature and give a mean error of about 12.5%.

A preliminary 90% and 95% confidence level cross section limit vs $M_{\gamma\gamma}$ is shown in Figure 5.24 and was calculated using a Bayesian approach [5]. Appendix C gives a brief overview of the Bayesian theory/method. The limit incorporates the error associated with the efficiency, luminosity, and background expectation. Correlated error is not included in the fitter. The limits are tabulated in Table 5.5

The full bosonic Higgs cross section is plotted in Figure 5.5 with the cross section

Table 5.4 The $\gamma\gamma$jj signal efficiency and acceptance for the diphoton mass range of 60 to 150 GeV/$c^2$.

| $M_{Higgs}$ | $\sigma(M_{\gamma\gamma})$ | $N_{pass}$ | Eff + Acc |
|---|---|---|---|
| 60(GeV/$c^2$) | 2.2 (GeV/$c^2$) | 271.2(events) | $5.4 \pm 0.6$(%) |
| 70 | 2.3 | 328.1 | $6.7 \pm 0.9$ |
| 80 | 2.5 | 372.2 | $7.4 \pm 0.9$ |
| 90 | 2.8 | 409.9 | $8.3 \pm 0.9$ |
| 100 | 2.9 | 429.6 | $8.7 \pm 1.0$ |
| 110 | 3.3 | 452.8 | $9.1 \pm 0.9$ |
| 150 | 3.9 | 485.4 | $10.0 \pm 1.2$ |

Table 5.5 The $\gamma\gamma$jj limit is calculated using a Bayesian approach.

| $M_{Higgs}$ | $N_{back}$ | $N_{obs}$ | $\sigma$ [90(95)%C.L.] |
|---|---|---|---|
| 60(GeV/$c^2$) | $0.9 \pm 0.3$ | 2 | 0.88(1.06)(pb) |
| 70 | $0.7 \pm 0.3$ | 0 | 0.36(0.46) |
| 80 | $0.6 \pm 0.2$ | 0 | 0.34(0.44) |
| 90 | $0.4 \pm 0.1$ | 0 | 0.29(0.37) |
| 100 | $0.4 \pm 0.1$ | 0 | 0.27(0.35) |
| 110 | $0.2 \pm 0.1$ | 0 | 0.27(0.34) |
| 150 | $0.1 \pm 0.1$ | 0 | 0.24(0.32) |

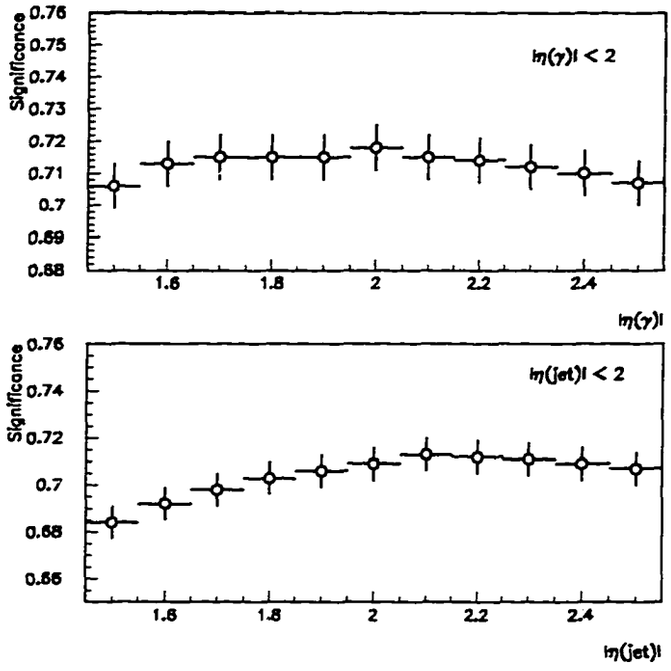


Figure 5.21 The leading jet and photon $\eta$ significance distributions. A modest $|\eta| < 2$ cut is applied. The error is statistical only.

limit contour, and includes both the HW/HZ associated production and the vector boson fusion Higgs production. The cross sections and branching fractions are calculated using PYTHIA 5.7 and are corrected using the recommendations from reference [3]. A 90(95)% confidence level bosonic Higgs lower mass limit of 85(90) GeV/$c^2$ is set.

## Summary

A search for new physics in the channel $p\bar{p} \rightarrow \gamma\gamma jj$ has been completed. Zero events are seen with a mass greater than the LEP lower mass limit of 60 GeV/$c^2$. Four events are seen in the entire ensemble while $7.8 \pm 3.4$ events of background are expected using MC methods and $6.0 \pm 1.8$ events of background are expected using data-based

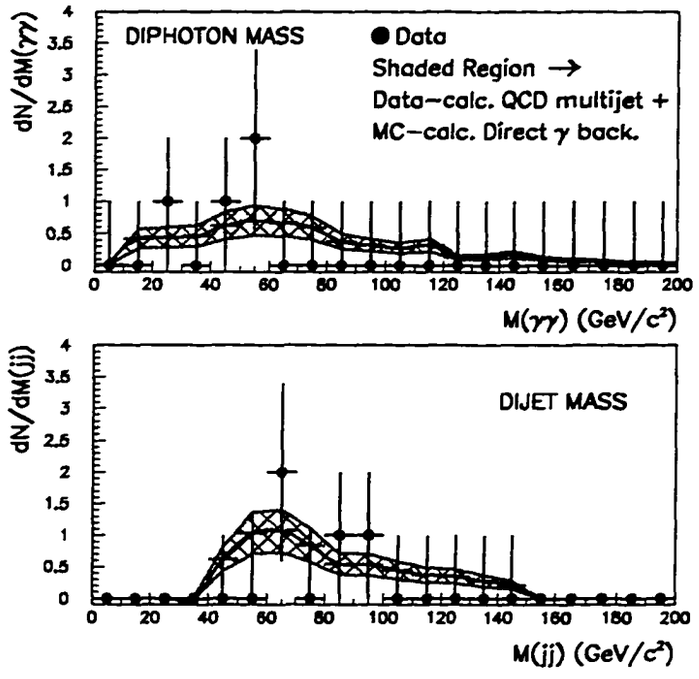


Figure 5.22 The signal sample with the final event requirements. The data-based QCD, MC DDP, and MC SDP backgrounds are shown as the shaded region. The error on the background is systematic, and on the data sample is statistical.

methods. A 90(95)% C.L. bosonic Higgs lower mass limit of 90(85) GeV/$c^2$ is set, using standard model coupling strengths between the Higgs and the vector bosons. A general 90(95)% C.L. upper limit production cross section is calculated which ranges from 0.60(0.73) pb$^{-1}$ for $M_{\gamma\gamma}$ = 65GeV/$c^2$ to 0.24(0.32) pb$^{-1}$ for $M_{\gamma\gamma}$ = 150GeV/$c^2$.

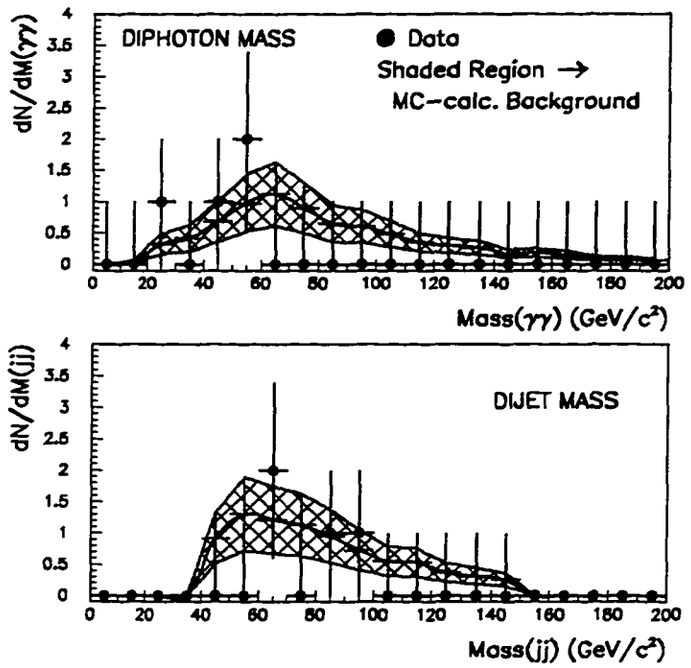


Figure 5.23 The signal sample with the final event requirements. The MC QCD, DDP, and SDP backgrounds are shown as the shaded region. The error on the MC is systematic, and on the data sample is statistical.

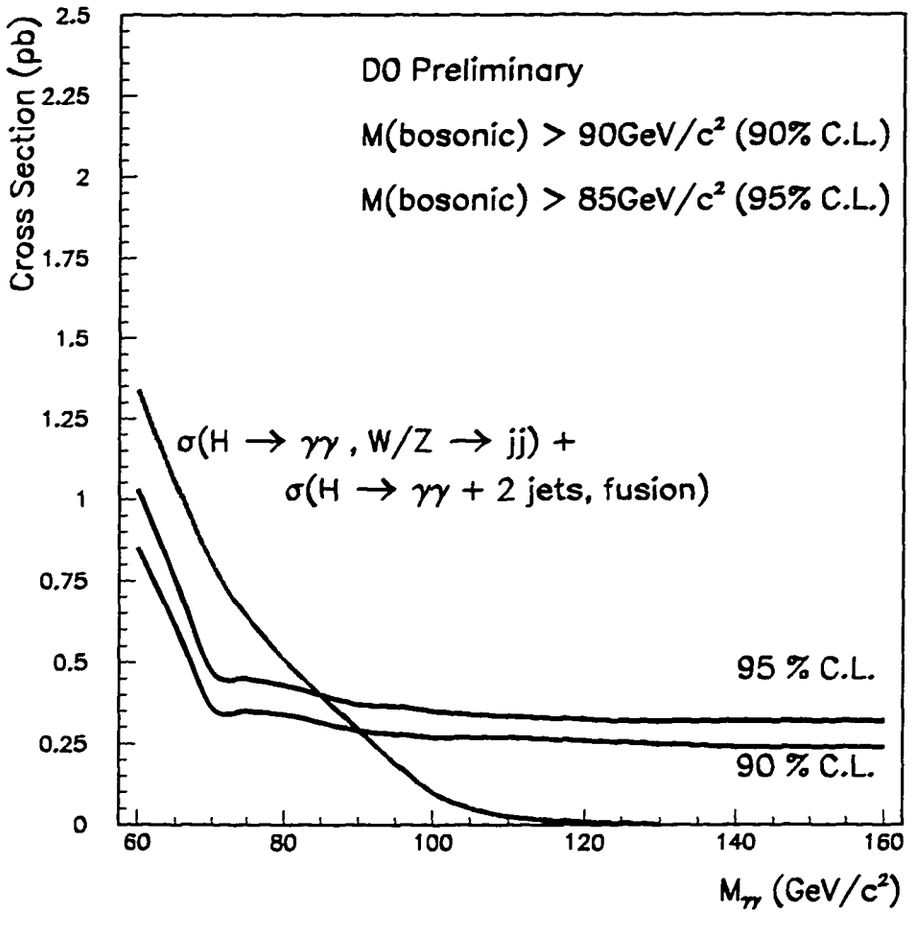


Figure 5.24 The 90% and 95% C.L. lower mass limit of 90 $GeV/c^2$ and 85 $GeV/c^2$ respectively is set for the bosonic Higgs.

# APPENDIX A INTERESTING EVENTS WITH A DIPHOTON MASS OF ABOUT 155 GEV/c$^2$

For the general event requirements, an interesting event fluctuation at 155 $GeV/c^2$ occurs. Four events are seen in a mass window of 150-160 $GeV/c^2$, with an expected $1.0 \pm 0.3$ events of background. The Poisson probability is defined as:

$$P(N_o) = \frac{N_e^{N_o} e^{-N_e}}{N_o!},$$

where $N_e$ is the number of expected events and $N_o$ is the number of observed events. The probability for four events to be observed with one expected is:

$$P(4) \simeq \frac{1^{-4} \cdot e^{-1}}{4!} \simeq 0.0153 .$$

That is a 2.5 sigma effect! The probability for such a fluctuation anywhere in the range 60-200 $GeV/c^2$ is ~3%, still interesting! So are these events consistent with a 'Higgs-like' decay, or simply a QCD fluctuation?

The event topologies are studied and show evidence that these events seem consistent with QCD background. Looking at Figure A.1, the leading and trailing photon transverse energies are much lower than expected for a 150 $GeV/c^2$ Higgs. Also notice that the photons are widely separated in $\eta$; this is not consistent with a 150 $GeV/c^2$ Higgs either. The 4 events are quite consistent with QCD background though, which is the probable source of these events. Further, larger values of $\mid \eta_\gamma^1 - \eta_\gamma^2 \mid$ give larger diphoton invariant masses, which explains the higher masses seen here. A 'real' high mass object decay is more central, thus has a small $\mid \eta_\gamma^1 - \eta_\gamma^2 \mid$ value. The jet $E_T$

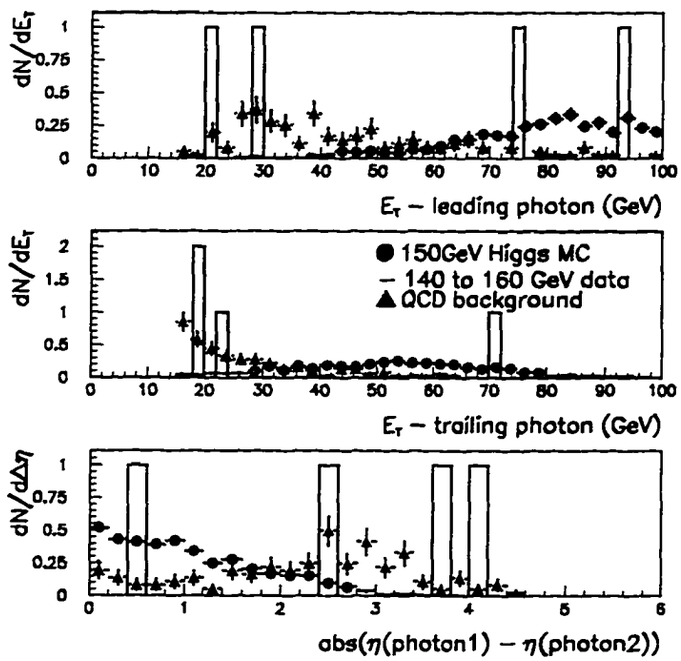


Figure A.1 The four events with $150 \leq M_{\gamma\gamma} \leq 160 GeV/c^2$ are plotted with a normalized 150 $GeV/c^2$ MC Higgs sample and a QCD background sample. The bosonic Higgs MC events are scaled up by 1000 from the expected number of events.

spectra are not as distinct as the photon's, but one could say that the 4 event's jets are slightly more consistent with QCD multijet events (Fig. A.2). The diphoton and dijet invariant mass distributions for the the 4 events are compared with the 150 $GeV/c^2$ Higgs MC sample. The 150 $GeV/c^2$ Higgs diphoton mass spectra are scaled up by 5 $GeV/c^2$, so that a better comparison can be made as seen in Figure A.3). The photon's and jet's spectrum is consistent with the QCD background and it is reasonable to conclude that the 4 events are more consistent with QCD multijet events than with new physics.

The four events run and event numbers are:

- 77324, 7864

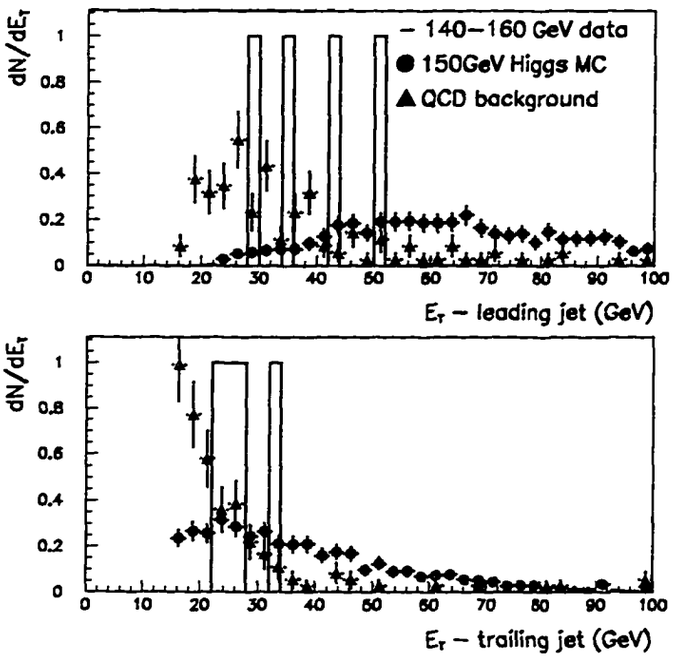


Figure A.2 The four events with $150 \leq M_{\gamma\gamma} \leq 160 GEV/c^2$ are compared with a 150 $GeV/c^2$ Higgs sample and a QCD background sample.

- 86556, 7529
- 92112, 23613
- 95831, 53644.

Two seperate event display figures are shown for each event. The first is a calorimeter energy "lego" plot, which displays the calorimeter as it would appear if we cut down a PHI plane and peeled the detector open. Therefore, we have two axes which are PHI and ETA, and a third dimension upward which is energy. The lego-plot is nice for observing shower size, energy, profile, and much more. The second plot shown is a side view of the calorimeter with all the energy and tracking hits summed over all PHI. Be careful about showers overlapping here, since showers at similar ETA's

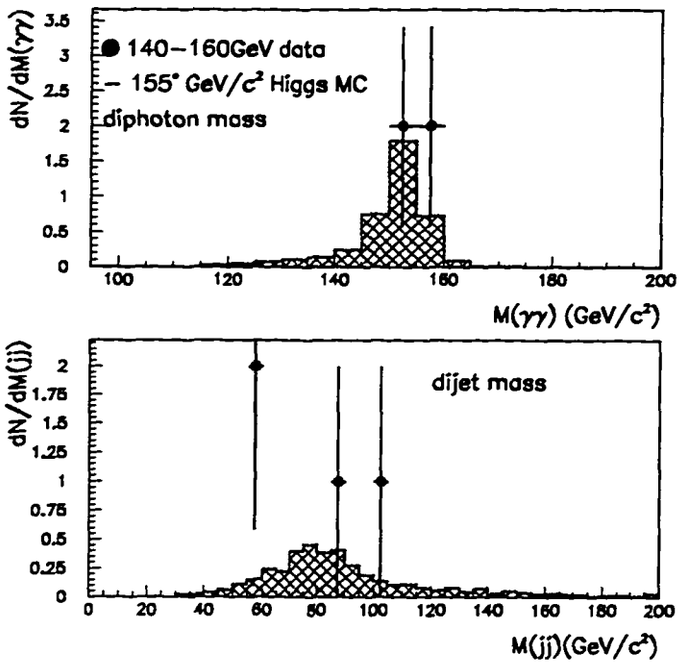


Figure A.3 The four events with $150 \leq M_{\gamma\gamma} \leq 160 GEV/c^2$ are compared with the 150 $GeV/c^2$ Higgs sample. The 150 $GeV/c^2$ Higgs diphoton mass spectrum is scaled up by 5 $GeV/c^2$, and the bosonic Higgs MC events are scaled up by 1000 from the expected number of events, so that a better mass comparison can be made.

but different PHI's will be plotted on top of each other. This plot shows where the reconstructed vertex was found, and clearly shows if the shower is in the forward or central calorimeter.

Figure A.4 and Figure A.5 displays event (77324, 7864).

Figure A.6 and Figure A.7 displays event (86556, 7529).

Figure A.8 and Figure A.9 displays event (92112, 23613).

Figure A.10 and Figure A.11 displays event (95831, 53644).

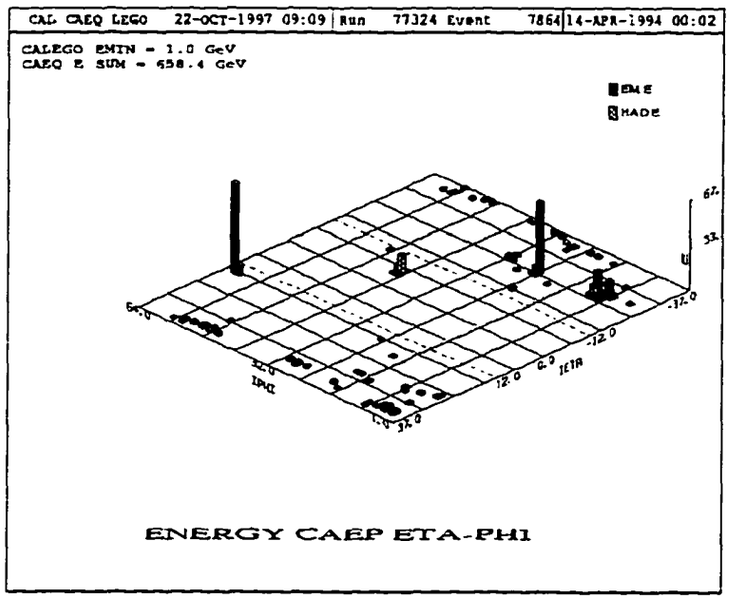


Figure A.4 The lego-plot for event 77324 run 7864.

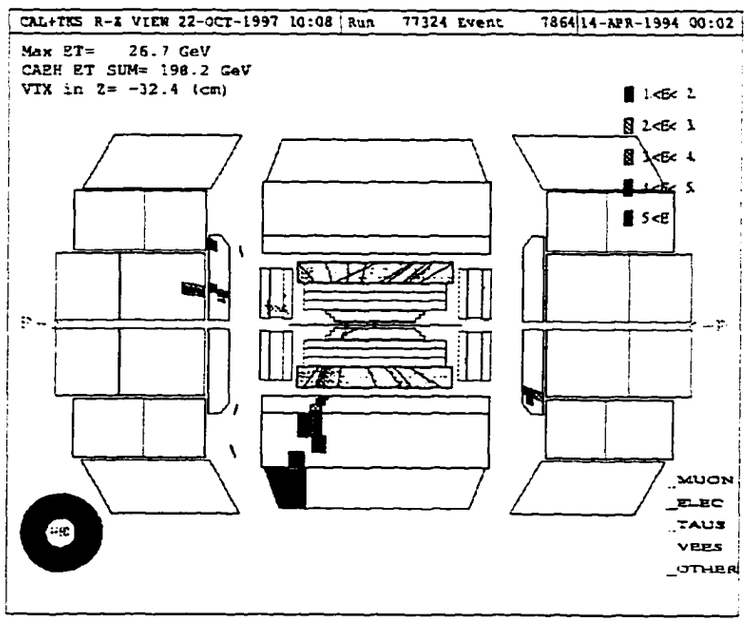


Figure A.5 The side view of the calorimeter and tracking for event 77324 run 7864.

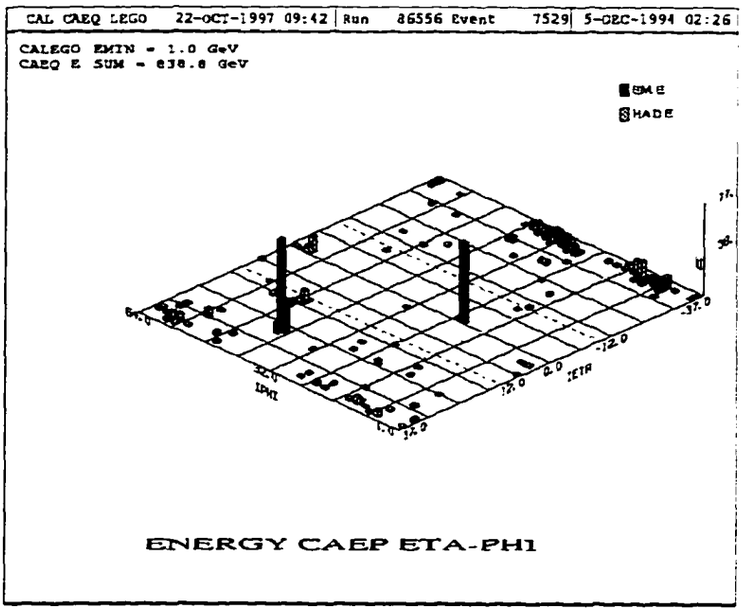


Figure A.6 The lego-plot for event 86556 run 7529.

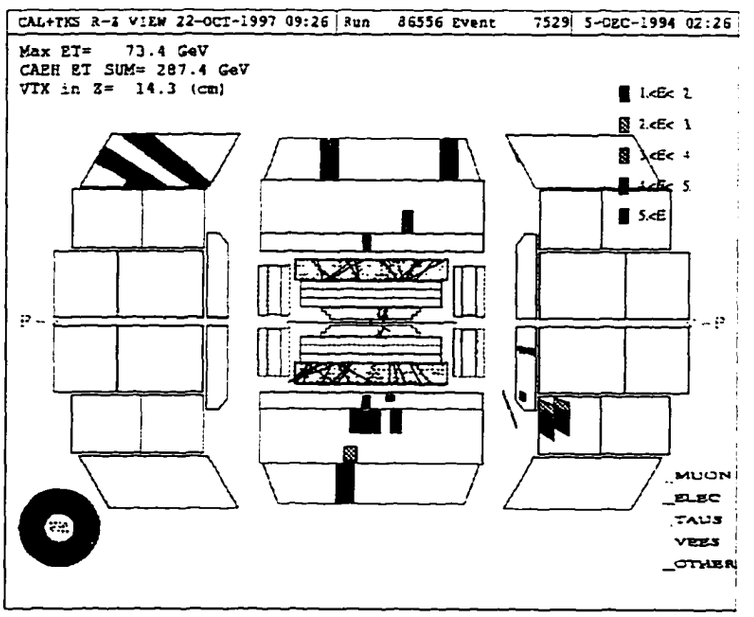


Figure A.7 The side view of the calorimeter and tracking for event 86556 run 7529.

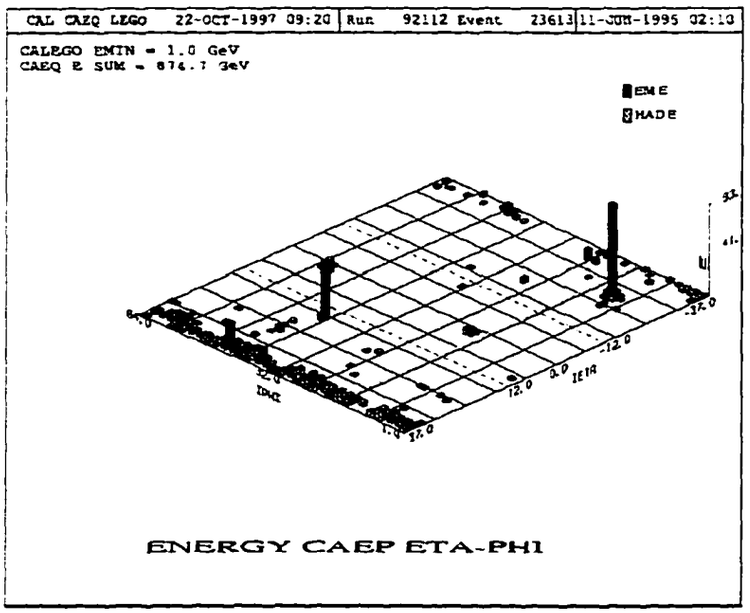


Figure A.8 The lego-plot for event 92112 run 23613.

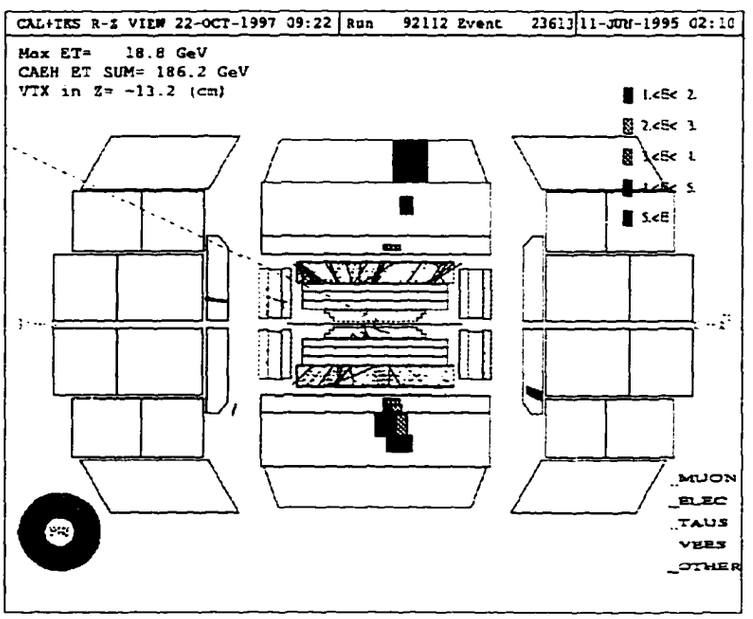


Figure A.9 The side view of the calorimeter and tracking for event 92112 run 23613.

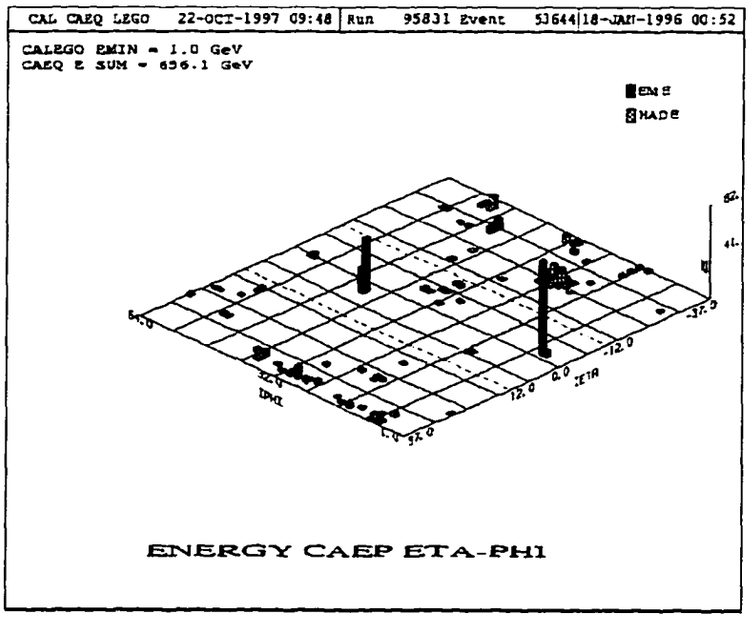


Figure A.10 The lego-plot for event 95831 run 53644.

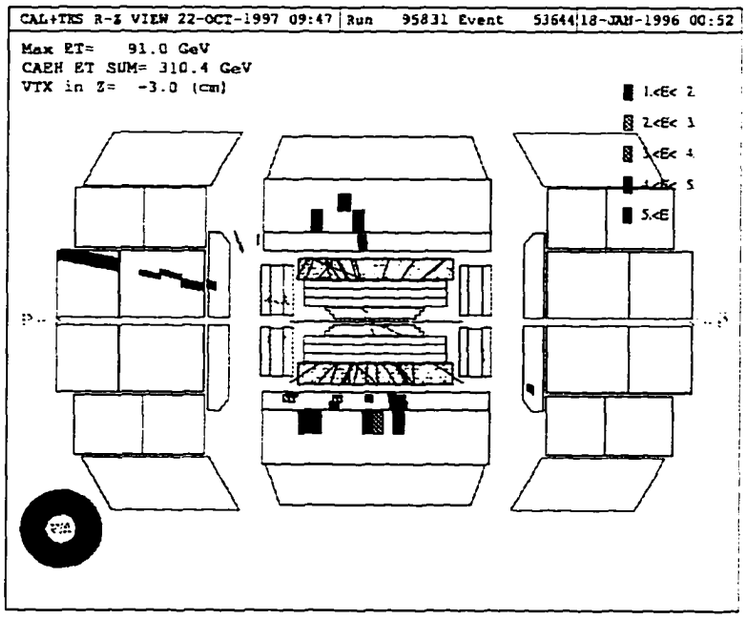


Figure A.11 The side view of the calorimeter and tracking for event 95831 run 53644.

# APPENDIX B THE PROBABILITY FOR A JET TO FRAGMENT INTO AN ISOLATED PHOTON

## Abstract

I present a study of the probability for a jet to fragment into an isolated photon in the DØ detector, (P(jet $\rightarrow$ "$\gamma$")). Assuming that all isolated photons arise from two sources, jets and direct photons. The data used to calculate P(jet $\rightarrow$ "$\gamma$") are run 1a's Inclusive Jet Cross Section [41],Inclusive Isolated Direct Photon Cross Section [38]. and the direct photon purity [38][42]. The P(jet $\rightarrow$ "$\gamma$")'s transverse energy range is from 40GeV to 125GeV and is within two regions of pseudorapidity $\eta$ : $\mid \eta \mid < 0.9$ and $1.6 < \mid \eta \mid < 2.5$. The probabilities calculated are of the order $10^{-4}$ which are consistent with previous studies [33][43]. The $E_T$ dependence differs for this study. though, since the photon energy isolation requirement is a flat 2 GeV for reference [38], and a floating 10%$\times$ $E_T^{\gamma}$ requirement is used for reference [33, 43].

## Isolated Photon Overview

The dominant production mechanism of isolated low $E_T$ photons at DØ are from gluon Compton scattering(LO) and Bremsstrahlung photons from initial and final state quarks(NLO), before hadronization occurs. These are called "direct" photon processes. The problems with making an accurate measurement of the direct photon cross section stem from the large non-direct photon background. The dominant

background is due to the quark's hadronization process which can produce high $P_t$ $\pi^0$ or $\eta$ mesons that carry most of the jet energy away. Much of this background is excluded due to restrictive isolation and quality requirements on the photon:

- $E_T(\Delta R = .4) - E_T(\Delta R = .2) \mid < 2GeV$,
- EMF$\geq$ .96,
- $\chi^2 < 150$ for CC and EC,
- vertex position within 50cm from $Z_{det} = 0$,
- no tracks between calorimeter cluster and primary vertex,
- fiducial cuts applied to photons near calorimeter boundaries.

Where EMF is the percentage of energy deposited by the electromagnetic shower in the electromagnetic section of the calorimeter. But the inclusive jet cross section is so much larger than the direct photon's cross section($10^5$), that this background is still a serious effect.

This remaining background is quantified by the purity of the direct photon sample. where purity is defined as the fraction of photon candidates which are genuine single isolated photons. Physically, $\pi^0$ and $\eta$ mesons decay into two or more photons. Thus. they will convert into $e^+e^-$ pairs roughly twice as often as direct photons in first layer of the electromagnetic calorimeter(EM1). So by using the fraction of energy deposited in EM1 as a discriminator, the purity can be estimated. Using the previous idea and incorporating this into a detailed GEANT detector simulation and further varification with W$\rightarrow e\nu$ data, a purity plot was calculated for the central($\mid \eta \mid < 0.9$) and forward($1.6 < \mid \eta \mid < 2.5$) regions of the detector. One note, all "pure" photons at this point are assumed to be from a direct photon process, and all "non-pure" photons are from a jet fragmentation fluctuation that produced an isolated photon. With the purity calculated the Isolated Direct Photon Cross Section is known.

## Calculation of P(jet $\rightarrow$ "$\gamma$")

Let $\psi$ be the purity, that is, the fraction of the "isolated photon" sample produced by a direct photon process. Since we assume photons arise from two sources, jets and direct photons, the total "isolated photon" cross section is:

$$\left\{\frac{d^2\sigma}{dE_t d\eta}\right\}_{isolated\ \gamma} = \left\{\frac{d^2\sigma}{dE_t d\eta}\right\}_{jet\rightarrow"\gamma"} + \left\{\frac{d^2\sigma}{dE_t d\eta}\right\}_{direct\gamma}$$

and a fraction $\psi$ of this total is the true direct $\gamma$ cross section,

$$\left\{\frac{d^2\sigma}{dE_t d\eta}\right\}_{direct\gamma} = \psi\left[\left\{\frac{d^2\sigma}{dE_t d\eta}\right\}_{jet\rightarrow"\gamma"} + \left\{\frac{d^2\sigma}{dE_t d\eta}\right\}_{direct\gamma}\right]$$

so that

$$\left\{\frac{d^2\sigma}{dE_t d\eta}\right\}_{jet\rightarrow"\gamma"} = \frac{1-\psi}{\psi}\left\{\frac{d^2\sigma}{dE_t d\eta}\right\}_{direct\gamma}.$$

The fraction $\frac{1-\psi}{\psi}$ is shown in Figure B.1. The jet $\rightarrow$ "$\gamma$" cross section is shown for the forward and central detector regions in Figure B.2. Notice that the forward jet $\rightarrow$ "$\gamma$" cross section is similar in value to the central region's at the lower $E_T$ values. This is due to the isolation cut being $E_T$ dependant, therefor being less effective at purifying the forward region's photons. The "Inclusive Jet Cross Section" is used as the production rate for multijets, obviously. Note that the Inclusive Jet Cross Section covers a slightly different rapidity region than the jet $\rightarrow$ "$\gamma$" (Fig. B.2). This difference is not serious though, since the cross sections are calculated per unit $\eta$ and per unit $E_T$. The effect of this is small($< 1\%$) and is far out-weighed by other systematic uncertainties. The P(jet $\rightarrow$ "$\gamma$") will be stated as covering the same rapidity region as the referenced Isolated Photon Cross Section publication.

Calculating the probability for a jet to fake as an isolated photon P(jet $\rightarrow$ "$\gamma$") is just the ratio of $\{\frac{d^2\sigma}{dE_t d\eta}\}_{jet\rightarrow"\gamma"}$ to $\{\frac{d^2\sigma}{dE_t d\eta}\}_{inclusivejet}$ as seen in Figure B.3.

$$P(jet \rightarrow "\gamma") = \frac{\{\frac{d^2\sigma}{dE_t d\eta}\}_{jet\rightarrow"\gamma"}}{\{\frac{d^2\sigma}{dE_t d\eta}\}_{inclusivejet}}$$

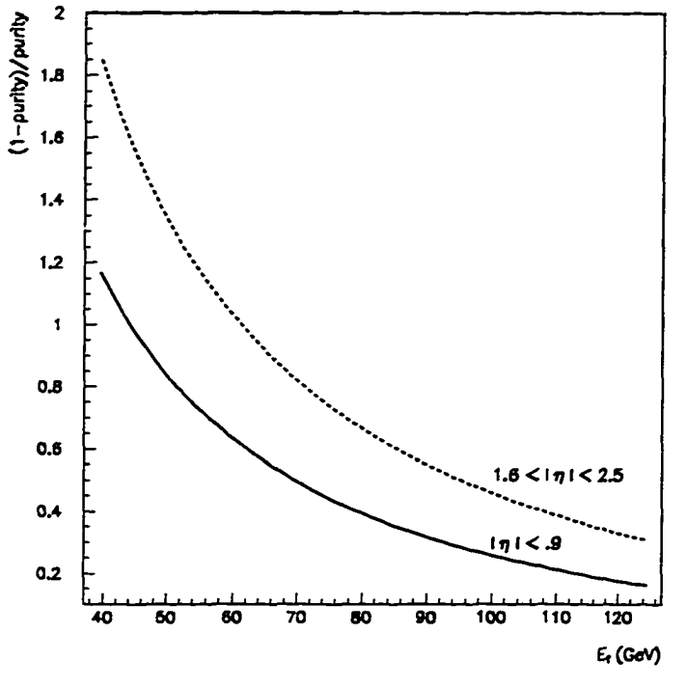


Figure B.1 Purity Factor for the central and forward regions of the detector.

The $E_T$ range is 40-125GeV. The lower $E_T$ limit stem from large systematic uncertainties at low $E_T$ in the Inclusive Jet Cross Section. The upper $E_T$ limit is caused by the lack of direct photons at higher Et. A simple exponential fit plus a constant to the P(jet $\rightarrow$ "$\gamma$") is also shown in Figure B.3. The fit is excellent and probably can be extrapolated in $E_T$ to some degree, except maybe at very low $E_T$.

The systematic error for Inclusive Jet Cross Section is 20.7% for the central region and 21.3% for the forward region. This includes trigger effeciency, jet quality cut effeciency, $\eta$-bias, and jet energy scale uncertainty. The systematic error for Isolated Direct Photon Cross Section is 8.7% for the central region and 14.1% for the forward region. This includes photon acceptance uncertainty, trigger and event selection efficiencies, purity uncertainty, and the electromagnetic energy scale uncertainty. The

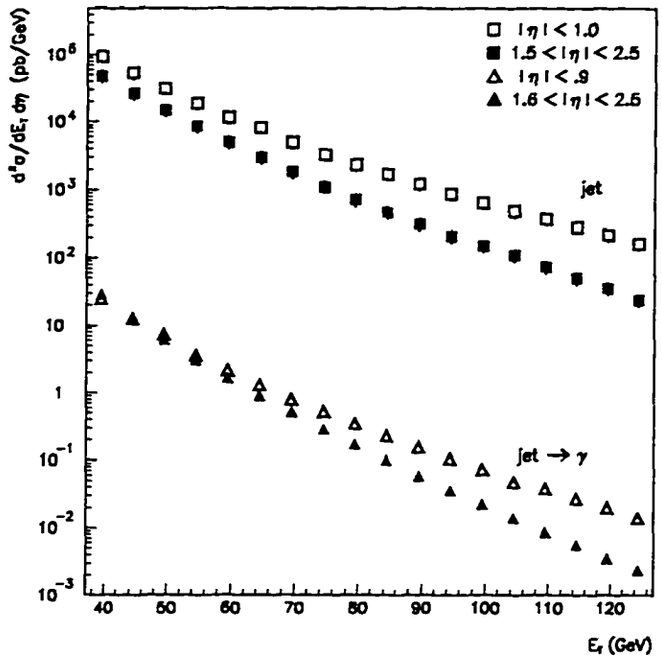


Figure B.2 $\frac{d^2\sigma}{dE_t d\eta}$ for the central and forward regions for the "Inclusive Jets" and for Jet $\rightarrow$ "$\gamma$".

systematic luminousity uncertainty is not included. The errors stated above are an average of the systematic errors over the entire $E_T$ and psuedorapidity range quoted initially. One note of caution, even though the Inclusive Jet Cross Section referenced has listed cross section values and systematic errors for the forward $\eta$ regions, the jet energy scale in this region is currently not well understood. The systematic error for each cross section was carried through to the probability by adding the errors in quadrature, and are displayed as error bars. Statistical error for the Inclusive Jet Cross Section is at least an order of magnitude less than systematic error. The statistical error for Isolated Direct Photon Cross Section is only significant at an $E_T > 100GeV$. The statistical errors are not shown.

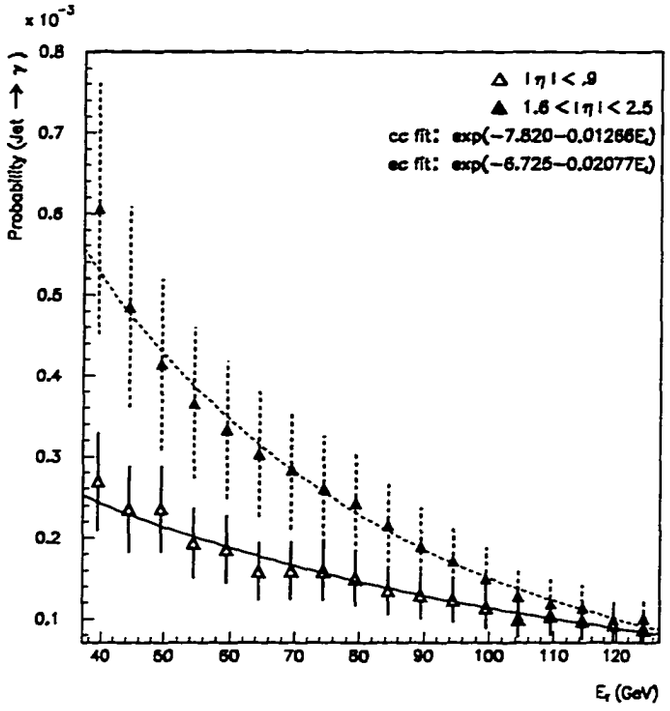


Figure B.3 Probability for a jet to fragment into isolated photon in the central and forward regions. The error bars are systematic only. excluded is the luminousity uncertainty.

## Conclusions

The strength of this method is that both cross section studies incorporate acceptances and efficiencies for all known effects, and both cross section papers agree well with QCD predictions at lower transverse energies. Further the P(jet $\rightarrow$ "$\gamma$") values are consistent with earlier studies, as stated before. Also, when the P(jet $\rightarrow$ "$\gamma$") is incorporated into personal diphoton QCD Monte Carlo background studies the MC results are consistent with data, which is encouraging.

When comparing reference 1 and the soon to be published run1a,b Inclusive Jet Cross Section values for $\eta < .5$ [44], there are definate differences. The new cross section values are $\simeq$ 15% smaller than reference 1. Further, the jet energy scaling and

correlations between all listed systematic errors are much better understood at this point, so the systematic errors are reduced by $\simeq 10\%$. However, there are limitations on how much the P(jet $\rightarrow$ "$\gamma$") value can be improved upon. Only when run1a.b's Inclusive Jet Cross Section papers are published and include the detector regions of this paper's interest, can new and improved probabilities be calculated.

# APPENDIX C CHARGED TRACKING EFFICIENCY CALCULATION

## Charged Track Efficiency

The events are selected from the run1 photon ntuples, which are calorimeter energy corrected with cafix 5.0. The level two filter used for run1a was gam_2_med and for run1b was em2_gis_gam. The filters required two em clusters with a $p_T$ greater than 12 GeV/c, that the shower shape be consistent with a photon, and in the run1b filter one of the em objects must be energy isolated. Their combined integrated luminousity is $93.3 \pm 5.0\ pb^{-1}$. The general event requirements are:

- vertex position within 75cm from $Z_{det} = 0$,
- both EM objects $p_T^{em} \geq 30$GeV/c,
- $|\ \eta_{em}\ | \leq 1.1$ or $1.5 \leq |\ \eta_{EM}\ | \leq 2.5$,
- $\chi^2_{EM} \leq 100$ for CC and EC,
- electromagnetic fraction $\geq .96$,
- EM cluster isolation cut,$|\ E_T(\Delta R = .4) - E_T(\Delta R = .2)\ | \leq 2GeV$.
- $86GeV \leq M_{ee} \leq 96GeV$ $Z$ mass window cut.

At this point it is assumed that all the events left are $Z$ boson events. Further, from other tracking studies and using sideband methods of estimating the background, the background is a few percent. The electrons are broken into four groups.

N(e-trk,cc) = Z electrons in cc with a track,

N(e-ntrk,cc) = Z electrons in cc without a track,

N(e-trk,ec) = Z electrons in ec with a track,

N(e-ntrk,ec) = Z electrons in ec without a track.

An electron's track is only accepted if the track is reconstructed in the em cluster's road, i.e. in a region of $\Delta R \leq 0.2$. Calculating the tracking efficiency is done by taking the following ratios.

$$\epsilon_t(cc) = \left\{ \frac{N(e-trk,cc)}{N(e-trk,cc) + N(e-ntrk,cc)} \right\} = 0.799 \pm 0.007 \pm 0.011$$

and

$$\epsilon_t(ec) = \left\{ \frac{N(e-trk,ec)}{N(e-trk,ec) + N(e-ntrk,ec)} \right\} = 0.799 \pm 0.013 \pm 0.020.$$

The statistical error is calculated using the binomial theorem assuming a Bernoulli process. The systematic errors are estimated by using a background subtraction method and using the Z resonance in the cc region and ec region only. The efficiencies calculated using this second method are very similar to the above quoted efficiences for both the cc and ec. The systematic error is estimated as one half the difference between the two methods.

# APPENDIX D DIPHOTON MASS DISTRIBUTION GAUSSIAN FITTED SAMPLES

## Diphoton Mass Distributions

The final selection criteria are applied to the seven MC Higgs samples and a diphoton mass is calculated and binned. The mass distributions are fitted with a Gaussian function, and all fits have a $\chi^2 < 1.5$. Notice that for each mass distribution the longer $M_{\gamma\gamma}$ tail on the lower mass region of the resonance. This caused by poorer energy sampling of the photon when it showers near a EM calorimeter modules edge (crack). On average this will shift the mass distribution downward, as seen in the Higgs's MC samples. The tail gets larger for the higher mass Higgs MC samples and this is reasonable, since the photons are of higher energy and are larger transversely, thus experience more crack problems.

The seven samples are: Figure D.1, Figure D.2, Figure D.3, Figure D.4, Figure D.5, Figure D.6, and Figure D.7.

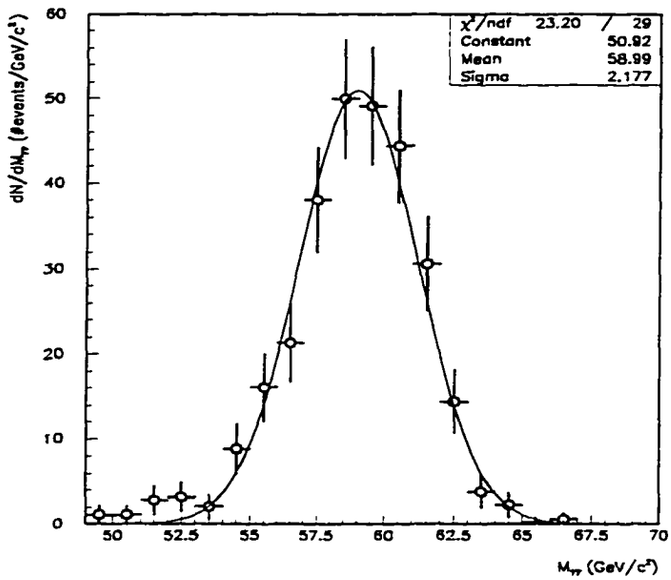


Figure D.1 The $M_{\gamma\gamma}$ distribution for the 60 GeV/$c^2$ Higgs sample.

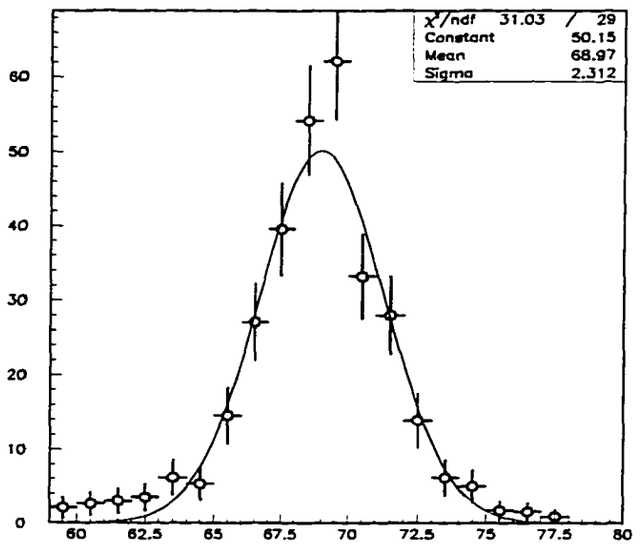


Figure D.2 The $M_{\gamma\gamma}$ distribution for the 70 GeV/$c^2$ Higgs sample.

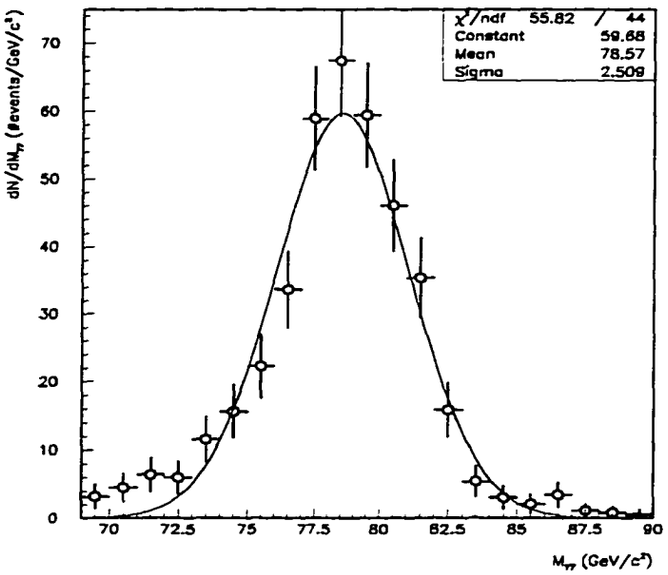


Figure D.3 The $M_{\gamma\gamma}$ distribution for the 80 GeV/$c^2$ Higgs sample.

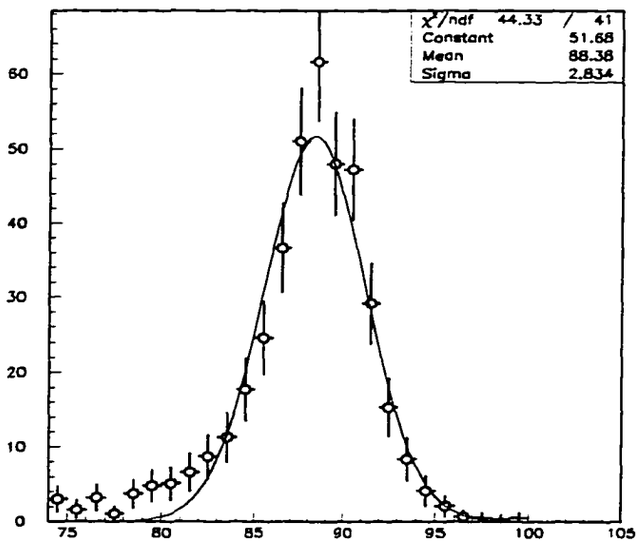


Figure D.4 The $M_{\gamma\gamma}$ distribution for the 90 GeV/$c^2$ Higgs sample.

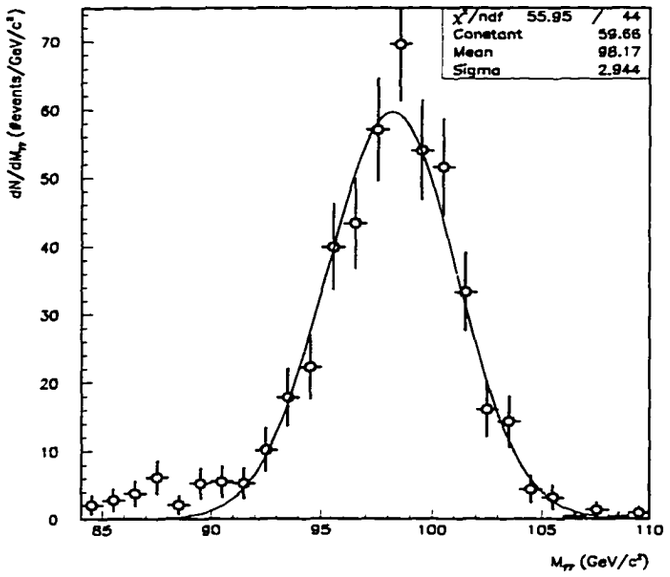


Figure D.5 The $M_{\gamma\gamma}$ distribution for the 100 GeV/$c^2$ Higgs sample.

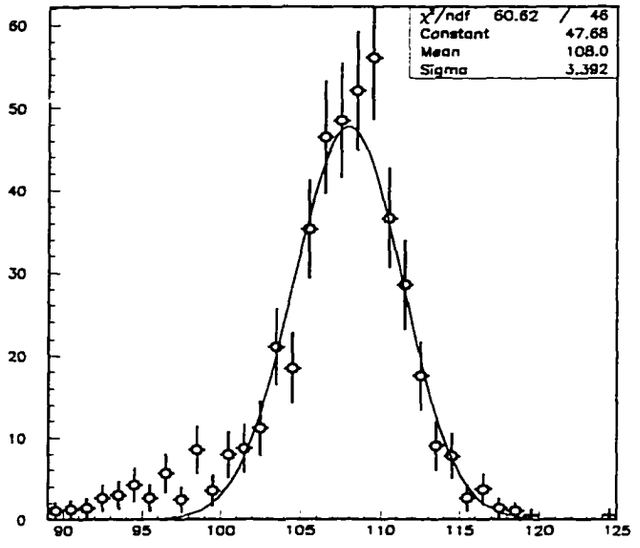


Figure D.6 The $M_{\gamma\gamma}$ distribution for the 110 GeV/$c^2$ Higgs sample.

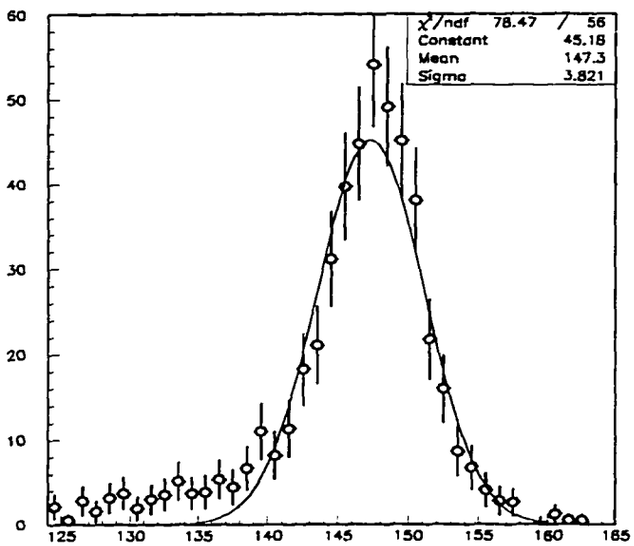


Figure D.7 The $M_{\gamma\gamma}$ distribution for the 150 GeV/$c^2$ Higgs sample.

# BIBLIOGRAPHY


[1] D. Griffiths, *Introduction to Elementary Particles*, (Wiley, New York, 1987).

[2] F. Halzen, A.D. Martin, *Quarks and Leptons: An Introductory Course in Particle Physics*, (Wiley, New York, 1984).

[3] A. Stange, W. Marciano, S. Willenbrock, Phys. Rev. D **49** numb. 3 (1994).

[4] V.D. Barger, R.J.N. Phillips, *Collider Physics*, (Addison-Wesley, New York, 1987).

[5] R.M. Barnett *et. al.*, Phys. Rev. D **54**, numb. 1 (1996).

[6] A.G.Akeroyd, **hep-ph/9511347**, (1995).

[7] A.G.Akeroyd, Phys. Lett. B **353**, 515 (1995).

[8] H.E. Haber, G.L. Kane, T. Sterling, Nucl. Phys. **B161**, 493 (1979).

[9] H. Pois, T. Weiler, T.C. Yuan, Phys. Rev. D **47**, 3886 (1993).

[10] P. Bamert, Z. Kunszt, Phys. Lett. B **306**, 335 (1993).

[11] H. Georgi, M. Machacek, Nucl. Phys. **B262**, 463 (1985); M. Chanowitz, M. Golden, Phys. Lett. B **165**, 105 (1985).

[12] M. Acciarri *et. al.*, *Search For New Particles In Hadronic Events with Isolated Photons*, **CERN-PPE/96-50**, (1996).

[13] J. Thompson. *Introduction to Colliding Beams at Fermilab.* **Fermilab-TM-1909**, (1994, unpublished).

[14] J. Thompson, *Design report Tevatron 1 project*, FNAL internal note. (1984. unpublished).

[15] Fermi National Accelerator Laboratory, *A report of the design of the Fermi National Accelerator Laboritory Superconduction Accelerator*, FNAL internal note. (1979, unpublished).

[16] S. Abachi *et al.*, Nucl. Inst. Meth., **A338**, (1994).

[17] J.F. Detoeuf *et al.*, Nucl. Inst. Meth., **A265**, (1988).

[18] R.C. Fernow, *Introduction to Experimental Particle Physics*, (Cambridge University Press, Cambridge, 1986).

[19] A.R. Clark *et al.*, Nucl. Inst. Meth., **A265**, (1988).

[20] E. Gallas, K. De, M. Sosebee, *The Contribution of the ICD to Missing Transverse Energy Resolution in DØ's Run 1*, DØNote 2494, (1994, unpublished).

[21] C. Brown *et al.*, Nucl. Inst. Meth., **A279**, (1989).

[22] J. Bantly *et al.*, IEEE Trans. on Nucl. Sci., **41**, 1274, (1994).

[23] M. Abolins *et al.*, IEEE Trans. on Nucl. Sci., **36**, 384, (1989); Nucl. Inst. Meth.. **A289**, 543 (1990).

[24] D. Cutts *et al.*, IEEE Trans. on Nucl. Sci., **36**, (1989).

[25] S. Youssef, *Comp. Phys. Comm.* **45**, 423 (1987).

[26] N. Hadley, *Cone Algorithm for Jet Finding.* DØnote 904. (1989, unpublished).

[27] R. Kehoe, R. Astur, *Dertimination of the Hadronic Energy Scale of DO Calorimetry - cafix version 5.0*, DØNote 2908, (1996, unpublished).

[28] B.A. Lauer, *Efficiency of Photon's No-Reconstructed Track Requirement.* DØNote 3176, (1997, unpublished).

[29] G. Landsberg, *Search for Anomalous Couplings in the $Z(\nu\nu)\gamma$ Channel with Run Ia Data*, DØNote 3047, (1996, unpublished).

[30] S. Chopra, *Search for Pair Production of Charginos and Neutralinos in Models with Low Energy Gauge Mediated Supersymmetry Breaking*, DØNote 3141. (1996. unpublished).

[31] S. Abachi *et al.*, *Search for a Fourth Generation Charge -1/3 Quark via Flavor Changing Neutral Current Decay*, **hep-ex/9611021**, (1996).

[32] W. Chen, Thesis, State University of New York, Stony Brook (1997).

[33] Mike Kelly, *Jet Faking Photon/Electron Study*, DØNote 1659, (1993, unpublished).

[34] S.A. Jerger, Thesis, Michagan State University, East Lansing, Michigan (1997).

[35] Harry Melanson; private communication.

[36] F. Hsieh, R. Partridge, S. Snyder, *Jet Energy Scale Uncertainty for Top Cross Section PRL*, DØNote 1234, (1997, unpublished).

[37] B.A. Lauer, *Efficiency of Photon's No-Reconstructed Track Requirement.* DØNote 3176, (1997, unpublished).

[38] F. Abachi *et al.*, *The Isolated Photon Cross Section in the Central and Forward Rapidity Regions in $p\bar{p}$ Collisions at $\sqrt{s}$ = 1.8 TeV*, Phys. Rev. D **77**, 5011 (1996).

[39] John Womersley; private communication.

[40] G. Landsberg, *Search for Anomalous Couplings in the $Z(\nu\nu)\gamma$ Channel with Run Ia Data*, DØNote 3047 (1996, unpublished).

[41] Victor Daniel Elvira, Thesis, Universidad de Buenos Aires, (1994).

[42] F. Abachi *et al.*, *Diphoton Production in $p\bar{p}$ Collisions at $\sqrt{s} = 1.8TeV$*. **Fermilab-Conf-95/251-E**, (1995).

[43] Mike Kelly, *The Doomsday Study of QCD Fakes for $W\gamma$ in RECO 11*, DØNote 2215, (1994, unpublished).

[44] J. Blazey, D. Elvira, B. Hirosky, Editoral Board Number 049, *Comparison of Large $E_T$ Jet Production with QCD Expectations*, (1996, unpublished).